Optical, Noncontact, Automated Experimental Techniques for Three-Dimensional Reconstruction of Object Surfaces Using Projection Moire, Stereo Imaging, and Phase-Measuring Profilometry

By JAIME F. CARDENAS-GARCIA, Texas Tech University; and
GARY R. SEVERSON, U.S. Geological Survey

U.S. GEOLOGICAL SURVEY

Open-File Report 95-433

Prepared in cooperation with the
NEVADA OPERATIONS OFFICE,
U.S. DEPARTMENT OF ENERGY, under
Interagency Agreement DE-AI08-92NV10874

Denver, Colorado
1996

U.S. DEPARTMENT OF THE INTERIOR
BRUCE BABBITT, Secretary

U.S. GEOLOGICAL SURVEY
Gordon P. Eaton, Director

For additional information write to:

Chief, Hydrologic Investigations Program
Yucca Mountain Project Branch
U.S. Geological Survey
Box 25046, Mail Stop 421
Denver Federal Center
Denver, CO 80225-0046

Copies of this report can be purchased from:

U.S. Geological Survey
Branch of Information Services
Box 25286
Denver, CO 80225-0286

CONTENTS

FIGURES

TABLES

CONVERSION FACTORS

Multiply	By	To Obtain
millimeter (mm)	0.03937	inch
meter (m)	3.2808399	foot

Optical, Noncontact, Automated Experimental Techniques for Three-Dimensional Reconstruction of Object Surfaces Using Projection Moire, Stereo Imaging, and Phase-Measuring Profilometry

By Jaime F. Cardenas-Garcia *and* Gary R. Severson

Abstract

Three optical, noncontact, automated experimental techniques for determining the topography of object surfaces were assessed. The main objective was to test the limitations of three experimental techniques: projection moire, stereo imaging, and phase-measuring profilometry. Phase-measuring profilometry is the most promising of the three techniques for mapping rock fracture surfaces automatically, accurately, quickly, and with high resolution. The experimental set-ups used to assess these different techniques are similar, and they require essentially the same equipment. It is relatively easy and inexpensive to go from one experimental set-up to another. Also, the experience gained in implementing one experimental technique is often applicable in another, although the basic principles of each experimental technique are sometimes very dissimilar.

The first technique, projection moire, is an optical experimental technique that is useful for displaying and measuring the three-dimensional form of large objects. Manual analysis of

INTRODUCTION

This study was conducted by the U. S. Geological Survey and Texas Tech University, done in cooperation with the U.S. Department of Energy for the Yucca Mountain Site Characterization Project. Yucca Mountain in Nye County, Nevada is being studied as a potential site for a high-level radioactive waste repository. The Yucca Mountain Site Characterization Project was established to evaluate the potential for storing nuclear wastes in geologic formations on or adjacent to the Nevada Test Site. As part of this site-characterization effort, a series of tests to investigate the hydrologic characteristics of the welded and nonwelded tuffs at Yucca Mountain have started at the Exploratory Studies Facility at Yucca Mountain. Fracture flow characteristics are being studied in the unsaturated zone of Yucca Mountain, where the potential repository will be located, as part of the site-characterization work. One of the tests being conducted for site characterization purposes is the Intact-Fracture Test in the Exploratory Studies Facility (U.S. Department of Energy, 1988), which measures fluid flow in single fractures under laboratory conditions. One of the unknowns in the site-characterization studies is the role of fracture roughness in controlling fluid flow through single, partially saturated fractures. The Intact-Fracture Test will help better understand the relations between unsaturated-fracture flow and fracture roughness. Therefore, a method is needed to digitize the topography of fracture surfaces.

experimental moire data is tedious and time consuming; therefore, calibration of the experimental set-up, determination of the fringe number, phase measurement at a point, and distinction of concavity and convexity of a surface were automated in these studies. Also, estimates of the error for simply shaped objects were obtained. For the second technique, two stereo-imaging experimental set-ups that are useful in measuring the three-dimensional geometry of objects were studied: a parallel optical-axis model and a converging optical-axis model. Digital image correlation was used to find the disparities between corresponding points in a pair of images for each of these models with subpixel accuracy. To show the application of the developed algorithms and the stereo-imaging experimental set-ups, four different object surfaces were studied. For some of the objects, a higher measuring accuracy was obtained from a converging optical-axis experimental set-up. For the third technique, a new, fast, phase-measuring profilometer for full-field three-dimensional shape measurement was developed. Compared to other optical methods for three-dimensional shape measurement, this technique is faster and more accurate. The technique is based on the principle of phase measurement of a projected grating image on the object surface that conforms to the shape of the object. This deformed grating pattern carries the three-dimensional shape information of the surface to be measured. Six different kinds of surface shapes were measured with this experimental technique. The measurement error was less than 0.15 percent. For the objects used, the resolution reached 50 microns.

Purpose and Scope

This report presents the cumulative results of examining three optical, noncontact, automated experimental techniques for three-dimensional reconstructoin of object surfaces for mapping rock fracture surfaces. The three experimental techniques are projection moire, stereo imaging, and phase-measuring profilometry which were examined in the laboratory in that order. The experimental set-ups used to assess these three different experimental techniques are very similar and require essentially the same equipment. It is relatively easy and inexpensive to go from one experimental set-up to another, and the experience gained in one experimental technique often is applicable to another, although the basic principles of each experimental technique are sometimes very dissimilar. The main objective in this assessment was to test the limitations of each experimental technique for mapping rock fracture surfaces.

Acknowledgments

The authors acknowledge the contributions made by H.G. Yao in helping to set up some of the experiments described in the first section of this report. H.G. Yao and S. Zheng of the Optomechanics Research Laboratory in the Department of Mechanical Engineering at Texas Tech University, Lubbock, Texas, contributed to the work described in the second and third sections of this report.

AUTOMATED PROJECTION MOIRE FOR THREE-DIMENSIONAL RECONSTRUCTION OF OBJECT SURFACES

The use of the moire phenomenon for scientific purposes is more than a century old and was first reported by Lord Rayleigh (1874). Only in the last twenty years has interest grown in using moire techniques for topographical measurement applications. Meadows and others (1970), Allen and Meadows (1971), and Takasaki (1970, 1973) proposed this type of application and did the necessary analysis and experimentation to give it credibility. Since that time, shadow and projection moire techniques have been developed and applied in many situations (Tsuruta and others, 1970; Yokozeki and Suzuki, 1970; Der Hovanesian and Hung, 1971; Jaerisch and Makosch, 1973; Chiang, 1975; Idesawa and others, 1977; Heiniger and Tschudi, 1979; Moore and Truax, 1979; Perrin and Thomas, 1979). In the last decade, the advent and easy accessibility of microcomputers and video technology enabled convenient digital image processing of acquired moire experimental results. These developments have allowed more flexibility and creativity in exploring the full potential of moire-based topographical techniques (Livnat and others, 1980; Funnell, 1981; Cline and others, 1982; Yatagai and others, 1982; Doty, 1983; Gasvik, 1983; Halioua and others, 1983; Harding and Harris, 1983; Robinson, 1983; Schemm and Vest, 1983; Cline and others, 1984; Gasvik and Fourney, 1986; Meyer-Arendt and others, 1987; Dirckx and others, 1988; Jin and Tang, 1989).

The moire phenomenon is not observed in nature except where order has been imposed by humankind in the form of picket fences, bamboo huts, or woven fabrics. The simplest moire creation results from the superimposition of nearly identical regular patterns almost parallel to each other. The result is a "watered or wavy appearance" (Durelli and Parks, 1970; Dally and Riley, 1991; Karara, 1989) formed by the secondary fringes. These resulting secondary fringes (or moire fringes) have much lower density (or frequency) and stronger contrast than those of the original primary fringes. Two approaches are generally taken by researchers to apply moire techniques to surface topography measurements. The most common approach is shadow moire, where only one grid is used with a light source and image recording equipment. Figure 1 shows a common experimental set-up (Gasvik, 1987; Kafri and Glatt, 1990; Dally and Riley, 1991). The use of one grid accomplishes the objectives of allowing projection of the grid onto the object and serving as the reference grating for viewing the moire fringes. The grid needs to be close to the object to prevent a deteriorative diffraction effect in the projecting shadow. Also, if there is great variation in the height of the object along the direction of the projection compared to the period of the grid, diffraction will occur. The major disadvantage of using shadow moire is that the grid needs to be at least as large as the object being studied. The result is an image with a set of fringes on the object representing a topographic map. By correctly interpreting these fringes, it is possible to obtain the three-dimensional coordinates

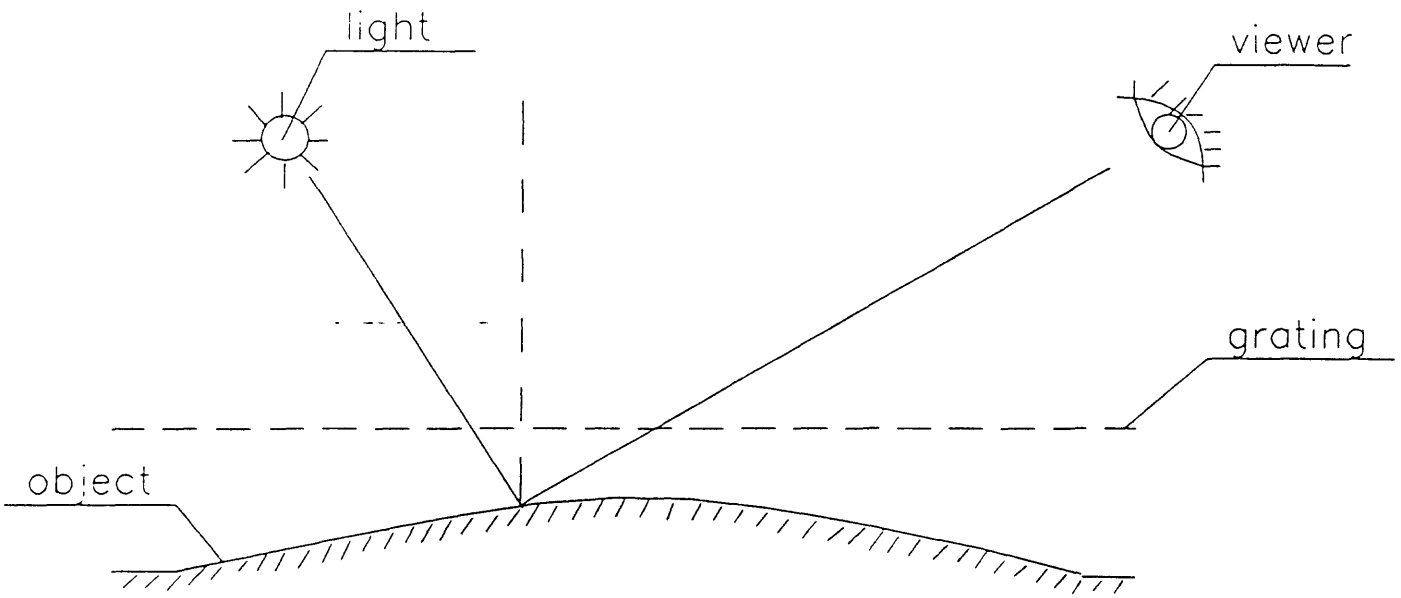

Figure 1. Schematic of shadow moire.

of every point on the object surface.

The other approach to surface topography measurements is projection moire. A typical experimental set-up is shown in figure 2 (Doty, 1983; Gasvik, 1987; Dally and Riley, 1991). In this technique two equal gratings are used with a matched projector (containing the light source) and a viewer (which may incorporate image-recording equipment). The projector is used to project one grating onto the object, which allows for greater flexibility when analyzing objects of varying size. Objects from a fraction to several meters in size can be accommodated. The only limitations in the size of the object to be assessed are determined by the power of the illumination source attached to the projector and the sensitivity of the measurements to be performed. The object, with a projected grating on its surface, is imaged using the viewer containing the reference grating. The result is an image similar to that obtained with shadow moire, except that now the grating size is not a limitation. Similar interpretation of the fringes yields the three-dimensional coordinates of every point on the object surface. An experimental set-up of this type is described in this section of the report.

Although many papers have been written on the use of projection moire, whether automated or not, it is uncommon to obtain detailed specifications on experimental data with the errors associated with the experimental set-ups. Also, simple shapes are

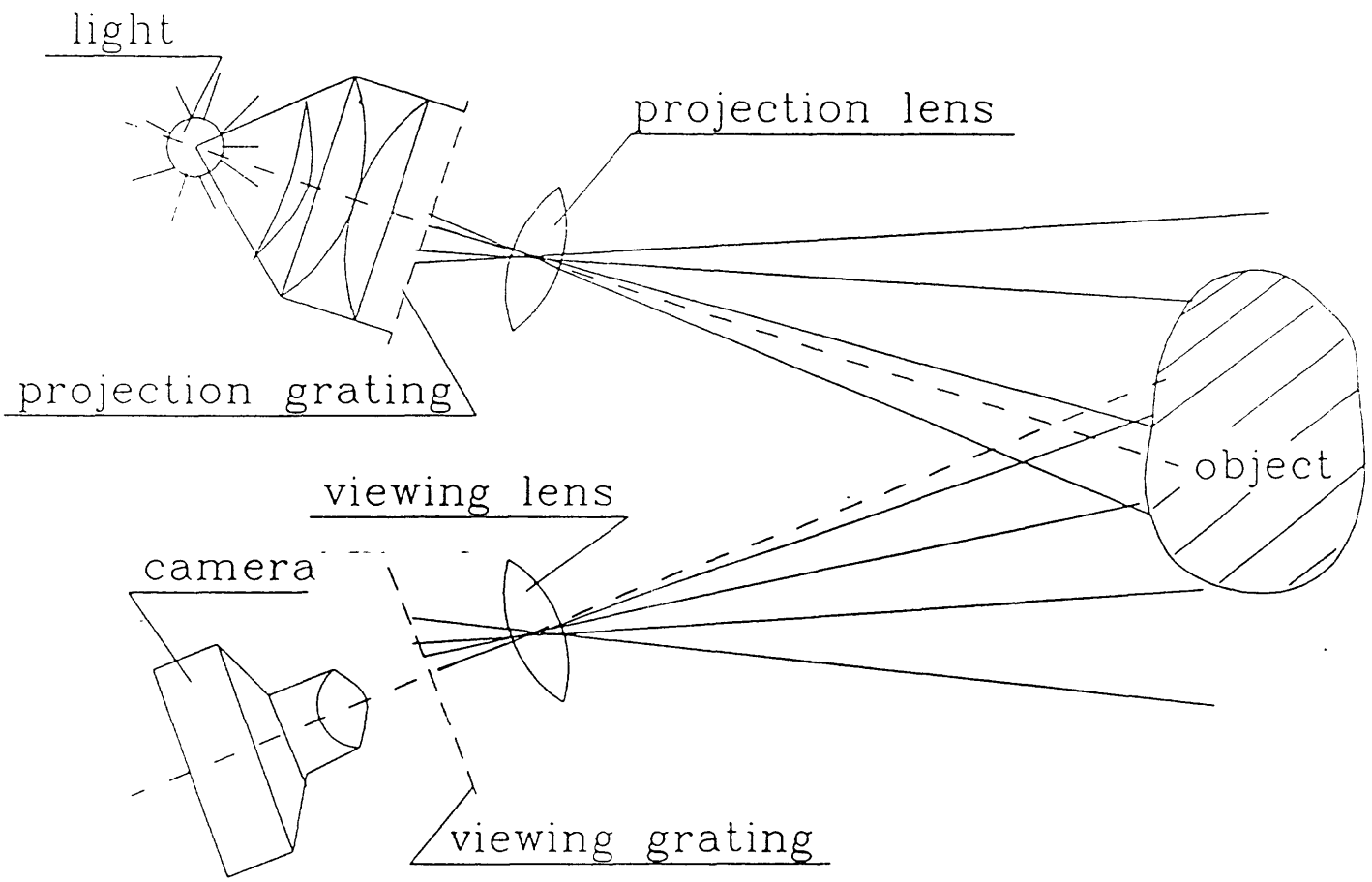

Figure 2. Schematic of projection moire.

generally used to simplify the analysis of the object surfaces. Possibly one of the reasons for not detailing the obtained accuracies and for not considering more complex shapes is that manual analysis of experimental moire data is tedious and time consuming. To analyze the data and obtain experimental errors and accuracies, many researchers have applied image processing techniques to the acquired video images of the moire fringes (Cline and others, 1982; Yatagai and others, 1982; Robinson, 1983; Gasvik, 1983; Cline and others, 1984; Gasvik and Fourney, 1986). One aspect that has not been made explicit in these papers is an analysis of the sensitivity and accuracy of the experimental set-ups. The main objective of this section of the report is to describe in detail an automated experimental implementation of projection moire. This section includes the calibration of the experimental set-up, the determination of the fringe number, the phase measurement at any point, and the distinction of concavity and convexity of a surface. Also, estimates of error on several simply shaped specimens are obtained. This section of the report has been previously described in Cardenas-Garcia and others (1991).

Experimental Set-up

The experimental set-up for this automated projection moire implementation is shown in figure 3, with a corresponding schematic shown in figure 4. The origin of the Cartesian coordinate system is set at the intersection of the viewer optical axis and the

viewer lens plane. Reference will be made to this Cartesian coordinate system throughout this section. The moire projector and viewer were mounted onto a precisely machined aluminum base, which is shown in figure 5. The mounting base for the projector and viewer is fixed and was designed for easy disassembly and for repeatable measurements. The fundamental aspects of this experimental set-up are that the optical axes of the moire projector and viewer are separated by a fixed distance of 91.4 ± 0.0254 mm, are parallel to each other to within ± 0.0254 mm over a distance of 200 mm, and lie in the same horizontal plane. Also, the projector and viewer gratings are the same nominal fixed distance from the base plane, distance Z_o in figure 4. The matched pair of gratings have a pitch of 0.05 mm (see appendix for other grating information). Also, a Cohu Model 4815 charge-coupled device (CCD) video camera is attached to the viewer. The number of horizontal and vertical picture elements (or pixels) is 752 and 480, respectively. All lenses used in this set-up are Nikon 55-mm micro lenses. A C-mount is used to attach the lens to the video camera. An EPIX, Inc., 1-megabyte image memory Silicon Video digitizing image processing board is attached to the video camera for data acquisition. Image processing is performed using Microsoft C, which is compatible with the software drivers on the imaging board. The imaging board resides in a Compaq 386/25 micro-computer. Attachments to this experimental set-up include a model PVM-1342Q Sony Trinitron color video monitor and a model P61U Mitsubishi video copy processor. Also, a model 106122P-20M Daedal

X-Y linear motion positioning table with computer control capable of 300-mm maximum travel, with an accuracy of ± 0.001 mm is used.

To obtain moire fringes that accurately reflect the actual contour lines of the object under study, the following conditions for the experimental set-up have been observed (Perrin and Thomas, 1979; Doty, 1983):

a. The optical axes of the projection and the viewing systems are parallel and aligned along the same horizontal plane;

b. The projection and viewing gratings are in the same vertical plane, which is perpendicular to the optical axes;

c. The distance from the lens to the grating in the projection system is equal to that in the observation system.

If both axes are not parallel or not in the same horizontal plane, the moire fringes do not accurately reflect the contour lines of the object, complicating the fringe analysis.

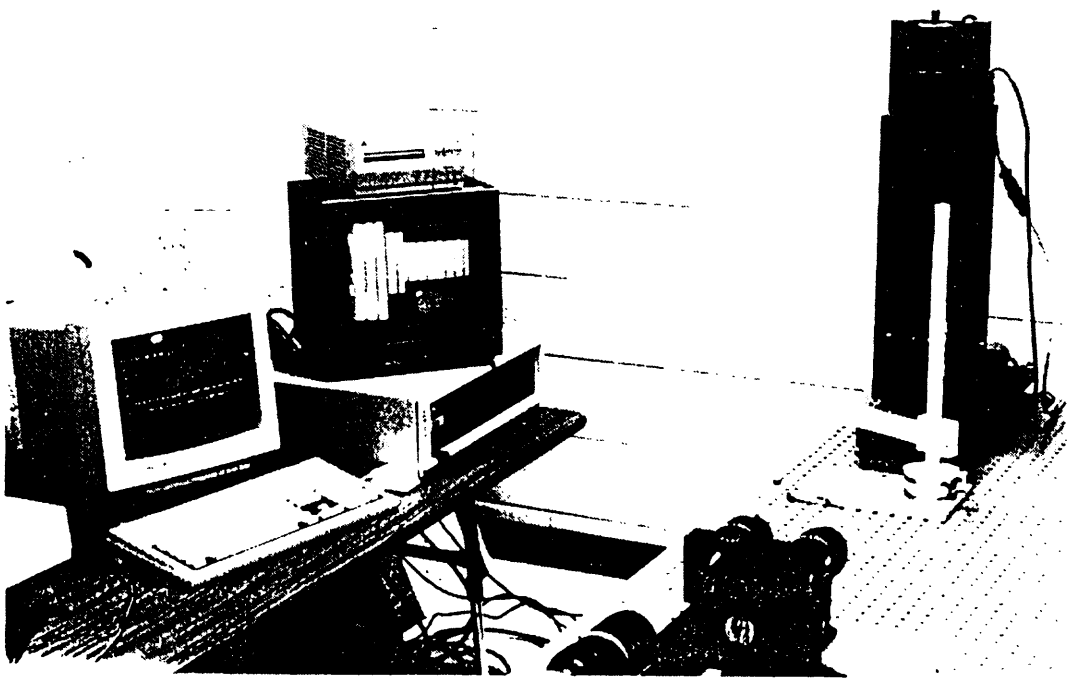

Figure 3. Projection moire experimental set-up used.

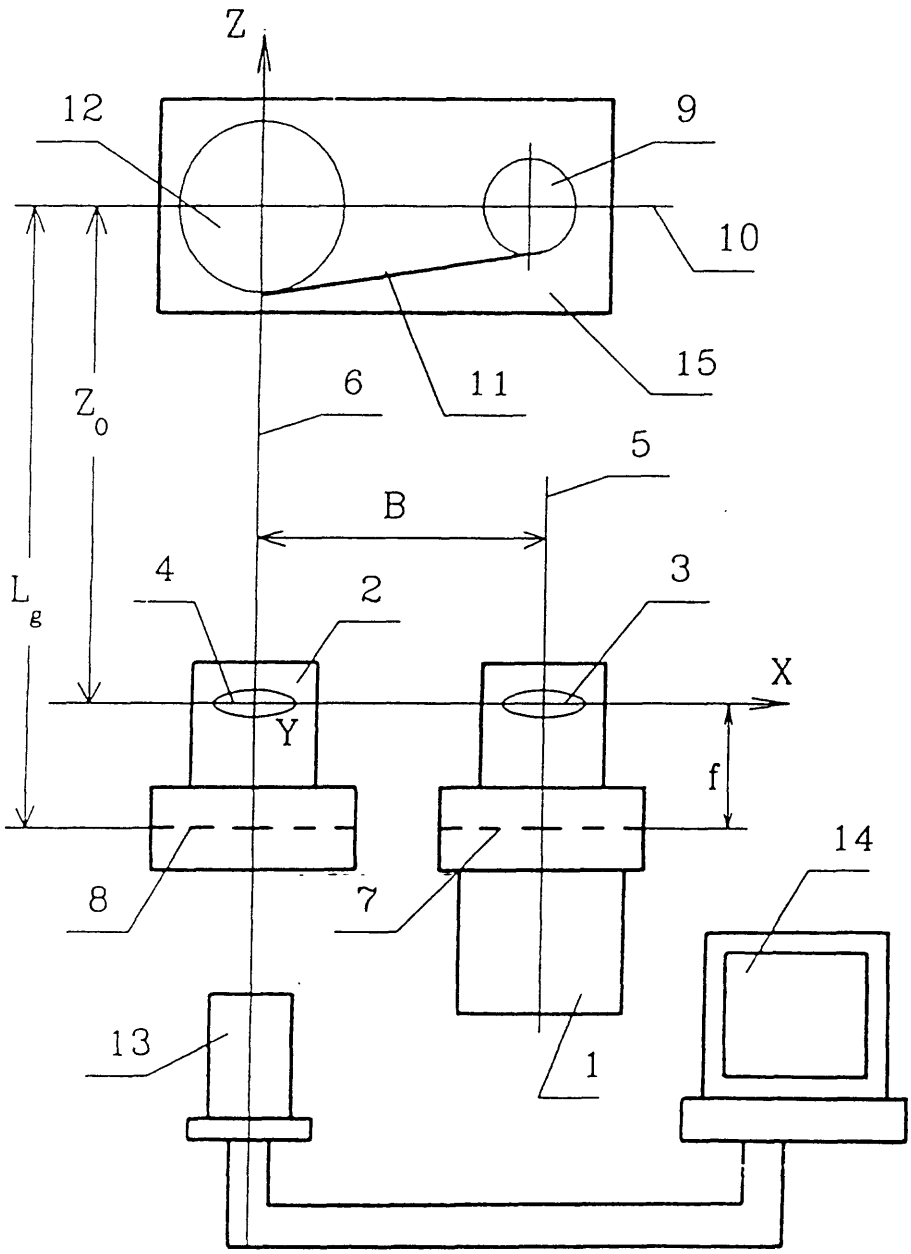

1. projector
2. viewer
3. projector lens
4. viewer lens
5. projection axis
6. viewing axis
7. projection grating
8. viewing grating
9. rotating table
10. base plane
11. calibration ruler
12. object
13. video camera
14. image processor and computer
15. X-Y positioner

Figure 4. Schematic of projection moire experimental set-up used.

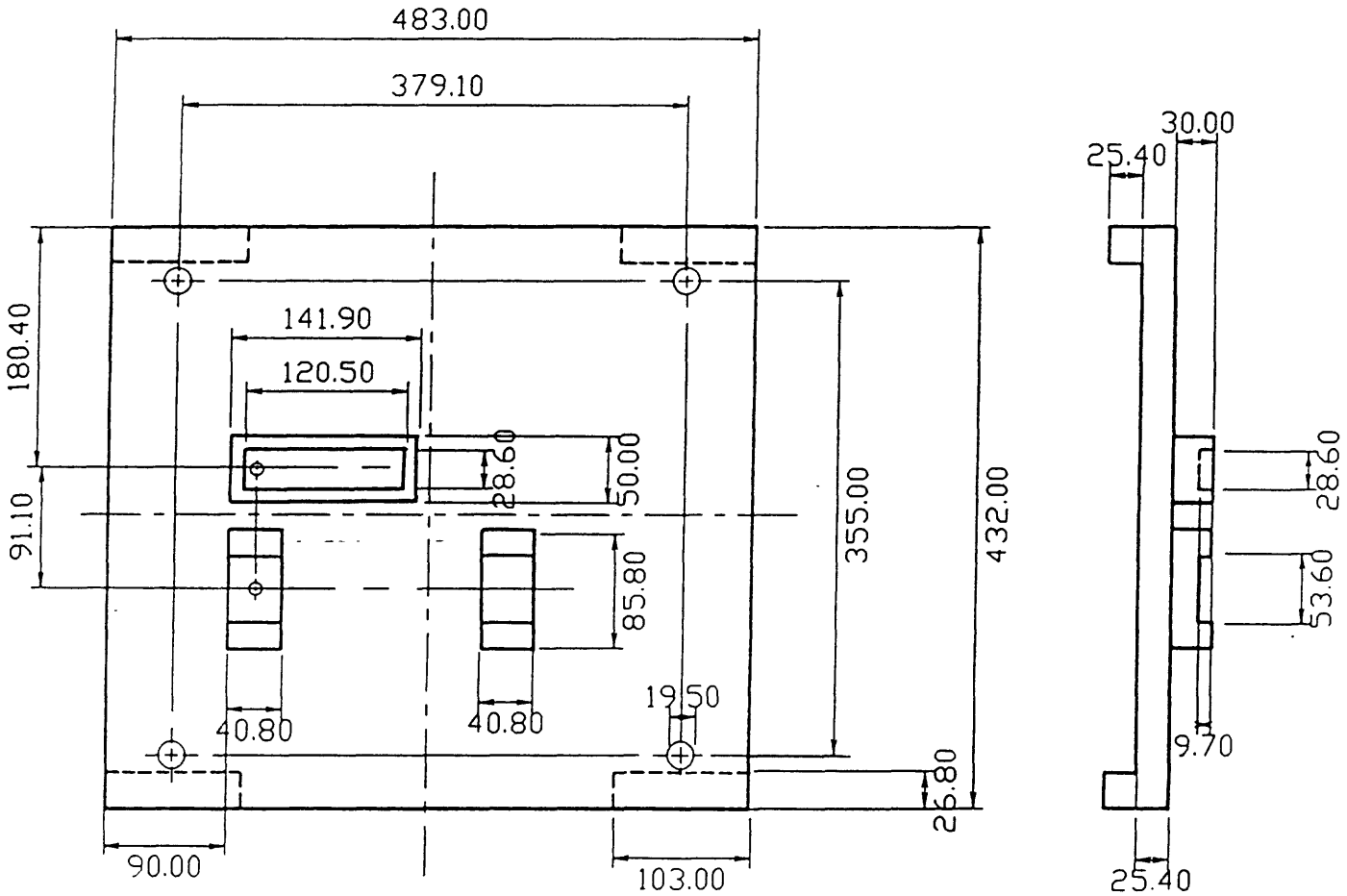

Figure 5. Plan view of aluminum base used for mounting moire projector and viewer (all units are in millimeters).

Calibration

The calibration of the experimental set-up used in this study requires the determination of several important set-up parameters. Once these set-up parameters are determined and used in conjunction with the experimental set-up, an accurate determination of surface topography can be obtained when used on a well-defined surface. An implicit assumption is that any inaccuracies that result from lens distortion and equipment alignment are accounted for in the calibration procedure, as any resulting errors are systematic. The general procedure is similar to the one followed by Perrin and Thomas (1979) and relies on a rotating plane calibration ruler. The rotating stage on which the rotating calibration ruler is mounted has an accuracy of ± 0.017 degrees. Using the rotating stage enables the determination of the base plane; the magnification factor, m_f; the distance between the camera lens and the base plane, Z_o; the distance between the camera lens and the grating, f; the fringe number on the base plane, n_b; and the relation between the fringe number, n, and the distance between two fringes, Δz. The schematic of the experimental set-up, shown in figure 4, is referred to in the following explanation of how to obtain each of these parameters.

The rotating plane calibration ruler is placed at the center of the field of view. If the rotating plane calibration ruler is positioned so that it is normal to the z-axis, it will show a constant phase distribution, which is easily tested at a particular

z-location by tilting the rotating plane back and forth until a uniform intensity is obtained. The tilt angle obtained at the base configuration can be easily adjusted to zero degrees using an attached vernier dial with an accuracy of ± 0.017 degrees. Thus, it is possible to locate the base plane at the axis of rotation at either total extinction, full intensity, or at any other constant phase position by moving the computer-controlled translation stage along the z-axis. For calibration purposes, the base plane is positioned on the translating stage where the base plane is fully illuminated. The video digitizer, using the computer-controlled translation stage makes this determination of the base plane with less than 1 percent error. The image-processing algorithm calculates the fringe centers using the lowest gray level value. A more complete description of useful algorithms for this purpose may be found in Cardenas-Garcia and others (1991). These calculations are easily done along two axes of rotation of the ruler. The x- and y-axis are considered separately. The base plane, which is normal to the z-axis, is located at each axis of rotation. Also, the rotation axis is positioned so that it coincides with the center of the field of view.

The magnification factor, m_f, is obtained by projecting an image of the grating on the base plane and counting the number of lines per unit length that are projected on the base plane. By comparing the grating spatial frequency (lines per mm), ν, used in the experimental set-up with the projected grating pitch, the magnification factor is calculated from

$$m_f = \frac{v}{\left(\frac{N}{d}\right)} \tag{1}$$

where d is the distance of grating projection, and N is the number of projected grating lines observed.

Given the magnification factor, m_f, the distance between the camera lens and the base plane, Z_o, and the distance between the camera lens and the grating, f, are obtained from combining the equations

$$m_f = \frac{Z_o}{f} \tag{2}$$

and

$$\frac{1}{Z_o} + \frac{1}{f} = \frac{1}{\lambda} \tag{3}$$

where λ is the lens focal length. Then Z_o and f can be determined from

$$Z_o = (m_f + 1)\,\lambda \tag{4}$$

and

$$f = \left(1 + \frac{1}{m_f}\right)\lambda . \tag{5}$$

By tilting the rotating plane, it is possible to obtain any desired number of fringes. The resulting moire patterns, at

different tilt angles, for rotating plane rotation about the x-axis are shown in figures 6(a) through 6(e). The moire patterns for rotating plane rotation about the y-axis are shown in figures 7(a) through 7(e). In both sets of pictures, it is possible to observe parallel sets of fringes on the surface of the tilted plane. The observed moire fringes are interpreted as contour lines of the object. They are equi-order surfaces normal to the optical axis (z-axis). The coordinate of the nth fringe center, z_n, can be calculated (Perrin and Thomas, 1979) using

$$z_n = \frac{2fB\nu}{2n+1} \tag{6}$$

where f is the image length of the lenses, B is the distance between two optical axes, ν is the grating spatial frequency (lines per mm), and n is the fringe number. In order to obtain the coordinates (x_n,y_n) at the center of the fringe on the object corresponding to the coordinates (x_m,y_m) on the viewer image plane, the following relations can be used:

$$x_n = x_m \frac{z_n}{f} \tag{7}$$

and

$$y_n = y_m \frac{z_n}{f}. \tag{8}$$

It is also possible to find the fringe number on the base plane, n_b, from

$$n_b = \frac{2Bf\nu - Z_o}{2Z_o}. \tag{9}$$

Generally the fringe number is a large number and any possible error in its determination is not very significant when calculating Δz, which is the parameter of interest in moire topography. Once the base plane has been identified and numbered, each additional fringe can easily be numbered, which is especially true in the case of a tilted plane where the numbering will either increase or decrease monotonically. In other applications, as described below, a paper tape may be used as an extended portion of the tilted calibration ruler to connect it with the object of interest. The fringe numbering can then be easily transferred to the object using the tilted calibration ruler as a reference.

Using equation 6, the distance between adjacent fringes Δz_t is easily found to be

$$\Delta z_t = z_{n+1} - z_n = \frac{4fB\nu}{(2n+3)(2n+1)}. \tag{10}$$

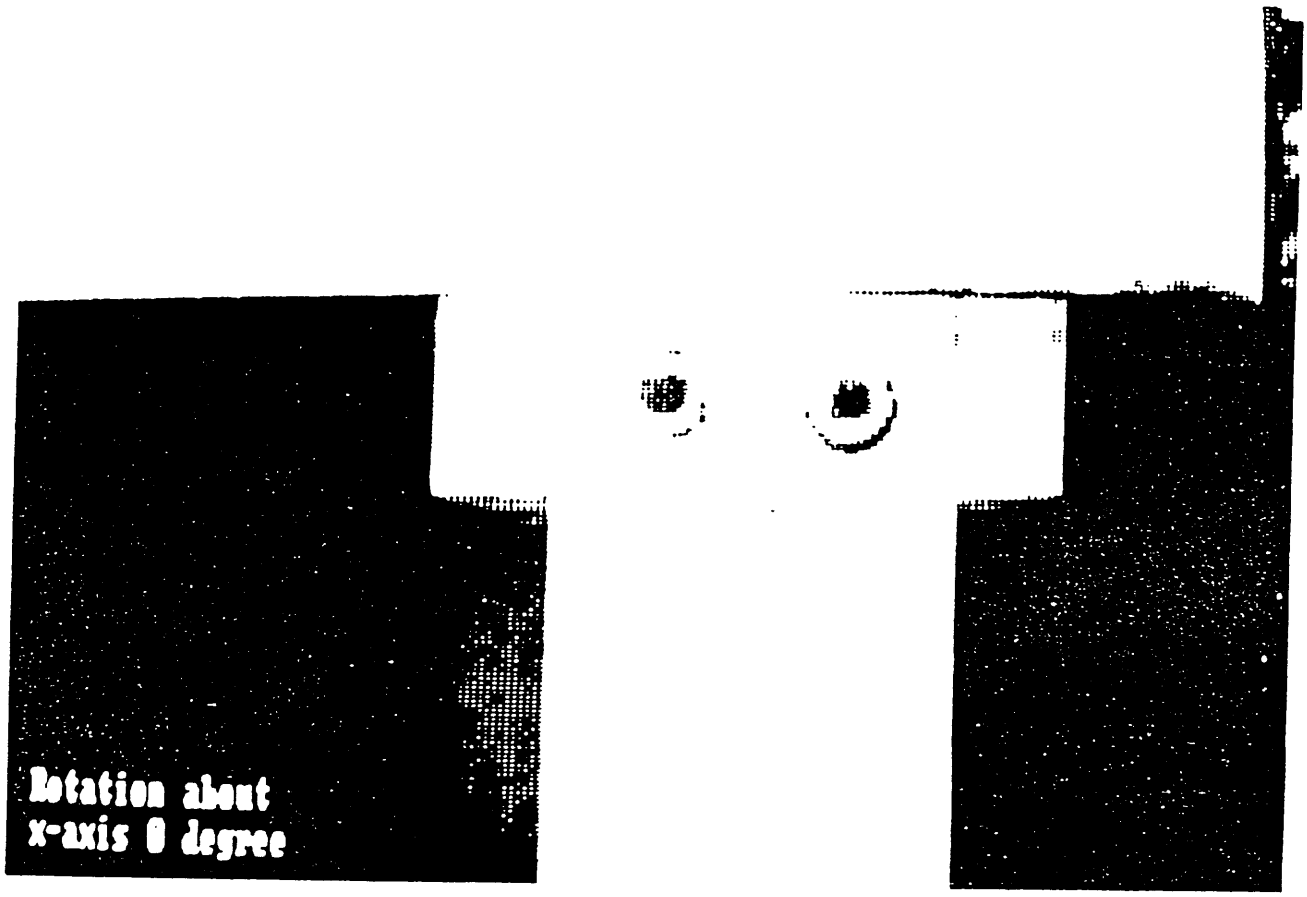

Figure 6a. Rotating plane calibration ruler positioned to rotate about the x-axis, α = 0 degrees.

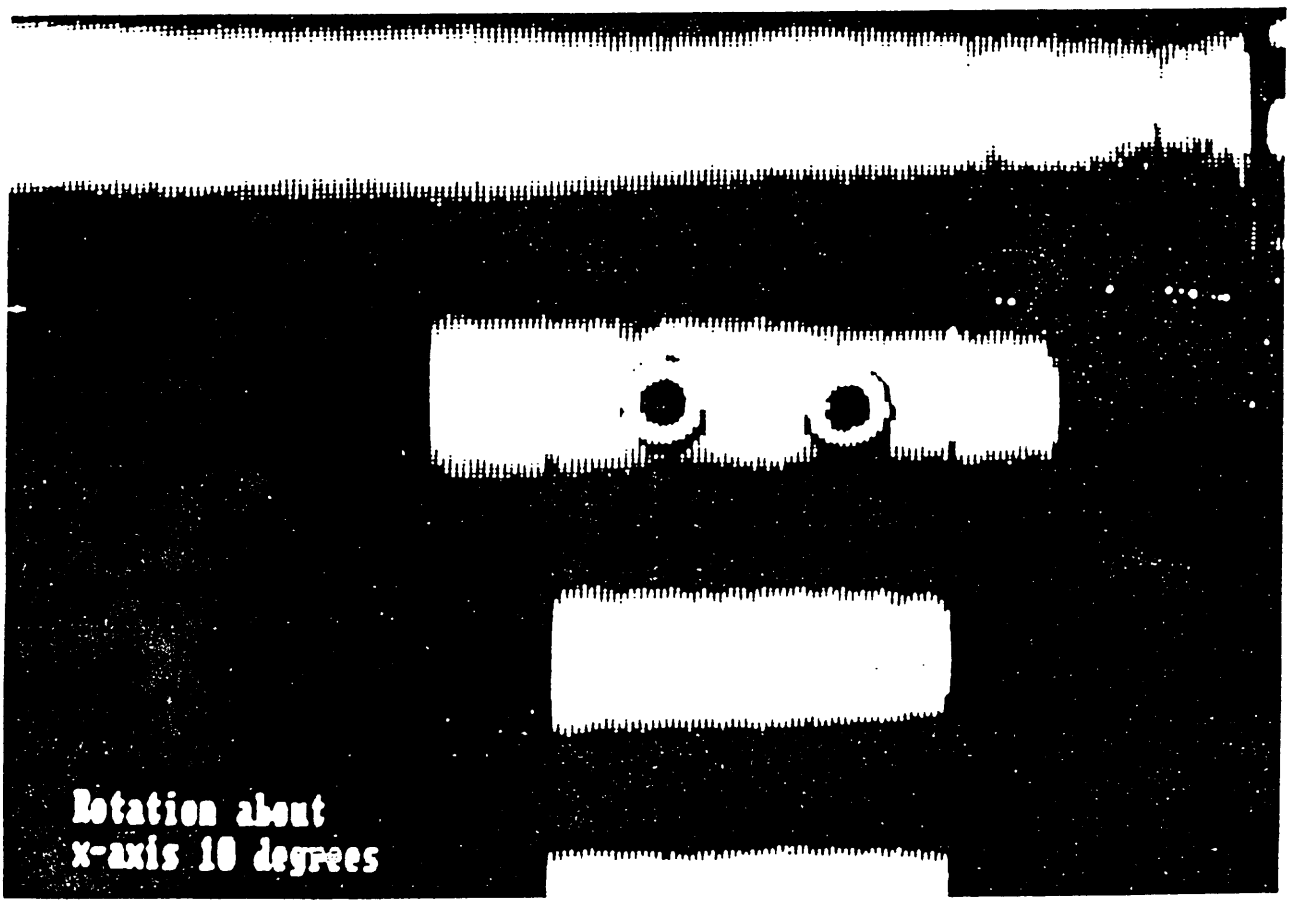

Figure 6b. Rotating plane calibration ruler positioned to rotate about the x-axis, α = 10 degrees.

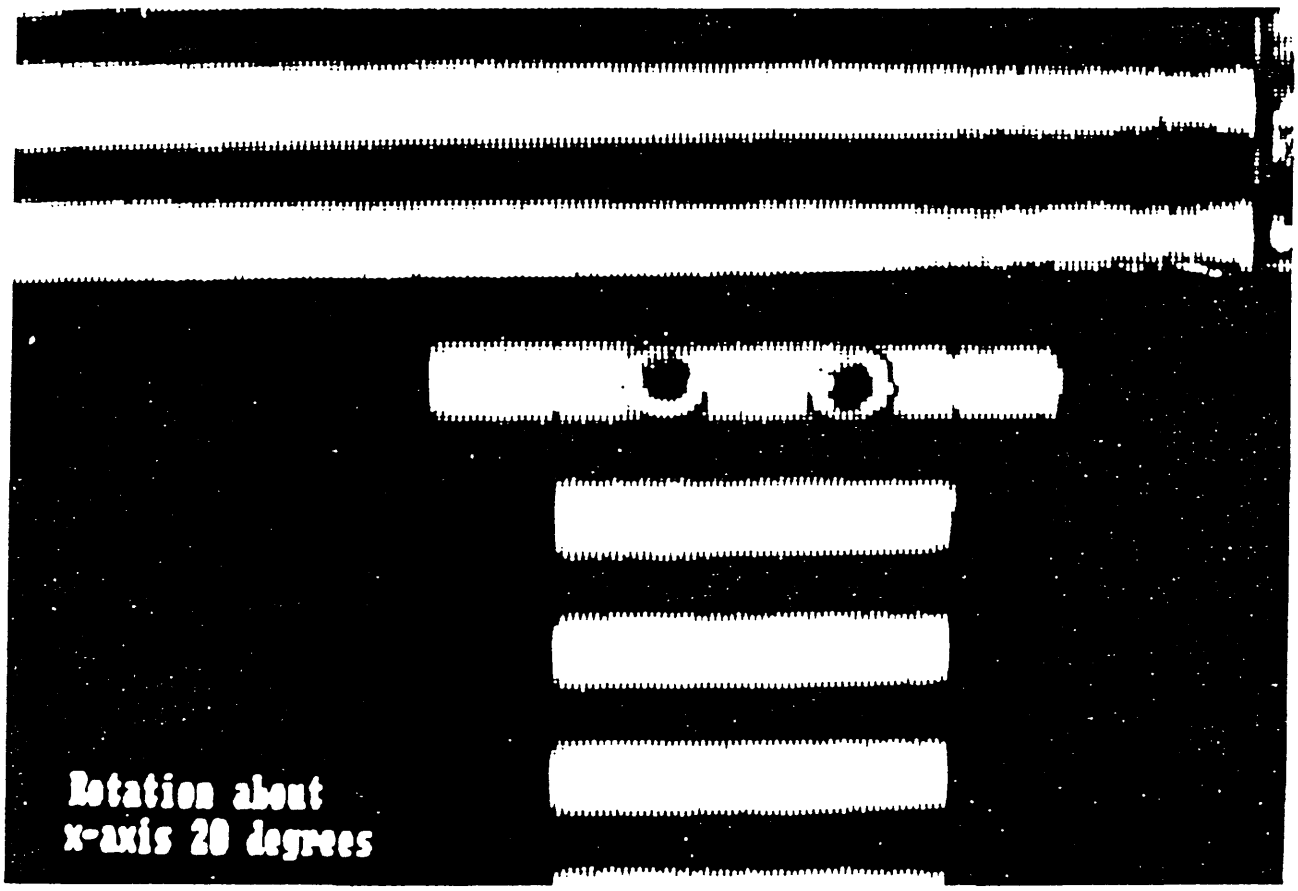

Figure 6c. Rotating plane calibration ruler positioned to rotate about the x-axis, α = 20 degrees.

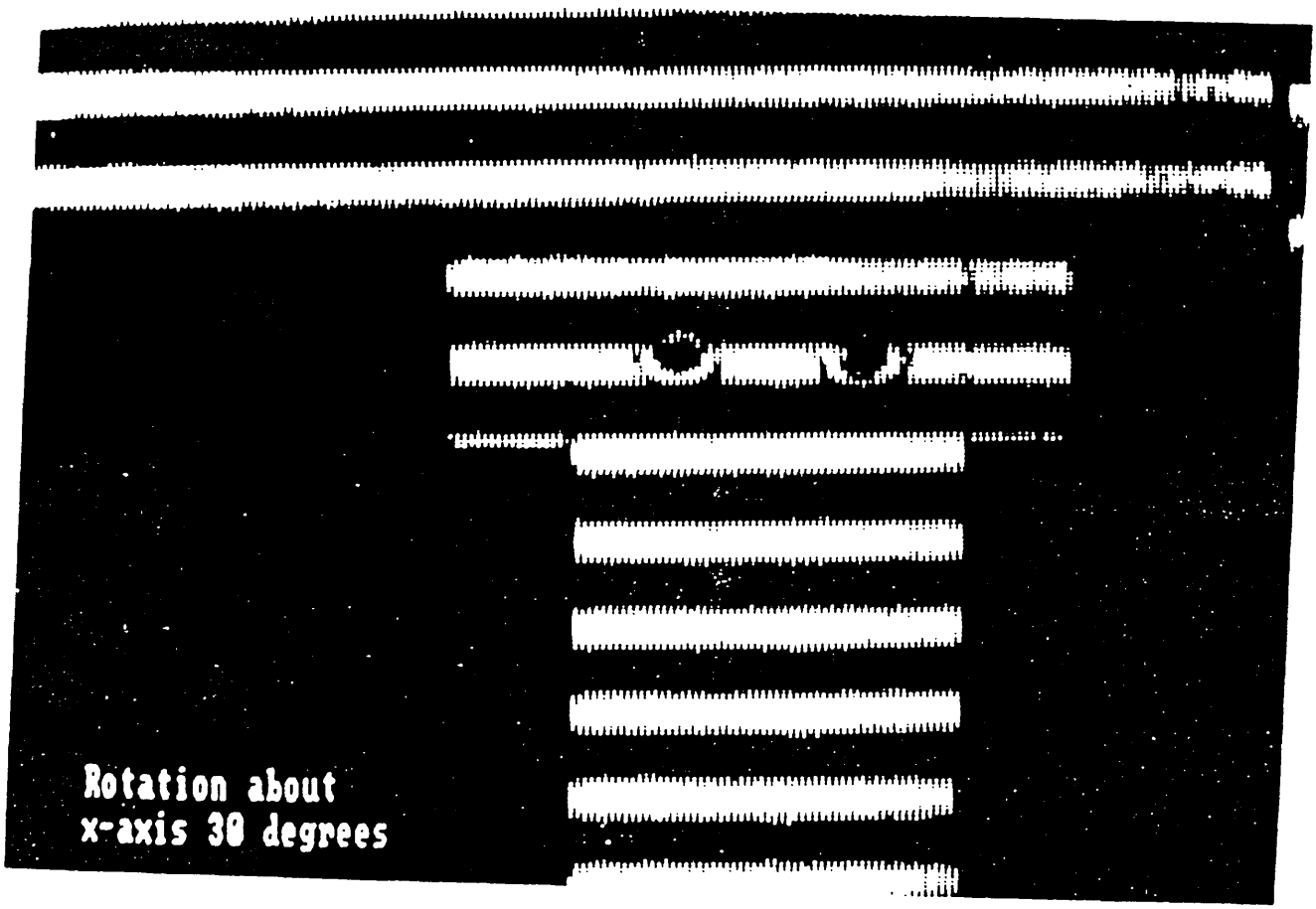

Figure 6d. Rotating plane calibration ruler positioned to rotate about the x-axis, α = 30 degrees.

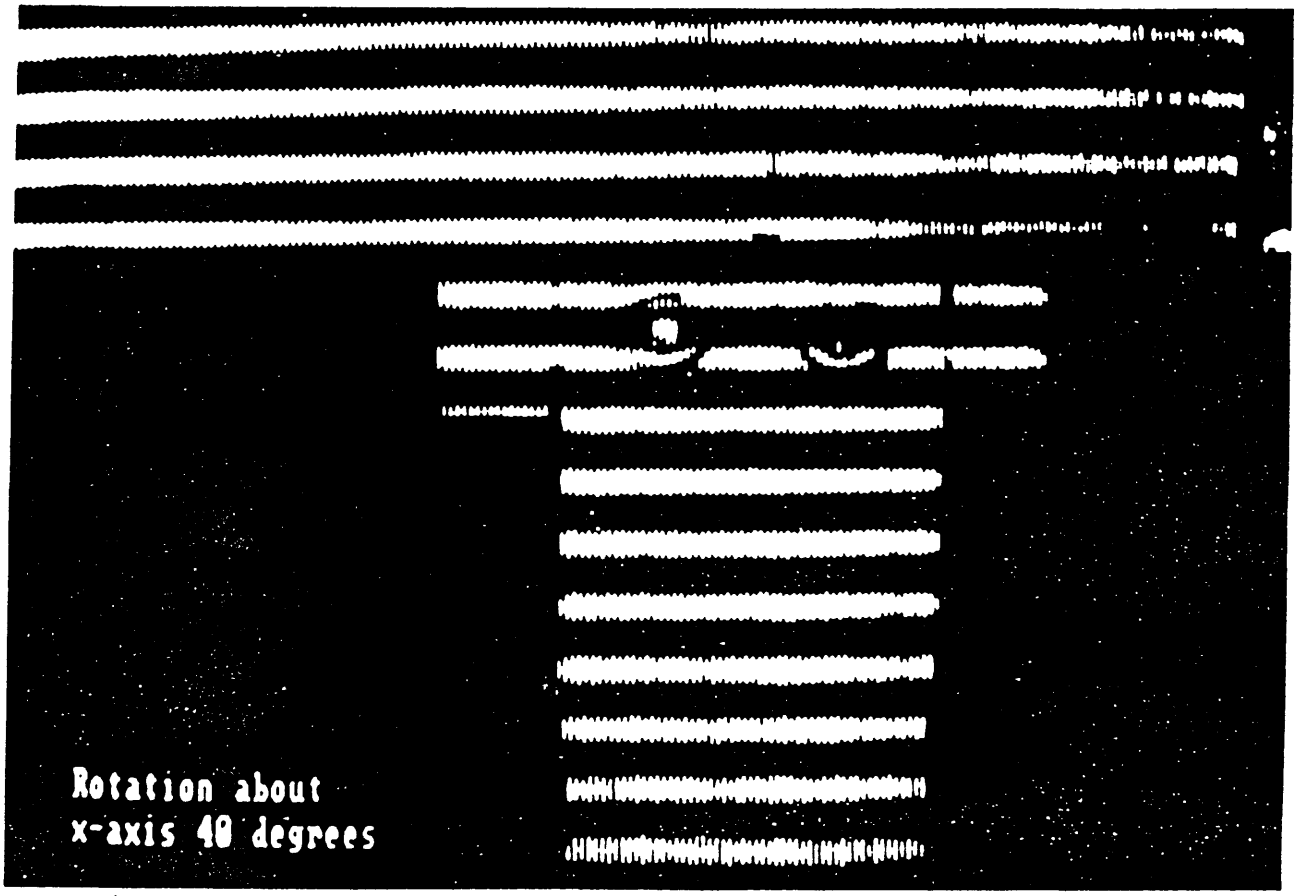

Figure 6e. Rotating plane calibration ruler positioned to rotate about the x-axis, α = 40 degrees.

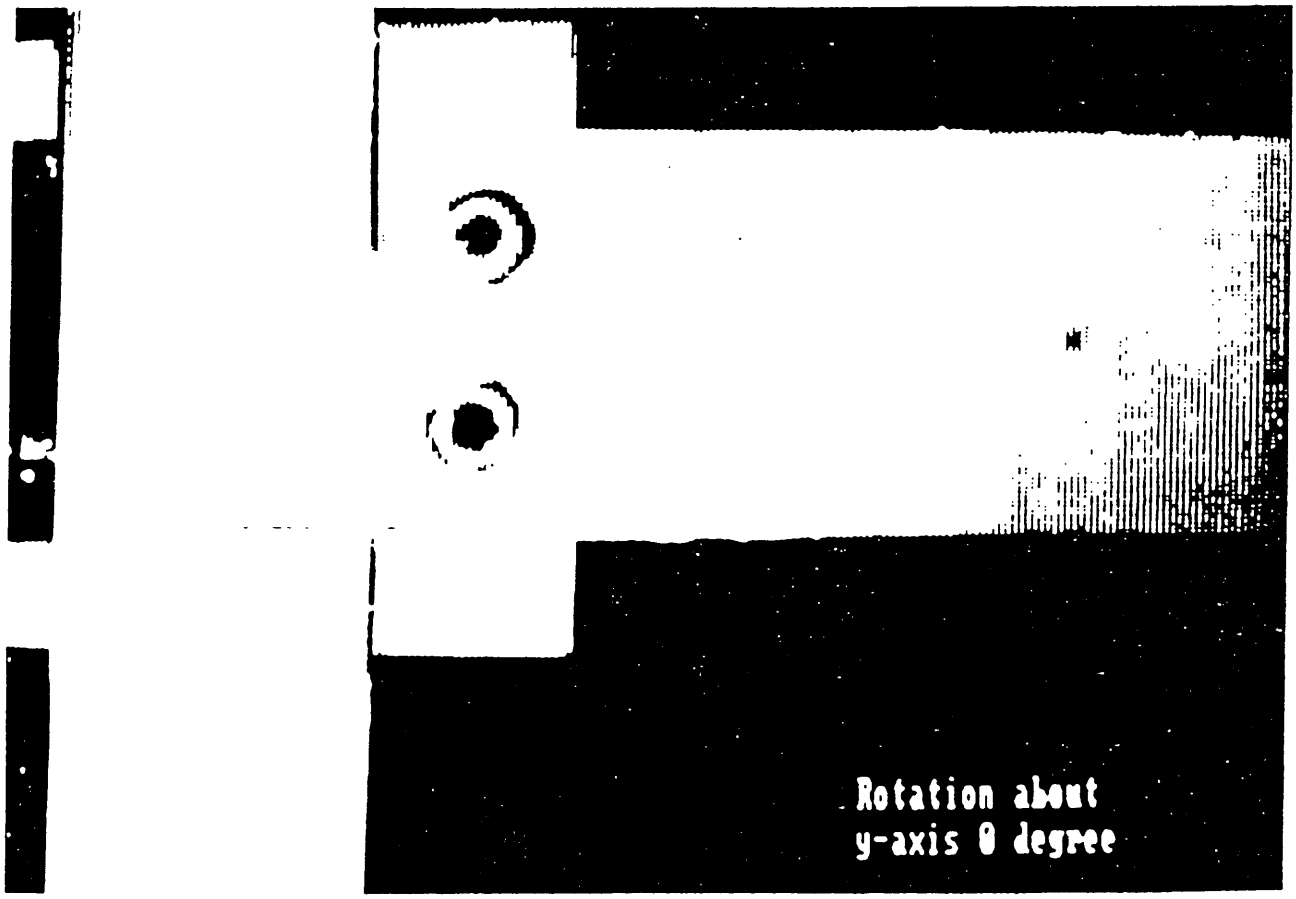

Figure 7a. Rotating plane calibration ruler positioned to rotate about the y-axis, α = 0 degrees.

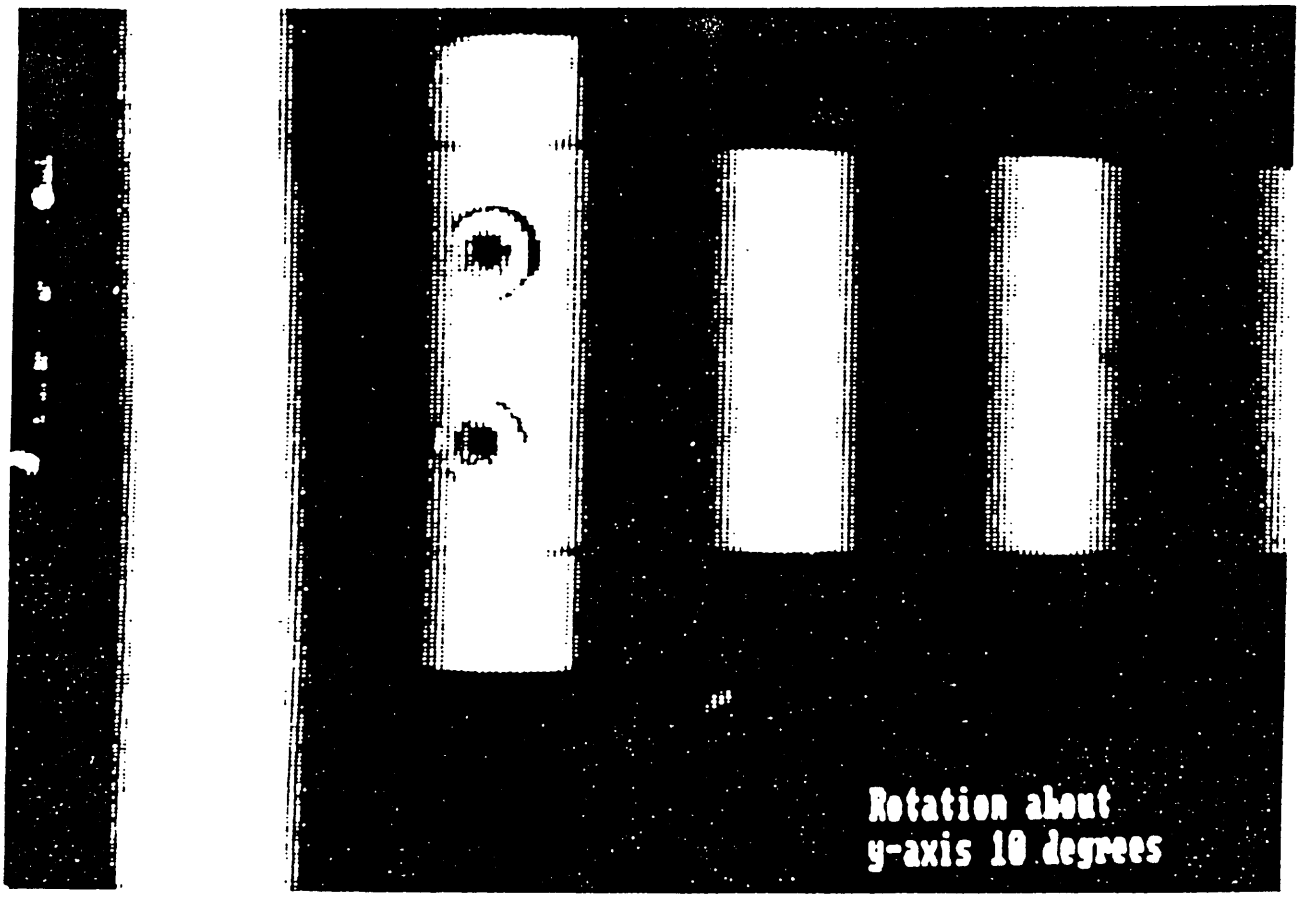

Figure 7b. Rotating plane calibration ruler positioned to rotate about the y-axis, α = 10 degrees.

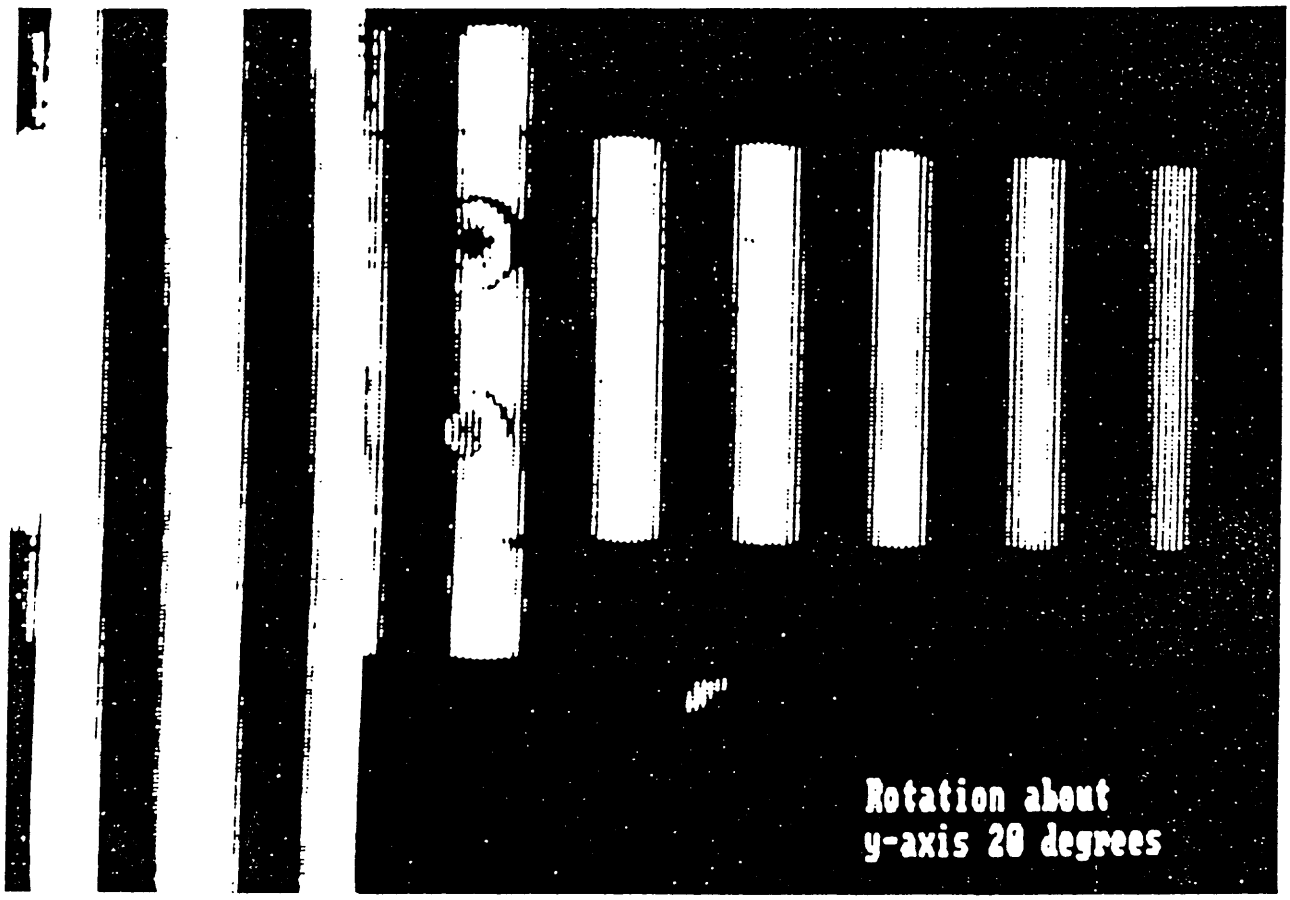

Figure 7c. Rotating plane calibration ruler positioned to rotate about the y-axis, α = 20 degrees.

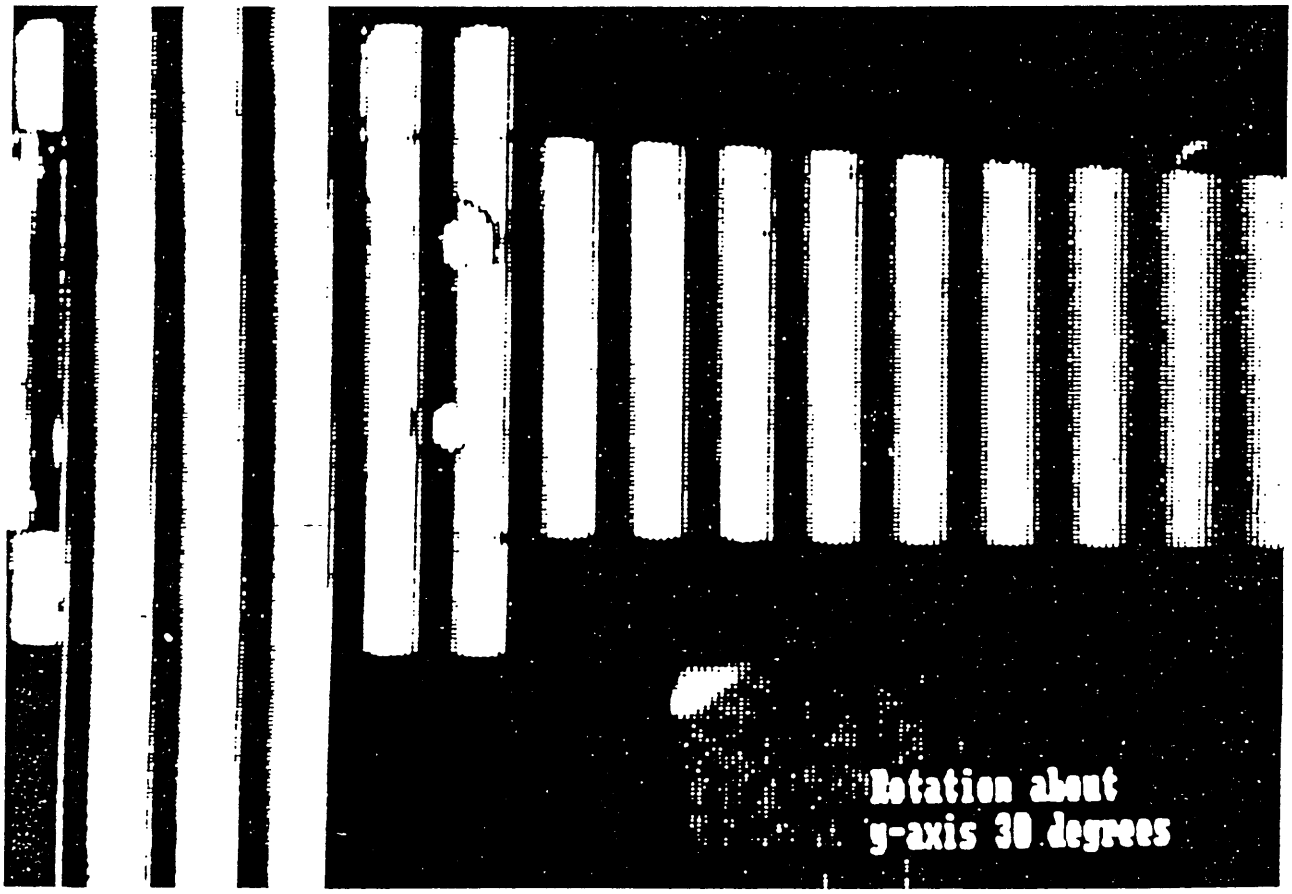

Figure 7d. Rotating plane calibration ruler positioned to rotate about the y-axis, α = 30 degrees.

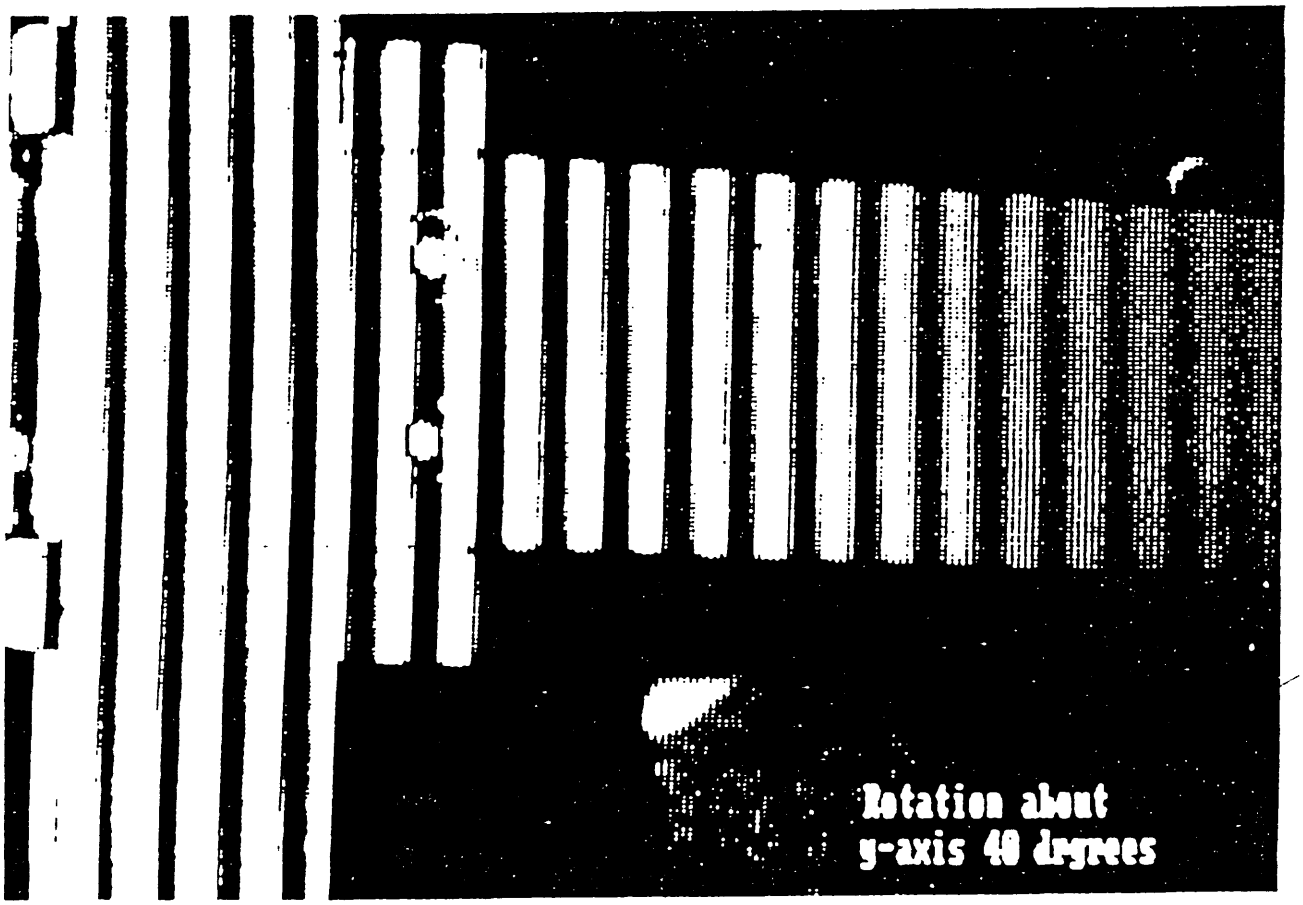

Figure 7e. Rotating plane calibration ruler positioned to rotate about the y-axis, α = 40 degrees.

Also, for the case of the tilted plane, Δz_e, the distance between two fringe center points along the z-direction is calculated using the following relationship, which is obtained from geometrical considerations,

$$\Delta z_e = z_0 \left[\frac{1}{\left(\frac{f}{x_B * \tan\alpha} - 1 \right)} - \frac{1}{\left(\frac{f}{x_A * \tan\alpha} - 1 \right)} \right] \qquad (11)$$

where α is the tilt angle from the base plane and x_A and x_B locate the centers of two adjacent fringes.

After the projection moire image is obtained for a particular orientation of the rotating plane calibration ruler, it is averaged to eliminate the high-frequency noise on the digitized image. Then a window is defined on the image that encloses the image area to be analyzed. After entering the basic experimental set-up parameters into a computer program, the data analysis is then performed automatically. It is possible to analyze experimental results for 10, 20, 30, and 40 degrees using the rotating plane calibration ruler and this approach. Table 1 summarizes the results at each of the positions of the rotating plane calibration ruler about the y-axis. The following two equations were used to determine the error, e_i, and the statistical error, e_s, respectively,

and

$$e_i = \left(\frac{\Delta Z_e - \Delta Z_t}{\Delta Z_t} \right) x\ 100\% \qquad (12a)$$

$$e_s = \sqrt{\frac{\sum_{i=1}^{n} e_i^2}{n-1}} \, .$$

Table 1 identifies the fringe numbers for the fringes visible in the field of view, the center of the fringe location in terms of a pixel number, the experimentally obtained distance between fringes, Δz_e, and the theoretically obtained distance between fringes, Δz_t. Additionally, the error and statistical error are listed. Table 2 summarizes the average values of error and statistical error from which a judgment of the relative accuracy of the experimental set-up can be made. The statistical error for a plane rotated about the x-axis is 3.12 percent and about the y-axis is 2.13 percent. This difference in results may be attributed to a difference in size between the vertical and horizontal dimensions of the pixels in the CCD camera, that is, the vertical pixel size is larger than the horizontal pixel size.

Table 1. Results of using the rotating plane calibration ruler positioned to rotate about the y-axis [The theoretically obtained distances between the fringes are Δz_e (fringe center points) and Δz_t (adjacent fringes); mm, millimeters. Parameters for the experimental setup: λ, 55.00 mm; m_1, 11.22; z_0, 671.90 mm; f, 59.90 mm; υ, 20 lines per mm; B, 91.40 mm; n_b, 162.48.]

Fringe number	Pixel number	Δz_e (mm)	Δz_t (mm)	Error (percent)
		α = 10 degrees		
		(Statistical error, e_s, is 2.96 percent)		
163	231	4.12	4.07	1.27
164	375	3.88	4.02	-3.66
165	512	4.11	3.97	3.34
		α = 20 degrees		
		(Statistical error, e_s, is 2.71 percent)		
162	120	4.17	4.12	1.07
163	191	4.11	4.07	1.00
164	262	4.00	4.02	-0.49
165	332	3.84	3.97	-3.36
166	400	3.96	3.93	0.86

Table 1 (continued). Results of using the rotating plane calibration ruler positioned to rotate about the y-axis [The theoretically obtained distances between the fringes are Δz_e (fringe center points) and Δz_t (adjacent fringes); mm, millimeters. Parameters for the experimental setup: λ, 55.00 mm; m_1, 11.22; z_0, 671.90 mm; f, 59.90 mm; υ, 20 lines per mm; B, 91.40 mm; n_b, 162.48.]

Fringe number	Pixel number	Δz_e (mm)	Δz_t (mm)	Error (percent)
	α = 20 degrees (continued)			
	(Statistical error, e_s, is 2.71 percent)			
167	471	3.64	3.88	-6.27
168	537	3.87	3.83	0.80
169	608	3.71	3.79	-2.09
	α = 30 degrees			
	(Statistical error, e_s, is 2.15 percent)			
161	86	4.24	4.17	1.53
162	132	4.09	4.12	-0.78
163	177	4.13	4.07	1.32
164	223	3.98	4.02	-0.98
165	268	3.93	3.97	-1.07
166	313	3.80	3.93	-3.33
167	357	3.92	3.88	0.98

Table 1 (continued). Results of using the rotating plane calibration ruler positioned to rotate about the y-axis [The theoretically obtained distances between the fringes are Δz_e (fringe center points) and Δz_t (adjacent fringes); mm, millimeters. Parameters for the experimental setup: λ, 55.00 mm; m_1, 11.22; z_0, 671.90 mm; f, 59.90 mm; υ, 20 lines per mm; B, 91.40 mm; n_b, 162.48.]

Fringe number	Pixel number	Δz_e (mm)	Δz_t (mm)	Error (percent)
	α = 30 degrees (continued)			
	(Statistical error, e_s, is 2.15 percent)			
168	403	3.78	3.83	-1.31
169	448	3.74	3.79	-1.39
170	493	3.61	3.74	-3.65
171	537	3.57	3.70	-3.70
172	581	3.76	3.66	2.78
173	628	3.56	3.62	-1.70
	α = 40 degrees			
	(Statistical error, e_s, is 1.47 percent)			
161	105	4.16	4.17	-0.40
162	137	4.10	4.12	-0.54
163	169	4.04	4.07	-0.68
164	201	3.99	4.02	-0.82

Table 1 (continued). Results of using the rotating plane calibration ruler positioned to rotate about the y-axis [The theoretically obtained distances between the fringes are Δz_e (fringe center points) and Δz_t (adjacent fringes); mm, millimeters. Parameters for the experimental setup: λ, 55.00 mm; m_1, 11.22; z_0, 671.90 mm; f, 59.90 mm; υ, 20 lines per mm; B, 91.40 mm; n_b, 162.48.]

Fringe number	Pixel number	Δz_e (mm)	Δz_t (mm)	Error (percent)
		α = 40 degrees (continued)		
		(Statistical error, e_s, is 1.47 percent)		
165	233	3.94	3.97	-0.95
166	265	3.88	3.93	-1.09
167	297	3.83	3.88	-1.22
168	329	3.78	3.83	-1.35
169	361	3.73	3.79	-1.48
170	393	3.69	3.75	-1.61
171	425	3.75	3.70	1.32
172	458	3.59	3.66	-1.89
173	490	3.54	3.62	-2.01
174	522	3.50	3.58	-2.13
175	554	3.46	3.54	-2.25
176	586	3.41	3.50	-2.37
177	618	3.48	3.46	0.55

Table 2. Summary of error results of using the rotating plane calibration ruler positioned to rotate about the x- and y-axis [Parameters for the experimental setup: λ, 55.00 mm; υ, 20 lines per mm; B, 91.40 mm; for the x-axis, m_f, 11.08; z_0, 664.28 mm; f, 59.97 mm; n_b, 164.51; and for the y-axis, m_f, 11.22; z_0, 671.90 mm; f, 59.90 mm; n_b, 162.48.]

Rotational plane angle (α, in degrees)	Axis of rotation	
	x-axis	y-axis
10	4.27	2.96
20	3.46	2.71
30	3.25	2.15
40	2.54	1.47
Statistical error	3.12	2.13

Phase Measurement Between Fringes

Using more than one image with moire projection techniques can increase the accuracy of the profile of an object. This approach works well in areas that are relatively flat and where the interval

between two fringes is large. To use this approach, several images with different phase information need to be obtained. The most convenient way to implement this phase change is by moving the translation stage along the z-axis, thus shifting the location of the base plane, with respect to the object. If the fringes and associated fringe numbers are tracked as they move, then it is possible to generate enough points on the object surface under study to assure accurate profiling. An assumption inherent in this procedure is that the motions along the z-axis are so small that they do not affect the experimental set-up calibration. Also, it has to be assumed that the center of the fringes is easily determined, especially for broad fringes.

Measurements Using A Cylindrical Specimen

After checking the accuracy and repeatability of the experimental set-up using the rotating plane calibration ruler, it is then possible to further check experimental results using a cylindrical specimen. The diameter, D_o, of the cylindrical specimen is 64.70 ± 0.0254 mm, and its length is 125.00 ± 0.1 mm. It is machined to this tolerance using a lathe and checked with a dial gage. The cylinder is positioned on the translation stage with its longitudinal axis parallel to the y-axis. The optical axis of the viewer is aligned, as closely as possible, with the center of the cylinder. The rotating plane calibration ruler is positioned to the right of the cylinder with its axis of rotation aligned parallel to the y-axis. A paper tape is used to connect the

rotating plane calibration ruler to the cylinder, as shown in figure 8, so as to transfer the fringe number from the calibration ruler to the object of interest, that is, the cylinder. For this case, the fringe numbering also is very predictable once the fringe number is transferred from the calibration ruler.

An initial analysis of the fringe positions is performed along a horizontal line toward the top of the image of the cylinder (fig. 8, line number 1), after the fringe numbers have been transferred from the calibration ruler to the cylinder. Before actual data collection, each image is averaged to eliminate the high frequency noise on the digitized image. To obtain additional points on the cylinder surface and check the results, the specimen is moved eight times in 0.500 ± 0.001-mm increments along the z-axis of the projection moire experimental set-up. By translating the specimen 4.000 mm, more than 100 data points are collected for the cross section considered. Figures 9(a) and 9(b) show the moire fringes after moving the cylinder toward and away from the viewer, respectively. In this way, it is possible to generate the (x,y,z) coordinates of many experimentally measured points on the surface of the cylinder at a particular vertical location. Figure 10 shows the sampling of points and the cylindrical configuration that is generated along cross section 1, shown in figure 8. The equation for the surface of the cylinder is

$$(x-x_c)^2 + (z-z_c)^2 = \left(\frac{D_o}{2}\right)^2 \qquad (13)$$

where x_c and z_c, the coordinates at the center of the cylinder, equal 0.26 mm and 671.80 mm, respectively.

The data points taken at this location and two other locations on the cylinder, shown in figures 8, 9(a), and 9(b), are detailed in table 3. This table shows the results of analyzing nine separate images with different phase information, as explained above. Also listed are the number of experimental points considered for each image, the calculated radius of the cylinder obtained from the experimental data collected, R_e, and the statistical error, e_s. Given the (x_n,y_n,z_n) coordinates of every sampled point, the distance from each of these points to the center line of the cylinder can be calculated using

$$R_e = \sqrt{(X-X_c)^2+(Z-Z_c)^2}\,. \tag{14}$$

This experimentally obtained value of the cylinder radius, R_e, can be compared with the cylinder radius, $D_o/2$, and the statistical error, e_s, can be evaluated for every point (x_n,y_n,z_n). The statistical errors for each of the three cross sections considered are 0.49 percent, 0.47 percent and 0.53 percent, respectively. The average statistical error is 0.49 percent.

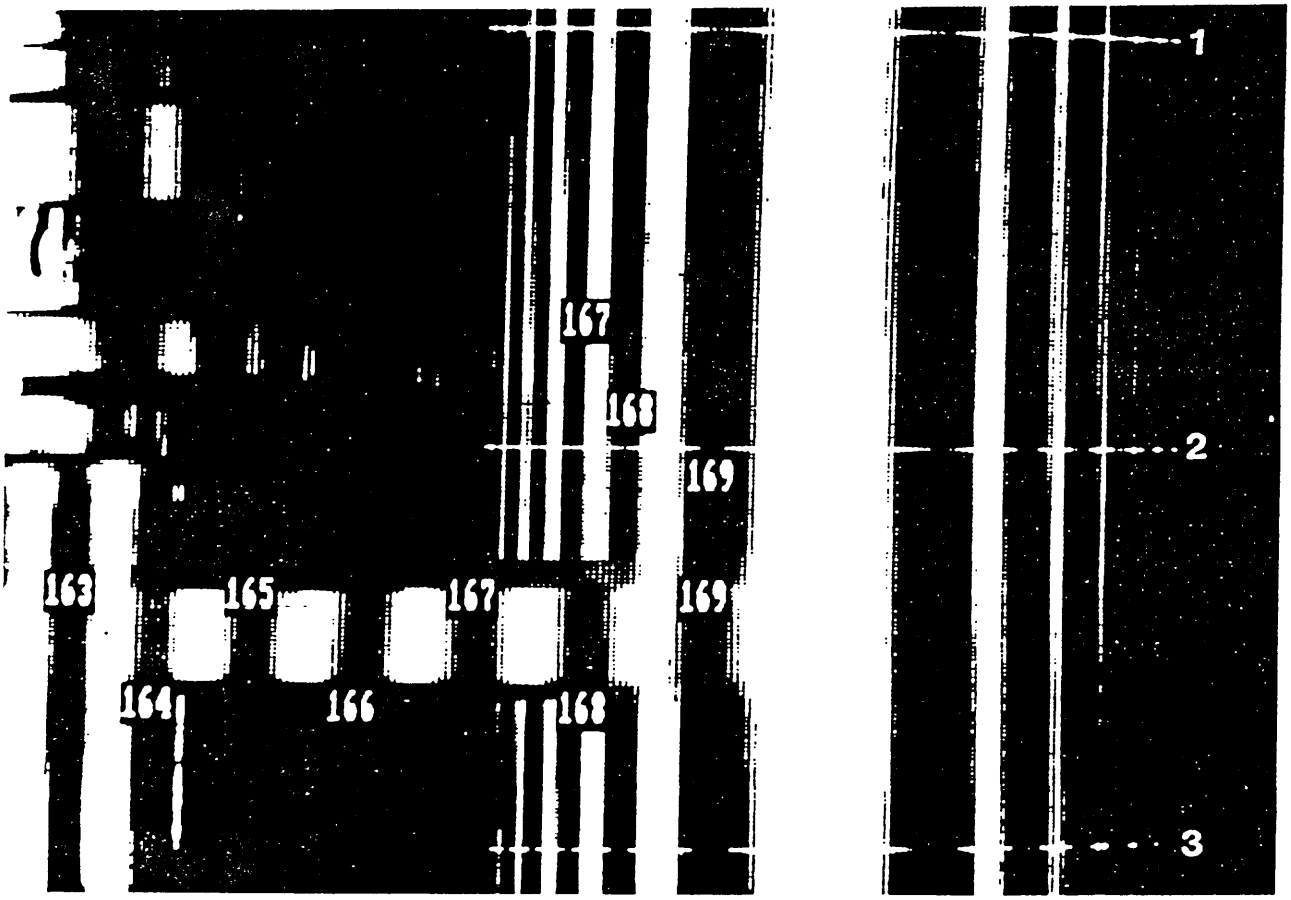

Figure 8. Transfer of the fringe number from the rotating plane calibration ruler to a cylindrical s.

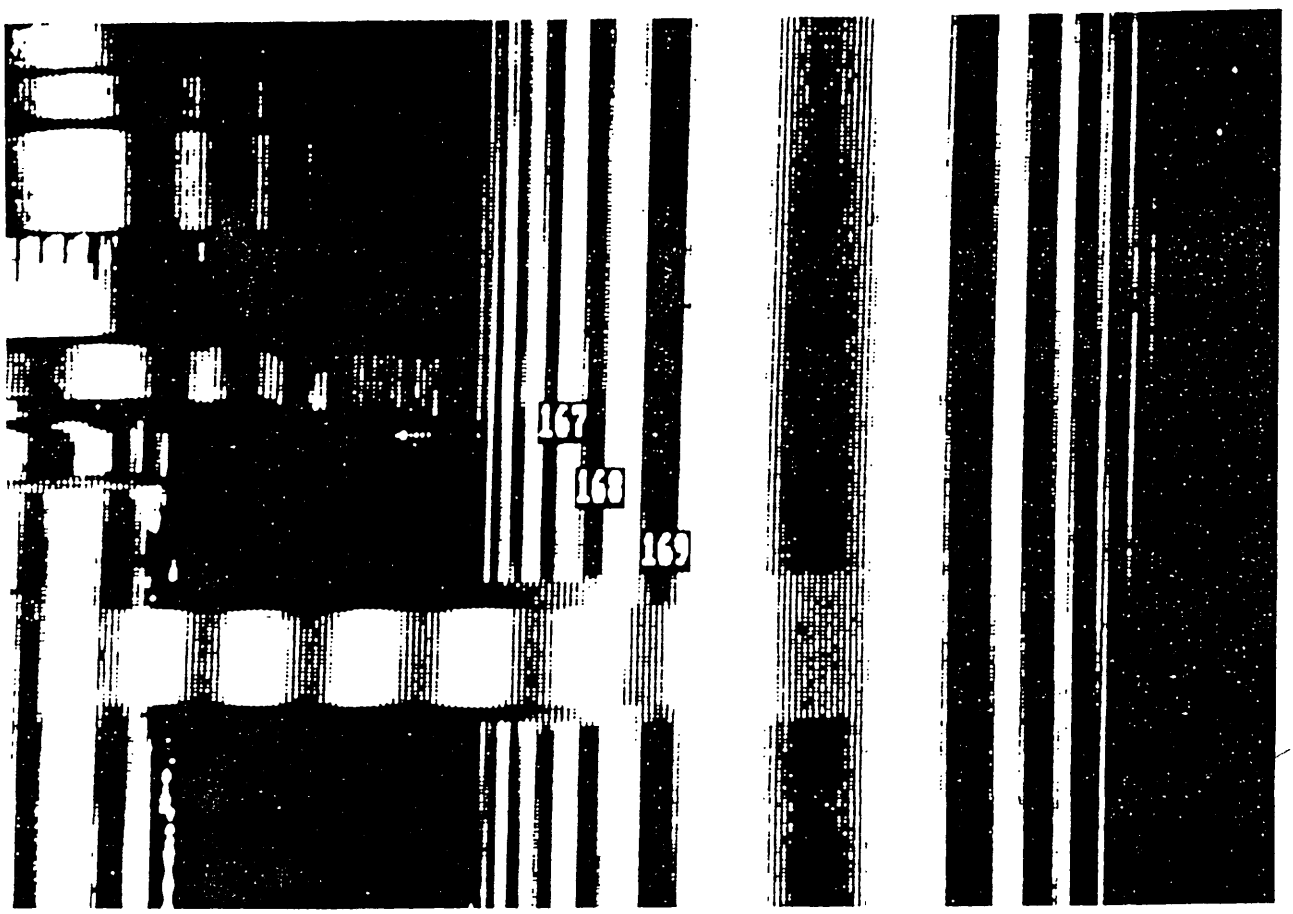

Figure 9a. Motion of moire fringes on a cylindrical surface translated along the z-axis (Δz = -1.500 ± 0.00 millimeters with respect to the reference position.)

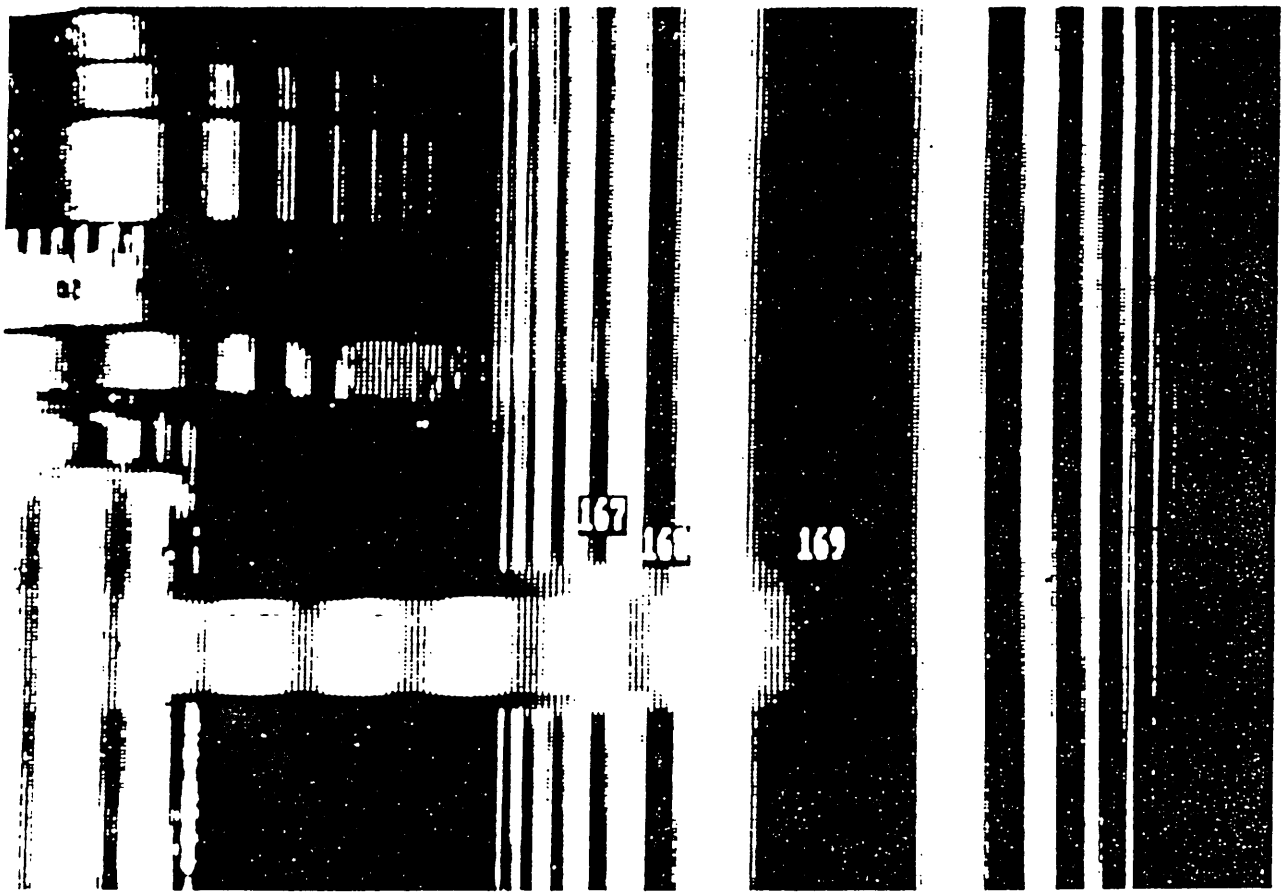

Figure 9b. Motion of moire fringes on a cylindrical surface translated along the z-axis (Δz = 1.500 ± 0.001 millimeters with respect to the reference position.)

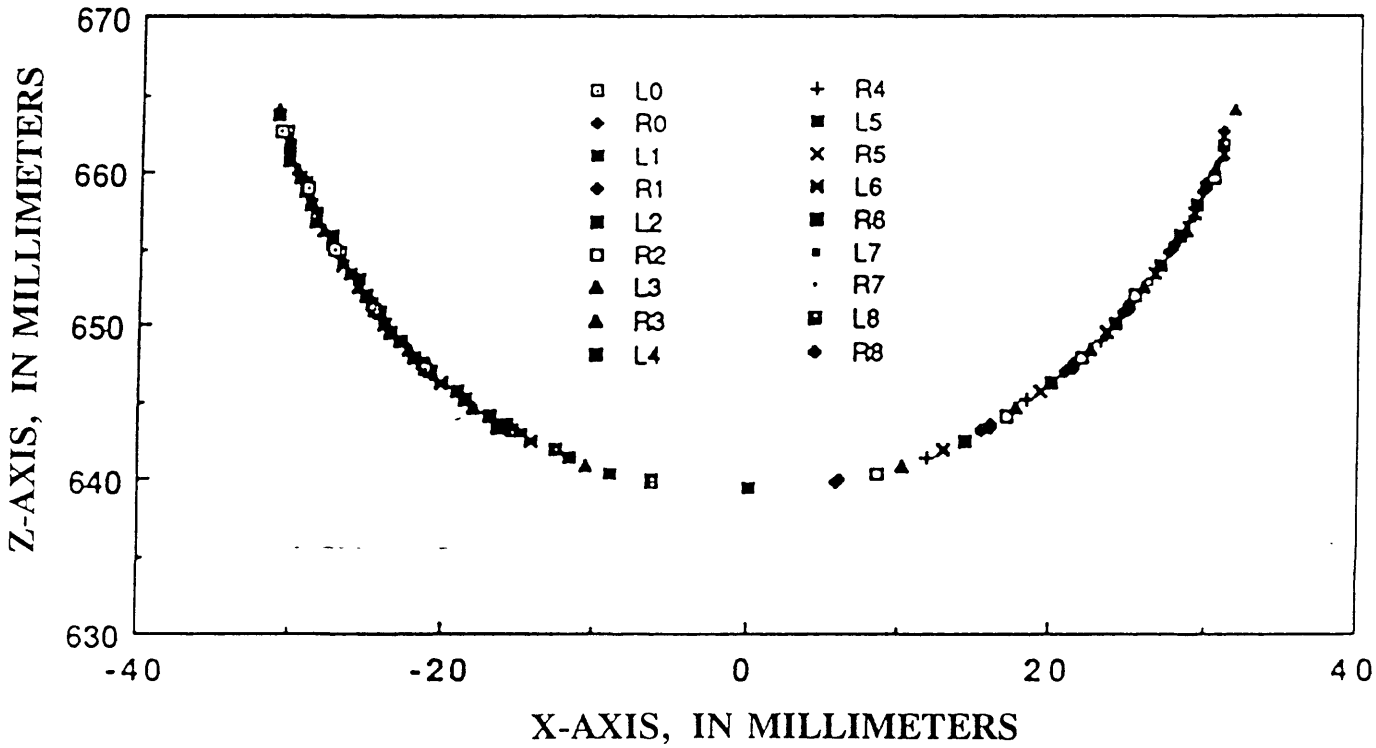

Figure 10. Reconstruction of the cylindrical surface using experimentally obtained data from analysis of moire fringe patterns. Nine scans were made of the left (L0 - L8) and right (R0 - L8) side of the cylinder.

Table 3. Results obtained from interrogating a cylindrical surface translated along the z-axis [Parameters for the experimental setup: λ, 55.00 mm; υ, 20 lines per mm; B, 91.40 mm; m_f, 11.21; z_0, 671.68 mm; f, 59.91 mm; n_b, 162.54.]

Image	Number of experimental points	Average cylinder radius, R_e, (mm)	Statistical error, e_s (percent)
	Horizontal cross section number 1		
	(Statistical error, e_s, is 0.49 percent)		
1	13	32.30	0.57
2	12	32.30	0.44
3	13	32.36	0.46
4	14	32.36	0.47
5	12	32.33	0.48
6	12	32.38	0.41
7	12	32.43	0.54
8	13	32.34	0.57
9	13	32.43	0.54
	Horizontal cross section number 2		
	(Statistical error, e_s, is 0.47 percent)		
1	13	32.29	0.48
2	12	32.27	0.48
3	13	32.36	0.50

Table 3 (continued). Results obtained from interrogating a cylindrical surface translated along the z-axis [Parameters for the experimental setup: λ, 55.00 mm; υ, 20 lines per mm; B, 91.40 mm; m_f, 11.21; z_0, 671.68 mm; f, 59.91 mm; n_b, 162.54.]

Image	Number of experimental points	Average cylinder radius, R_e, (mm)	Statistical error, e_s (percent)
Horizontal cross section number 2 (continued) (Statistical error, e_s, is 0.47 percent)			
4	14	32.40	0.47
5	12	32.35	0.48
6	12	32.38	0.41
7	12	32.44	0.54
8	12	32.38	0.57
9	13	32.42	0.54
Horizontal cross section number 3 (Statistical error, e_s, is 0.53 percent)			
1	13	32.35	0.60
2	12	32.28	0.47
3	13	32.40	0.66
4	14	32.37	0.61
5	12	32.31	0.48
6	12	32.35	0.53

Table 3 (continued). Results obtained from interrogating a cylindrical surface translated along the z-axis [Parameters for the experimental setup: λ, 55.00 mm; υ, 20 lines per mm; B, 91.40 mm; m_f, 11.21; z_0, 671.68 mm; f, 59.91 mm; n_b, 162.54.]

Image	Number of experimental points	Average cylinder radius, R_e, (mm)	Statistical error, e_s (percent)
Horizontal cross section number 3 (continued) (Statistical error, e_s, is 0.53 percent)			
7	12	32.38	0.48
8	11	32.37	0.56
9	14	32.39	0.49

Concavity and Convexity Measurements

From the calibration results using a rotating plane calibration ruler and the tests using a cylinder, it can be concluded that the accuracy of the experimental set-up is approximately 3 percent and can be used to determine the surface topography of different simple configurations. The main task is not the identification of the fringe number, which can easily be transferred from the rotating plane calibration ruler. Many other problems then become of primary concern, including the following: 1) making an automatic distinction between a depression and an

elevation from a contour map of the object; 2) assigning fringe orders automatically including those separated by discontinuities; 3) locating the center lines of broad fringes by correcting unwanted irradiance variations caused by nonuniform light reflection on the object surface; 4) interpolating in surface regions lying between contour lines; and 5) evaluating the existence of false or partially dark fringes.

Figure 11(a) shows what is defined as the base configuration of moire fringes for an artificially created surface composed of two-dimensional hills and valleys. The x-axis is oriented along the direction of the surface showing the most waviness. Next to the wavy surface is the rotating plane calibration ruler with its rotation axis parallel to the y-axis. Figures 11(b) and 11(c) show the same surface, except that the fringes have moved from their original positions (-1.000 ± 0.001 mm for figure 11(b) and 1.000 ± 0.001 mm for figure 11 (c)) due to moving the object along the z-axis. For the case where the object is moved toward the viewer (fig. 12), the fringes that lie on the hills of the object should move away from each other and those that lie on the valleys of the object should move toward each other, which is seen in figure 11(b) when it is compared to 11(a). The opposite would be true if the object were moved away from the viewer, which would be the case if figure 11(a) were taken as the reference position and compared to figure 11(c).

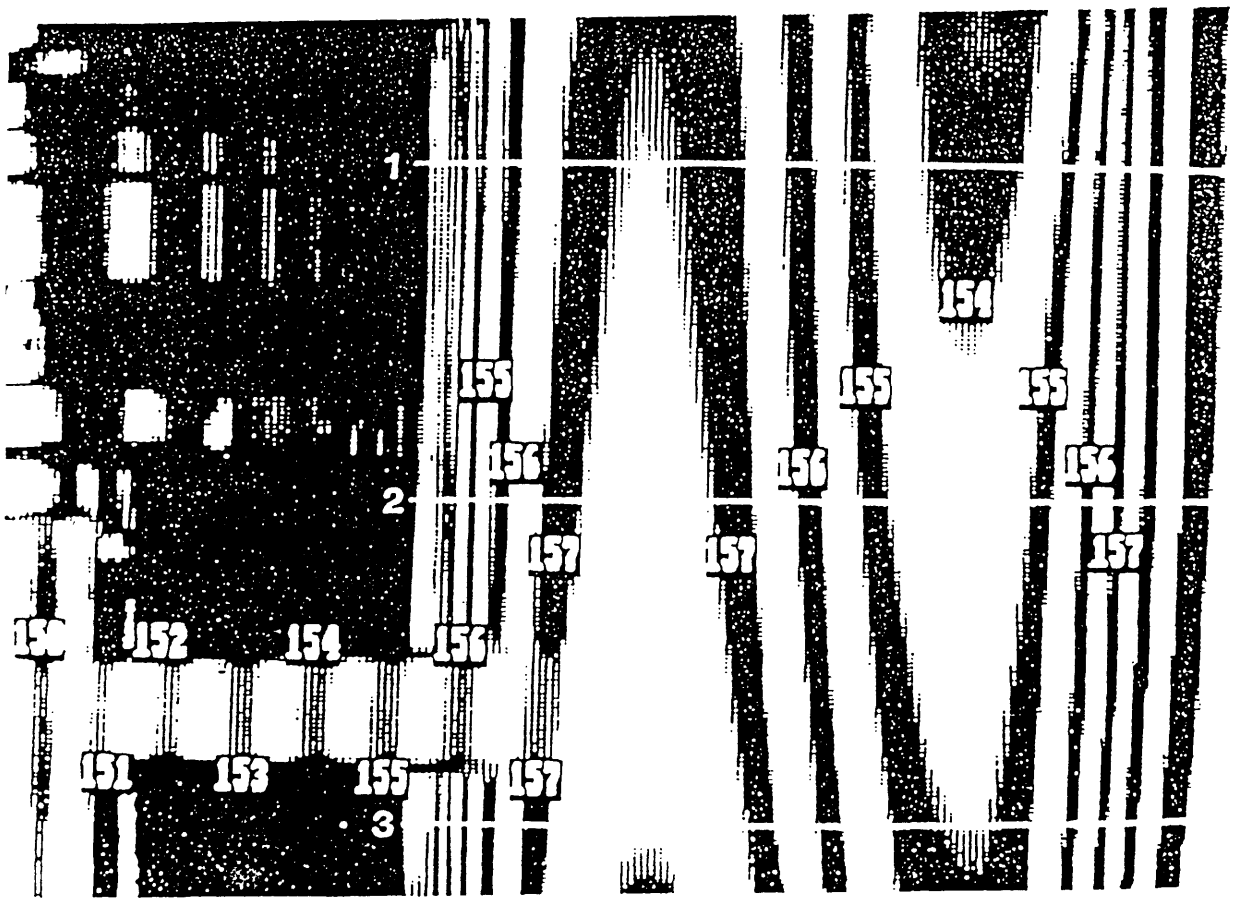

Figure 11a. Surface composed of concave-convex segments translated along the z-axis, reference position.

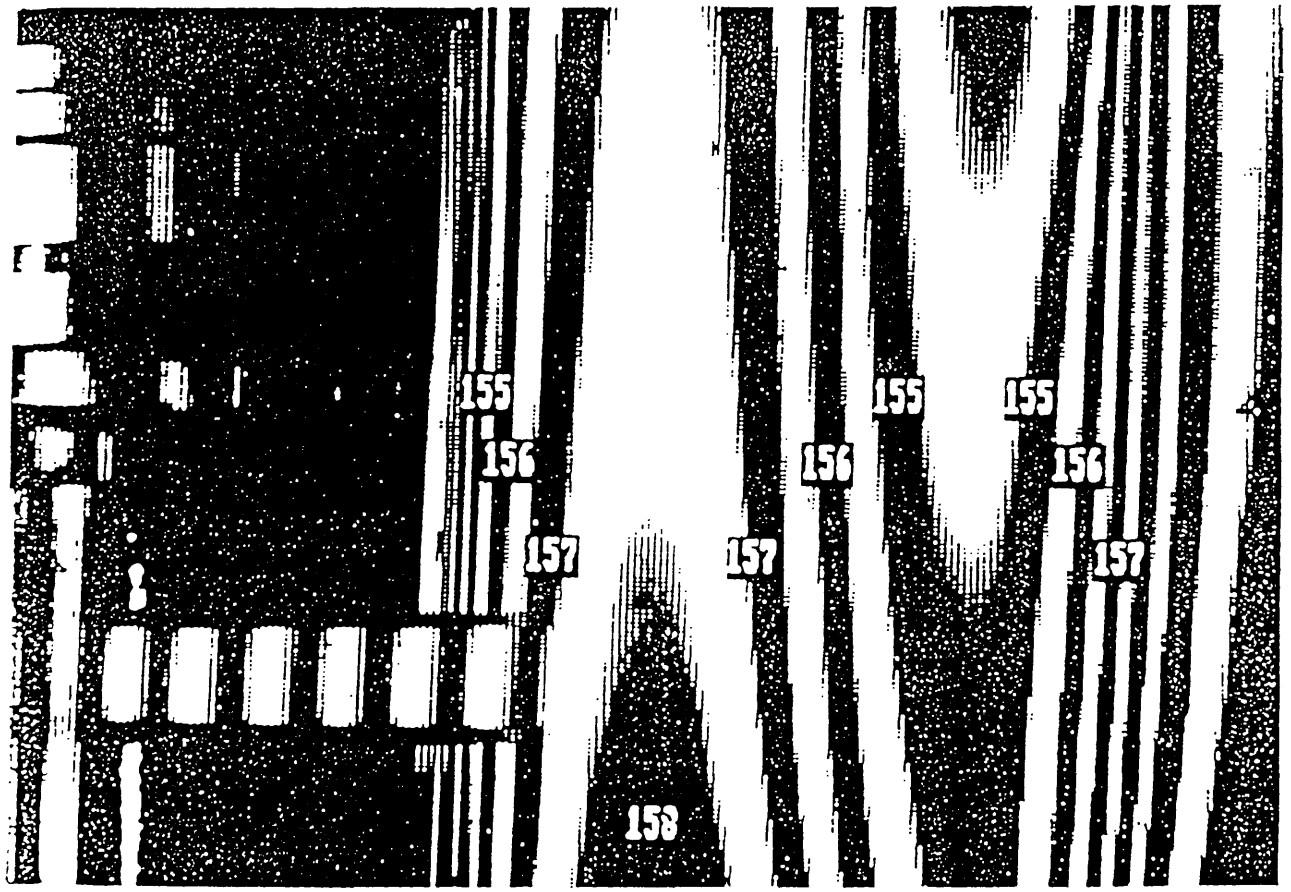

Figure 11b. Surface composed of concave-convex segments translated along the z-axis ($\Delta z = -1.000 \pm 0.001$ millimeters with respect to the reference position.)

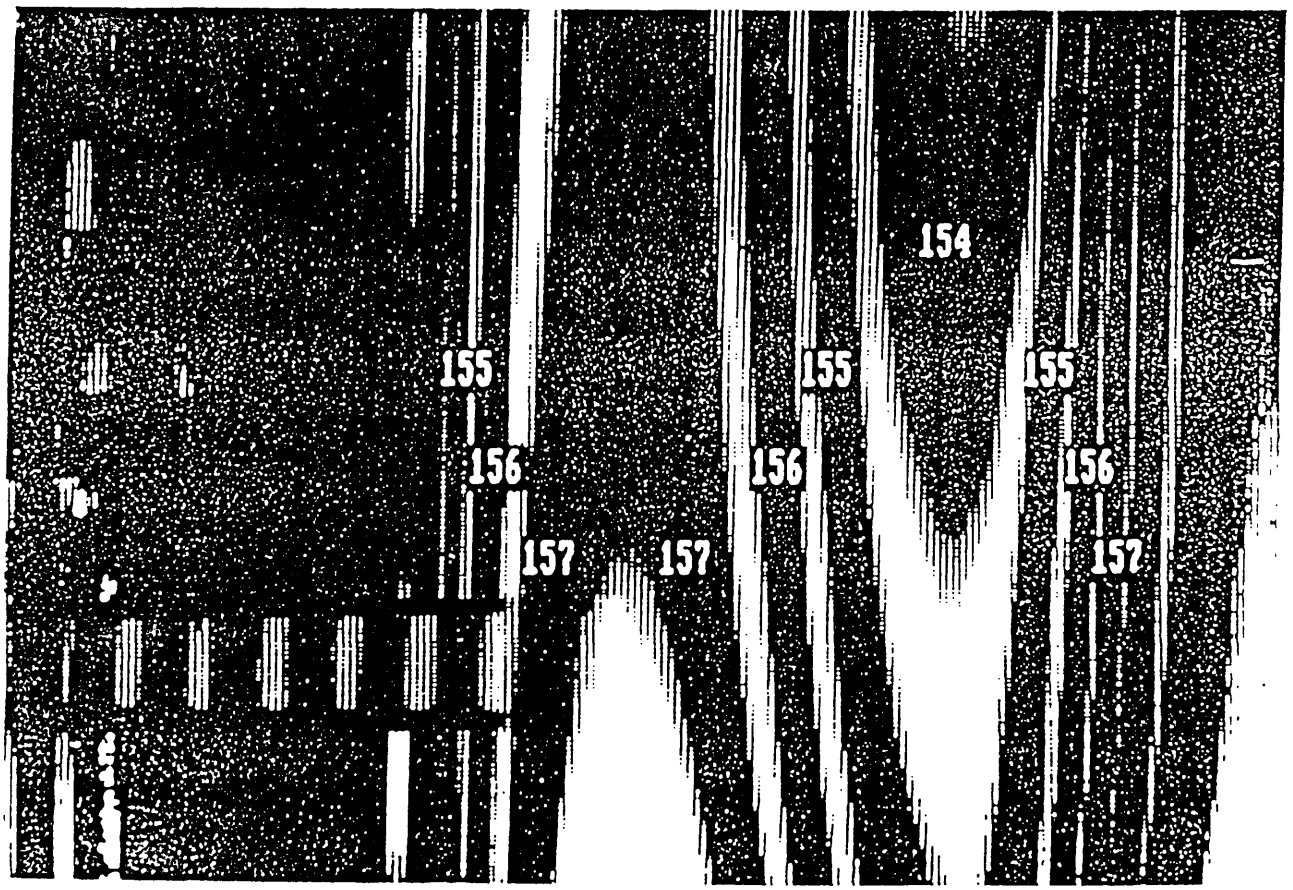

Figure 11c. Surface composed of concave-convex segments translated along the z-axis ($\Delta z = 1.000 \pm 0.001$ millimeters with respect to the reference position.)

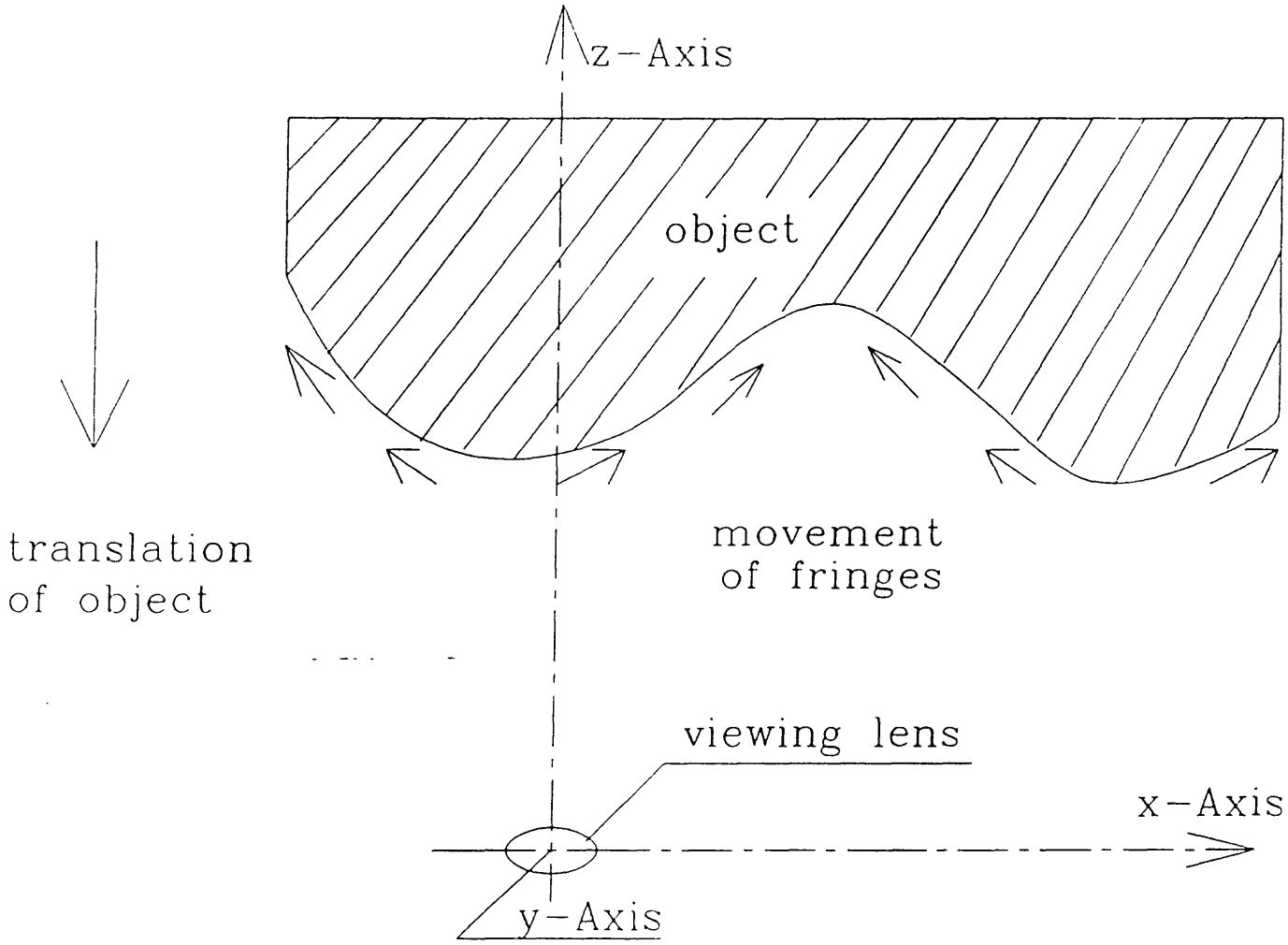

Figure 12. Schematic showing the relation between fringe movement and translation of object.

Using the automation capabilities of the experimental set-up, it is possible to locate the center of the fringes on the wavy surface and to number the fringes. By taking several images with differing phase and repeating this analysis, it is possible to better approximate the profile of the surface along the three cross sections shown in figure 11(a). Curve fitting can then be used to attempt a reconstruction of the actual profile of the curved surface, which is shown in figures 13(a) through 13(c). The profiles of the curved surface have been plotted using data obtained from computer analysis by moving the object in two increments forward and backward from a reference position along the z-axis. Because no independent verification of the surface profile was made, the accuracy of this determination depends on the previous calibration and on measurements performed on the rotating calibration plane ruler accuracy (upper limit) of 3.12 percent and the cylinder accuracy, approximately 0.5 percent.

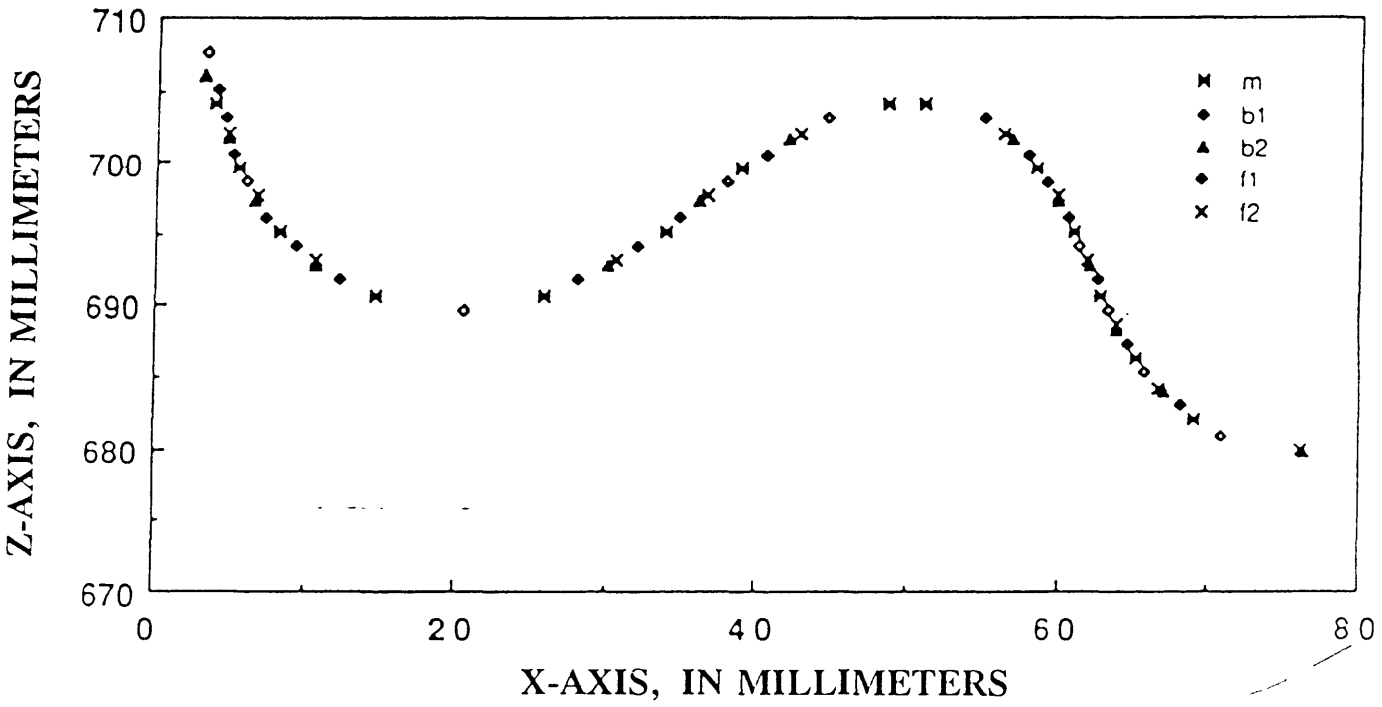

Figure 13a. Profile of the concave-convex surface along cross-section 1, using five separate scans (m, b1, b2, f1, and f2) with differing phases.

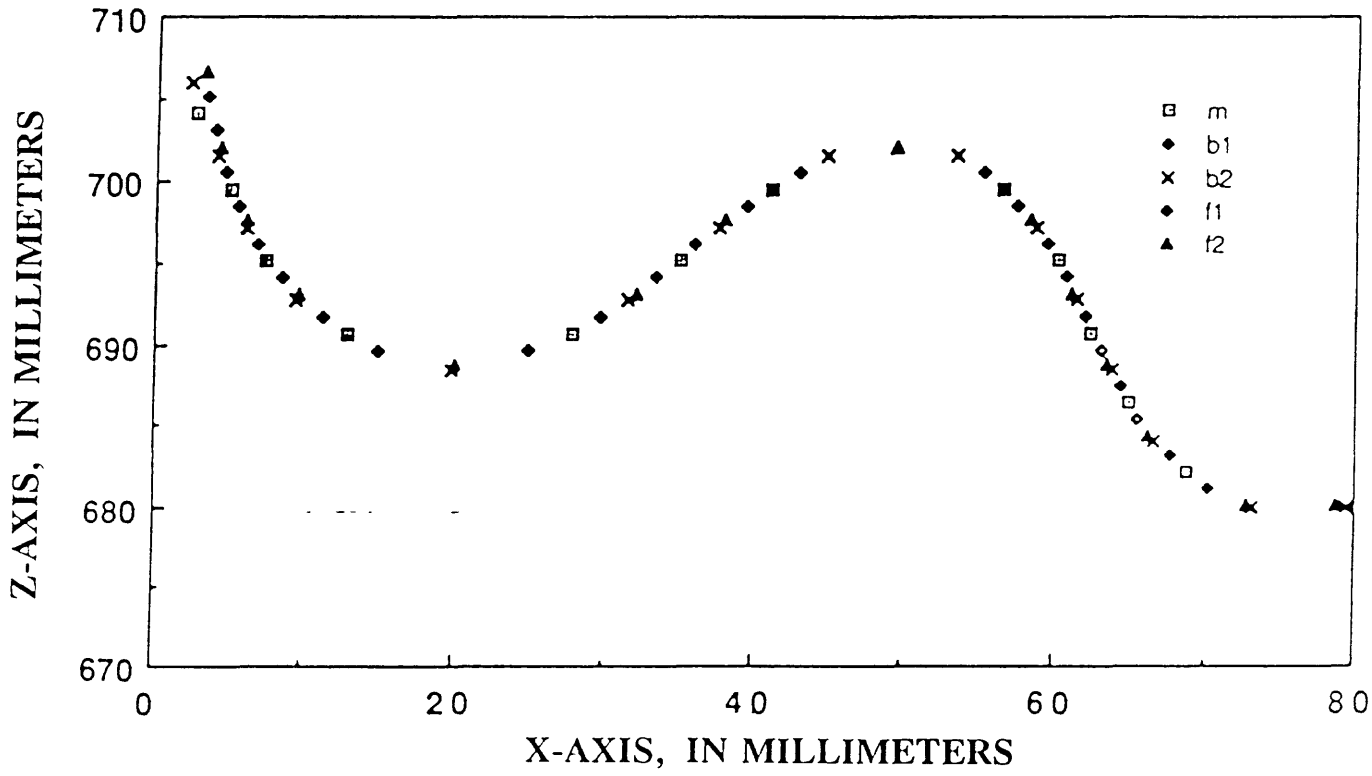

Figure 13b. Profile of the concave-convex surface along cross-section 2, using five separate scans (m, b1, b2, f1, and f2) with differing phases.

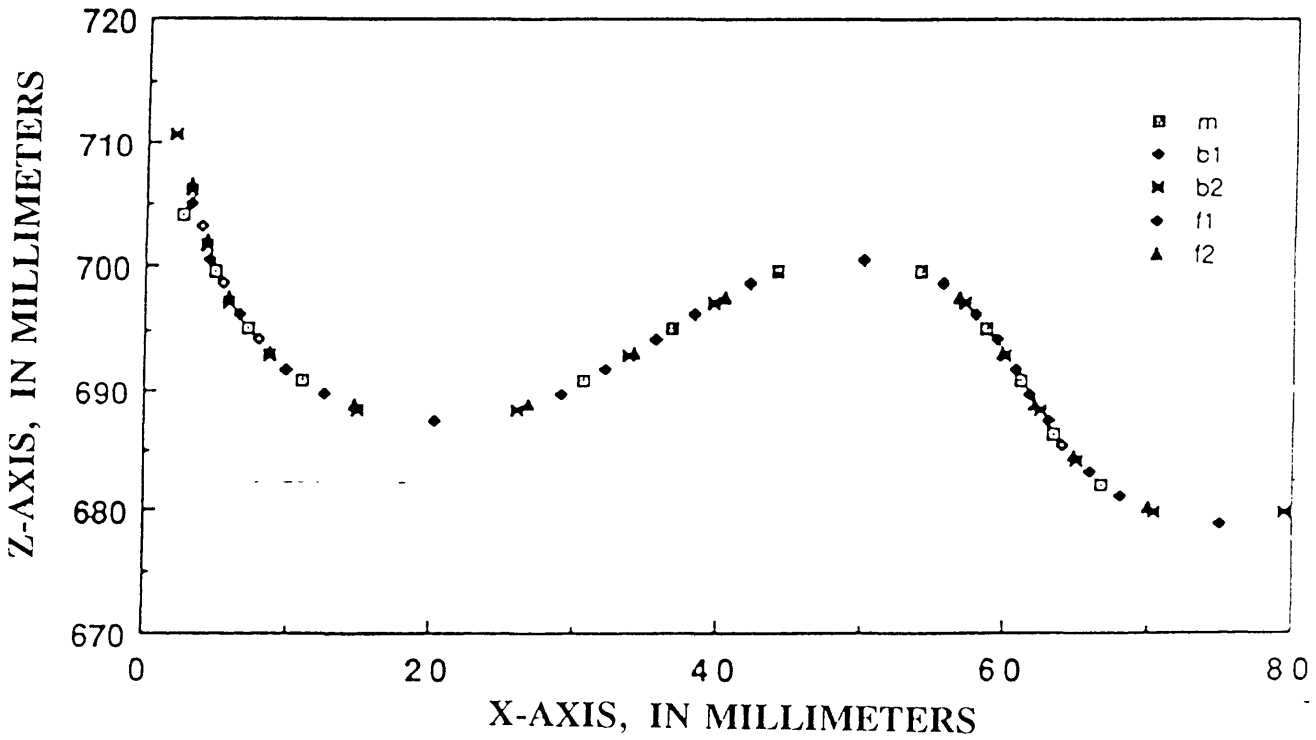

Figure 13c. Profile of the concave-convex surface along cross-section 3, using five separate scans (m, b1, b2, f1, and f2) with differing phases.

STEREO IMAGING FOR THREE-DIMENSIONAL RECONSTRUCTION OF OBJECT SURFACES

There are several optical, noncontact approaches for obtaining three-dimensional topographical data for objects, including shadow and projection moire methods (Meadows and others, 1970; Allen and Meadows, 1971; Takasaki, 1970, 1973), fast-Fourier transform approaches (Takeda and Mutoh, 1983), and stereo imaging (Barnea and Silverman, 1972; Marr and Poggio, 1979; Grimson, 1981, 1984, 1985; Frobin and Hierholzer, 1982; Kashef, 1983; Wu and others, 1983; Jain and others, 1987; Lee, 1990). Stereo imaging provides more direct, unambiguous, and quantitative depth information than for example, shadow moire. In addition, to three-dimensional topographic measurement, stereo imaging can be used for a wide range of applications, such as robotic vision, autonomous vehicle control, sight for the blind, remote sensing, and automated manufacturing.

Most approaches to the application of stereo imaging use human vision as a model for the camera system (see, for example, Kashef, 1983). Figure 14 shows the comparison between the human vision system and a camera system. The model consists of the object that is imaged by two cameras whose optical axes are usually parallel to each other. If only one camera is used to image the object, then either the object is moved slightly along a plane perpendicular to the camera optical axis, or the camera is moved laterally with

respect to its optical axis. In figure 14, two cameras (lenses 1 and 2) are translated laterally along the baseline. Lens 1 is translated from X_{1A} to X_{1B}. Lens 2 is translated from X_{2A} to X_{2B}. This translation results in a change in depth, D_z, along the parallel z-axes, Z_1 and Z_2, between the points A and B observed by lenses 1 and 2. In both instances, the imaged object remains in the camera field of view. Many different camera-object geometries have been used for specific applications such as, converging camera optical axes (Frobin and Hierholzer, 1982); camera translation along the optical axis (Jain and others, 1987); and rotating camera optical axis (Wu and others, 1983).

Once the camera-object geometry has been defined and two images of the object are obtained, it is then necessary to locate the same points on the two images. To do this manually for an entire image is very time intensive. Video imaging and digital image processing make the problem of finding similar points on two images less tedious for a human operator. The problem is when determining depth information it is necessary to find disparities, or translation differences, among a series of corresponding points between a pair of images taken from the same scene. There are many matching algorithms that can be used to perform these computer-intensive operations. In general, matching techniques and corresponding algorithms can be divided into three major categories: Area-based (Anuta, 1970; Barnea and Silverman, 1972; Barnard and Thompson, 1980; Grimson, 1984), feature-based (Grimson,

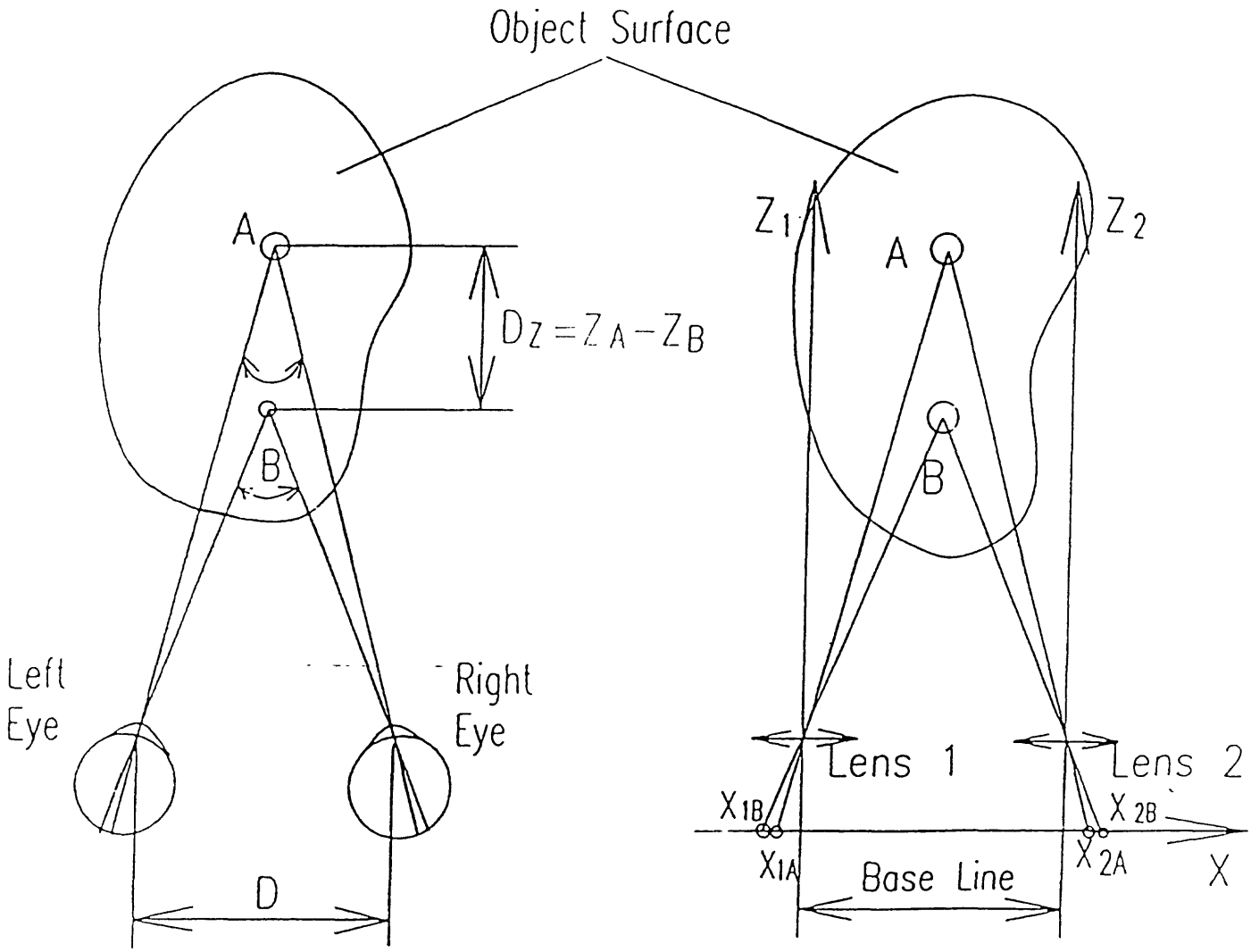

Figure 14. The human eye model of stereo vision. Comparison of human vision system (on left) and a camera system (on right).

1981, 1985), and hybrid (Lillestrand, 1972). Area-based algorithms use image gray-level distribution information directly to find the best match between a pair of images. Various correlation techniques are used to define area-based algorithms. Feature-based algorithms compare specific characteristics extracted from a pair of images, such as edges, lines, vertices, and other regular shapes. Through this process, a best match between two images can be obtained. In general, the correlation algorithms provide good matches because of their inherent noise-suppression effects if distortion is not excessive. This approach may not be the best alternative when attempting to detect the peak of a broad correlation function. Thus, feature-based algorithms strongly depend on good, noise-free images for exact feature extraction. In general, feature-based techniques yield a best match more reliably and accurately than area-based techniques. The hybrid algorithms combine both area-based and feature-based algorithms.

Two stereo imaging experimental set-ups for measuring the three-dimensional geometry of objects are described in this part of the report: A parallel optical-axis model and a converging optical-axis model. Digital image correlation is used to find the disparities between corresponding points in a pair of images for each of these models with subpixel accuracy. The application of the developed algorithms and the stereo-imaging experimental set-ups are shown using four different object surfaces.

Principles of Stereo Imaging

The selection of the coordinate system that governs the experimental set-up depends on the particular experimental set-up. Figure 15 shows the general scheme of the experimental set-up used in this investigation. The three-dimensional world coordinate system, as represented by coordinates (X, Y, Z), is centered at point O. The X-axis of the world coordinate system coincides with the line segment A_1A_2 and the Z-axis with the perpendicular bisector of the line segment A_1A_2. Point O lies on the line connecting points A_1 and A_2, being equidistant from both.

The individual two-dimensional camera-image plane coordinate systems are centered at points O_1, which defines local coordinate axes (x_1, y_1), and O_2, which defines local coordinate axes (x_2, y_2). Points A_1 and A_2 are at the center of rotation for each of the cameras. Considering that the swing angle (for rotation about the Z-axis) and the tilt angle (for rotation about the X-axis) are negligible, points O, A_1, A_2, O_1 and O_2 lie in the same plane, that is, in the XOZ plane. The optical axes of both cameras are normal to the camera-image planes, and it is along the respective optical axes that the z_1 and z_2 axes of the local camera coordinate systems are defined. Also, as shown in figure 15, each of the optical axes is assumed to be rotated about its respective y-axis. Thus, the z_1-axis is rotated clockwise by an angle β_1 about the y_1-axis and the z_2-axis counterclockwise by an angle β_2 about the y_2-axis.

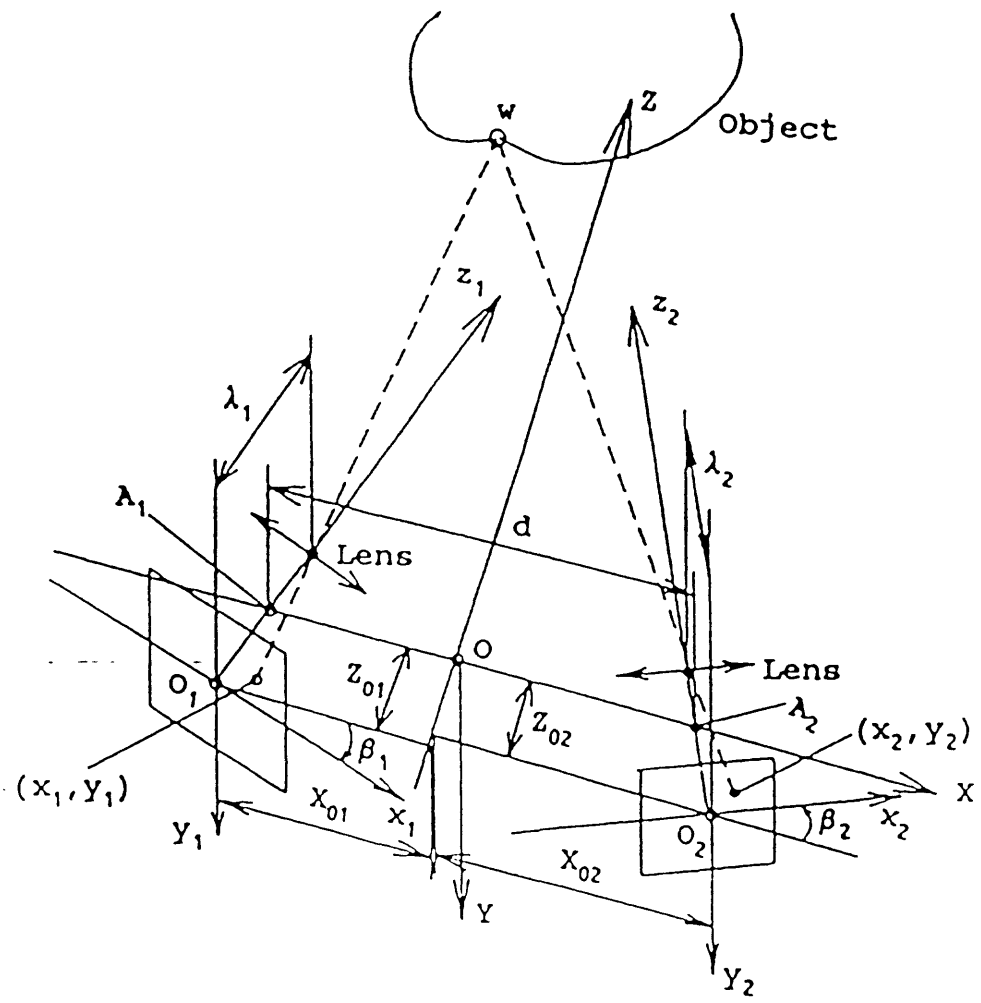

Figure 15. The coordinate system used for binocular vision.

Based on figure 15, the relation between the world coordinate system and the local or camera coordinate system can be established, using matrix notation, as:

$$\underline{x}^T = [R]\ [T]\ \underline{X}^T \tag{15}$$

where the superscript T denotes the transpose of the vectors $\underline{x}$ and $\underline{X}$, respectively. The homogeneous coordinate column matrices for the local and global coordinate systems, respectively, are

$$\underline{x} = [x^*, y^*, z^*, 1]^T, \quad \underline{X} = [X, Y, Z, 1]^T \tag{16}$$

and [R] and [T] are the rotation and translation matrices, respectively, which are defined as follows:

$$[R] = \begin{bmatrix} \cos\beta & 0 & -\sin\beta & 0 \\ 0 & 1 & 0 & 0 \\ \sin\beta & 0 & \cos\beta & 0 \\ 0 & 0 & 0 & 1 \end{bmatrix} \tag{17}$$

and

$$[T] = \begin{bmatrix} 1 & 0 & 0 & X_0 \\ 0 & 1 & 0 & Y_0 \\ 0 & 0 & 1 & Z_0 \\ 0 & 0 & 0 & 1 \end{bmatrix}. \tag{18}$$

Thus, using these equations, it is possible to transform the world coordinate system into the local or camera coordinate system. Additionally, the perspective relation between world and local

coordinates is expressed as,

$$\frac{x^*}{X} = -\frac{z^* - \lambda}{\lambda}$$
$$\frac{y^*}{Y} = -\frac{z^* - \lambda}{\lambda} \qquad (19)$$

where λ is the distance from the camera lens to the image plane.

Substituting the parameters found from equation 16 into equation 20 (taking into account two camera systems) yields four equations. Solving these four equations for X, Y and Z allows the three-dimensional shape of the surface of an object to be determined using the following expressions:

$$X = \frac{x_1\lambda_1 - m_1X_{01} - n_1(Z+Z_{01})}{m_1} \qquad (20)$$

$$Y = y_1 - Y_{01} - \frac{y_1}{\lambda_1}[(X+X_{01})\sin\beta_1 + (Z+Z_{01})\cos\beta_1] \qquad (21)$$

$$Z = \frac{m_1m_2(X_{01}-X_{02}) + m_1\lambda_2x_2 - m_2\lambda_1x_1 + m_2n_1Z_{01} - m_1n_2Z_{02}}{m_1n_2 - m_2n_1} \qquad (22)$$

where λ_1 and λ_2 are the distances from the camera lens to the image planes for cameras 1 and 2, respectively; (x_1,y_1) and (x_2,y_2) are

points in local image planes 1 and 2, respectively; and (X_{01},Y_{01},Z_{01}) and (X_{02},Y_{02},Z_{02}) are the translation components along the X, Y, and Z directions from point O to points O_1 and O_2, respectively; and m_1, m_2, n_1, n_2 are given by the expressions,

$$m_1 = \lambda_1 \cos\beta_1 + x_1 \sin\beta_1 \tag{23}$$

$$m_2 = \lambda_2 \cos\beta_2 - x_2 \sin\beta_2 \tag{24}$$

$$n_1 = x_1 \cos\beta_1 - \lambda_1 \sin\beta_1 \tag{25}$$

$$n_2 = x_2 \cos\beta_2 + \lambda_2 \sin\beta_2. \tag{26}$$

Note that if reference is made to the experimental set-up in figure 16, $Y_{01} = Y_{02} = 0$.

The following conditions are established: If $\beta_1 = \beta_2 = 0$ and $\lambda_1 = \lambda_2 = \lambda$, then $m_1 = m_2 = \lambda$, $n_1 = x_1$ and $n_2 = x_2$; also, if the X- axis of the world system coincides with the line segment O_1O_2 (that is, $Z_{01} = Z_{02} = 0$), and let $X_{01} = -X_{02} = B/2$, then the parallel optical-axis model of stereo imaging is obtained, as shown by the following equations:

$$X = \frac{\lambda - Z}{\lambda} x_1 - \frac{B}{2} \tag{27}$$

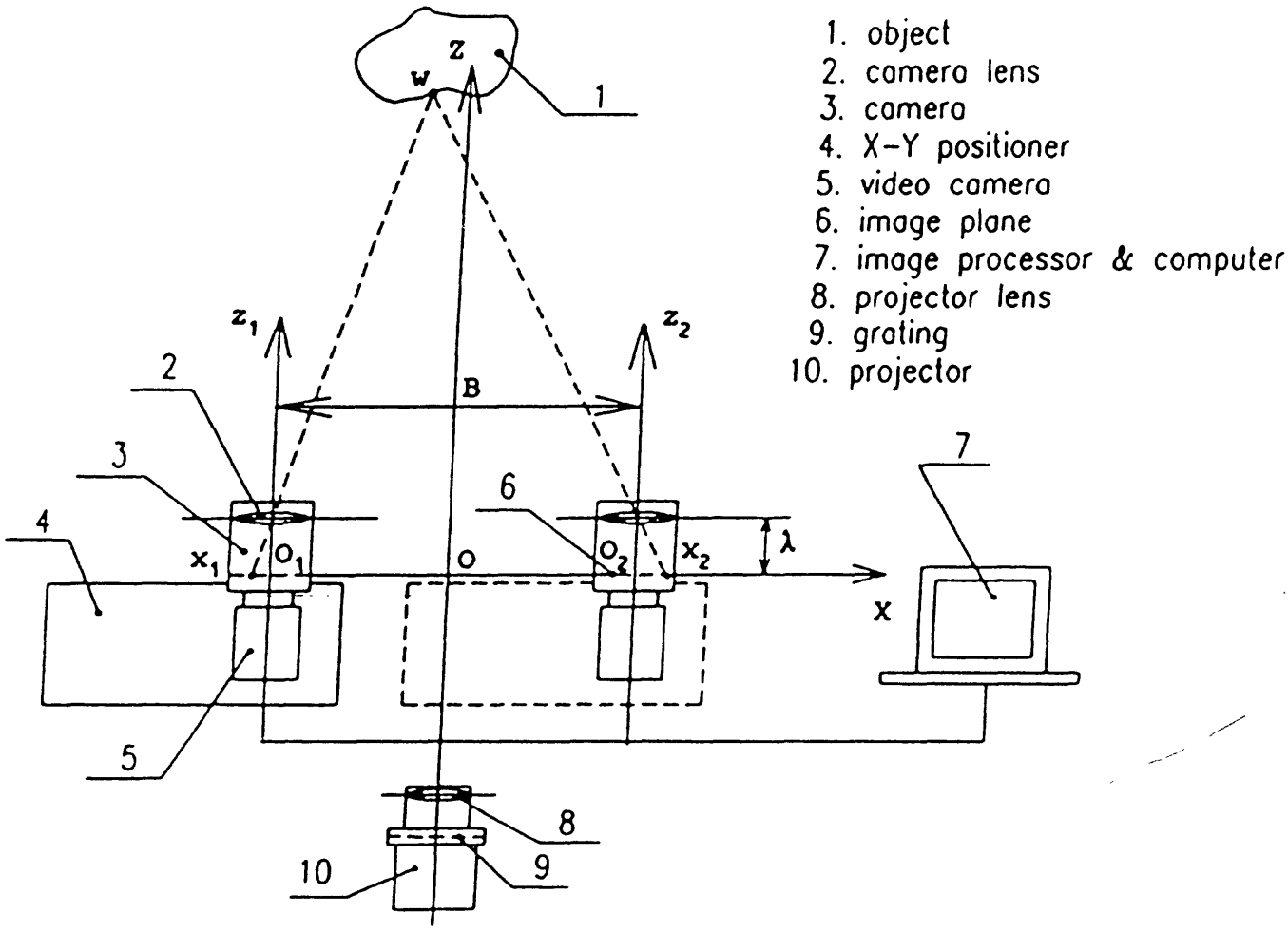

Figure 16. Schematic diagram of the parallel optical-axis experimental set-up.

$$Y = \frac{\lambda - Z}{\lambda} y_1 \tag{28}$$

$$Z = \lambda - \frac{B\lambda}{x_1 - x_2} \tag{29}$$

where B is the baseline, that is, the distance between the two optical axes located at camera positions 1 and 2.

Experimental Set-Up for a Parallel Optical-Axis Model

A schematic of the parallel optical-axis experimental set-up for stereo vision is shown in figure 16. A charge-coupled device (CCD) video camera that has 752 horizontal and 480 vertical picture elements is used with this system. Attached to the video camera is a lens with a nominal focal length of 105 mm. To obtain video capture of the images, a 1-megabyte image memory digitizing image processing board is attached to the video camera and mounted inside a 386/25 microcomputer. This set-up uses only one video camera. The camera is mounted on one of the translation stages of a computer-driven X-Y linear motion positioning table. This linear motion positioner is capable of 300 mm maximum travel, with an accuracy of ± 0.0001 mm. In addition, a projector is used to project a grating on the object of interest when the surface of the object to be measured is so diffuse that it does not provide a wide range of gray levels. It is difficult to find corresponding points

by digital correlation techniques when a wide range of gray levels are not present. Projecting a grating onto such a surface provides a way to structure the surface with a convenient gray-level distribution at every point, making it more convenient to find the corresponding points. Additional attachments to this set-up include a video color monitor and video image printer.

The video camera is mounted and fixed on a spacer block that mounts on the translation stage of the X-Y positioner. The spacer block is machined carefully to guarantee that the top and bottom of this block are parallel to each other and to ensure that the camera tilt is negligible. The X-Y positioner is fixed on an anti-vibration optical table (1.22-m by 3.66-m) with a perfect planar surface (±0.13 mm over the entire surface). The object to be measured also rests on the table surface and is never moved during testing. Thus, by moving the X-Y positioner mounted camera, it is possible to obtain two or more video images of the object, with full control over the baseline length ensuring that the optical axes of the camera at the various positions are perfectly parallel.

Experimental Set-Up for a Converging Optical-Axis Model

A schematic of the converging optical-axis experimental set-up for stereo imaging is shown in figure 17. It uses the same components as the previously described parallel optical-axis experimental set-up, except that the X-Y positioner is not used.

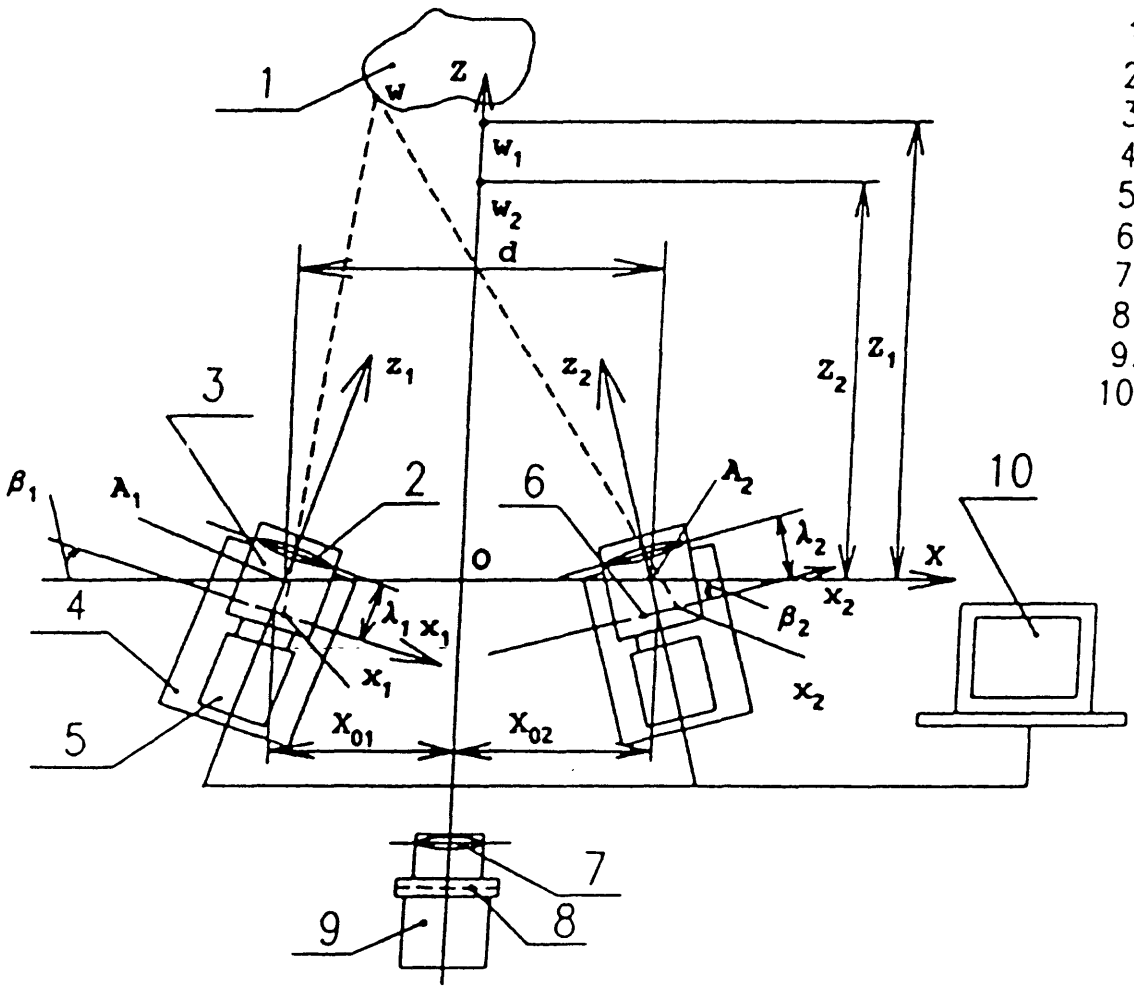

1. object
2. camera lens
3. camera
4. baseblock
5. video camera
6. image plane
7. projector lens
8. grating
9. projector
10. image processor

Figure 17. Schematic diagram of the converging optical-axis experimental set-up.

Instead, the single camera is moved from one position to another by taking advantage of the threaded holes in the optical table, which are precisely machined and whose center-to-center distance is 25.4 mm ±0.38 mm. Thus the camera(s) can be moved a known fixed distance apart. Spacer blocks are used to attach the camera to the surface of the optical table. A hole drilled through the block serves as a rotating center, which also is the rotating center of the camera. Video images are then taken using camera 1 (on the left side of fig. 17) with pan angle β_1 clockwise, and camera 2 (on the right side of fig. 17) with pan angle β_2 counterclockwise. To reduce experimental errors, it is necessary to perform a calibration to determine the values of the angles β_1 and β_2.

Calibration

Calibration to take into account the swing, tilt, and pan angle errors in the parallel optical-axis experimental set-up was not necessary because of the high accuracy of all mechanical components. For the converging optical-axis experimental set-up, the swing and tilt angle errors also were neglected for calibration purposes. Any resulting errors as a result of inaccuracies in accounting for the correct values of swing, tilt, and pan angle as applicable in either of these experimental set-ups can be included in the final experimental results but are not covered in this report.

The required calibration is related to determining pan angles, β_1 and β_2 and the transform components, X_{01}, X_{02}, Z_{01}, and Z_{02}. The geometry used to perform this calibration is shown in figure 18. Points w_1 and w_2 are specific points on the object whose (X_1,Y_1,Z_1) and (X_2,Y_2,Z_2) coordinates are known. In the case of this calibration, $X_1 = X_2 = Y_1 = Y_2 = 0$, and the Z_1 and Z_2 values measured from the X-axis are known. The translation components from the world system to the local or camera systems are:

$$\begin{aligned} Z_{01} &= (X_{01}-\frac{d}{2})\ \cot\beta_1 \\ Z_{02} &= (X_{02}-\frac{d}{2})\ \cot\beta_2 \\ Y_{01} &= Y_{02} = 0 \end{aligned} \tag{30}$$

where d is the distance between the two camera rotating centers. From equation 30, equations 16 through 20, and taking into account the two camera systems, the following four equations are obtained

$$\begin{aligned} &(\lambda_1\cos\beta_1 + x_{11}\sin\beta_1)\ X_{01} \\ &+ (x_{11}\cos\beta_1 - \lambda_1\sin\beta_1)\ [Z_1+(X_{01}-\frac{d}{2})\ \cot\beta_1] - x_{11}\lambda_1 = 0 \end{aligned} \tag{31}$$

$$\begin{aligned} &(\lambda_1\cos\beta_1 + x_{12}\sin\beta_1)\ X_{01} \\ &+ (x_{12}\cos\beta_1 - \lambda_1\sin\beta_1)\ [Z_2 + (X_{01}-\frac{d}{2})\ \cot\beta_1] - x_{12}\lambda_1 = 0 \end{aligned} \tag{32}$$

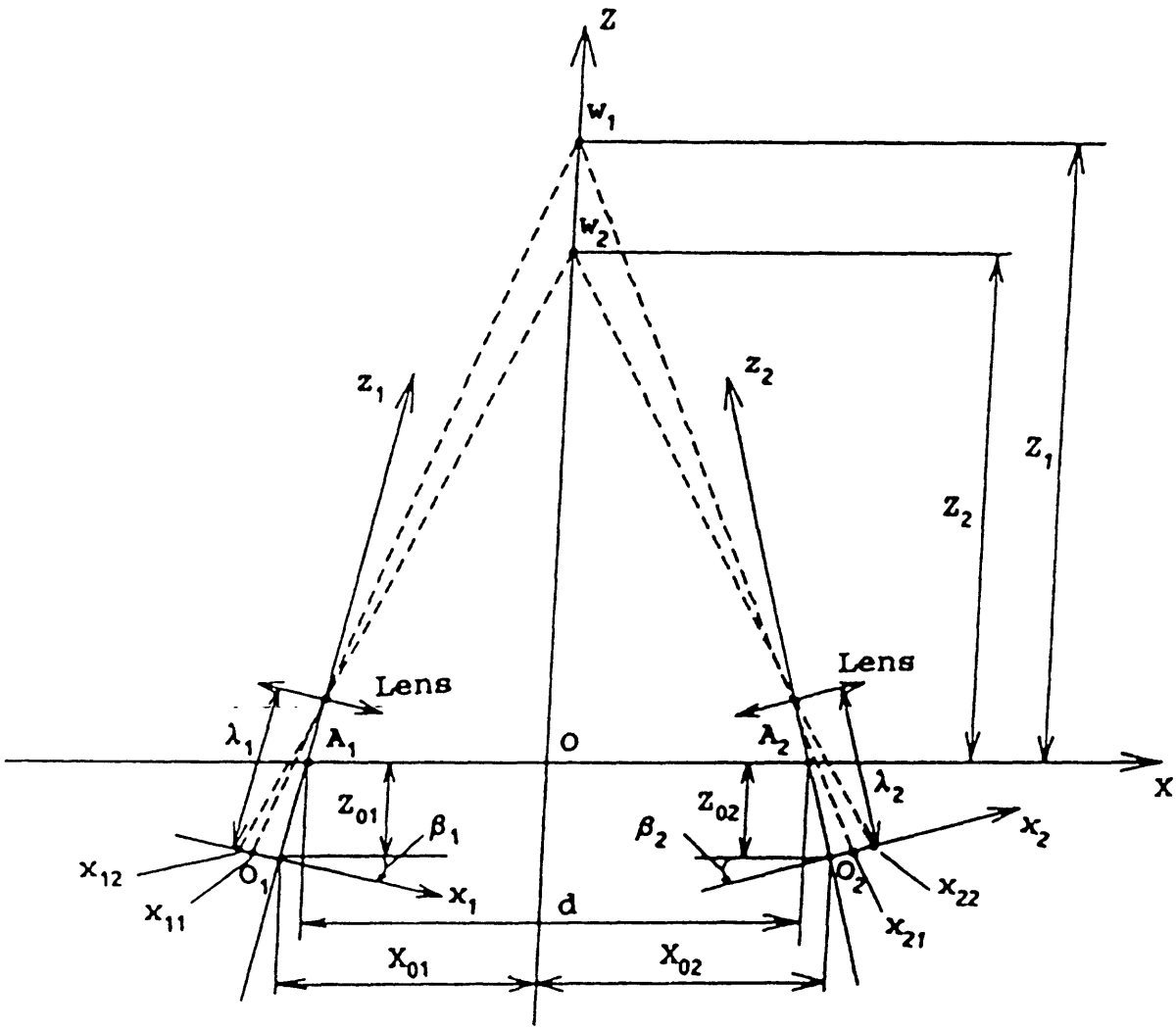

Figure 18. Calibration geometry for the more general converging optical-axis experimental set-up.

$$- (\lambda_2 \cos\beta_2 - x_{21}\sin\beta_2)\, X_{02}$$
$$+ (x_{21}\cos\beta_2 + \lambda_2\sin\beta_2)\, [Z_1 + (X_{02} - \frac{d}{2})\, \cot\beta_2] - x_{21}\lambda_2 - 0 \quad (33)$$

$$- (\lambda_2 \cos\beta_2 - x_{22}\sin\beta_2)\, X_{02}$$
$$+ (x_{22}\cos\beta_2 + \lambda_2\sin\beta_2)\, [Z_2 + (X_{02} - \frac{d}{2})\, \cot\beta_2] - x_{22}\lambda_2 - 0 \quad (34)$$

where λ_1, λ_2, β_1, β_2, X_{01} and X_{02} have been previously defined; Z_1 and Z_2 are the coordinate values of the calibration points w_1 and w_2; x_{11} and x_{12} are the projections of the points w_1 and w_2 on the image plane at camera position 1; x_{21} and x_{22} are the projections of the points w_1 and w_2 on the image plane at camera position 2; and d is the distance between the two camera's rotating centers.

By solving equations 32 through 35 for β_1, β_2, X_{01}, and X_{02} and substituting X_{01} and X_{02} into equation 31, all parameters needed for the accurate determination of the surface topography of objects are obtained, and the calibration of the experimental set-up is achieved.

Determination of Corresponding Points

The implementation of stereo imaging requires the determination of corresponding points between a pair of images.

One approach to this problem is to use an area-based algorithm. There are other correlation techniques that have been developed by other researchers, but for convenience and to shorten computer runtime, an area-based algorithm approach is used in this study, which is defined as follows.

Define x_0 and y_0 as the disparity or translation difference existing between two corresponding points in a pair of images. Let $g(x,y)$ represent a gray-level distribution sampled from the first image, where the center of this gray-level sample is located at the point (x,y). Then $g^*(x+x_0,y+y_0)$ represents a gray-level distribution sampled from the second image, with its center located at point $(x+x_0,y+y_0)$. The similarity between $g(x,y)$ and $g^*(x+x_0,y+y_0)$ can be defined in discrete form by

$$S = R[\, g(x,y),\ g^*(x+x_0,y+y_0)\,] \qquad (35)$$

where $g(x,y)$ and $g^*(x+x_0,y+y_0)$ are gray-level distributions expressed in terms of an (n x m) matrix, and R represents a relationship operation that defines a correlation measure between $g(x,y)$ and $g^*(x+x_0,y+y_0)$.

If the Euclidian distance is used to measure the similarity between $g(x,y)$ and $g^*(x+x_0,y+y_0)$, the discrete correlation function $C(x_0,y_0)$ is written as

$$C(x_0, y_0) = \sum_{i}^{n} \sum_{j}^{m} \| g_{ij}(x,y) - g_{ij}(x+x_0, y+y_0) \| \qquad (36)$$

If normalized correlation is used to measure the similarity between two images, the discrete correlation function is defined as follows:

$$C(x_0, y_0) = \frac{\sum_{i}^{n} \sum_{j}^{m} g_{ij}(x,y) \cdot g_{ij}(x+x_0, y+y_0)}{\left[\sum_{i}^{n} \sum_{j}^{m} g_{ij}^2(x,y) \cdot \sum_{i}^{n} \sum_{j}^{m} g_{ij}^2(x+x_0, y+y_0)\right]^{\frac{1}{2}}} \qquad (37)$$

The (n x m) area considered, in using either of these discrete correlation functions, is a gray-level subset extracted from the two images. The point $(x+x_0,y+y_0)$ in the second image that corresponds to the point (x,y) in the first image is found by looking for a minimum value of the above correlation function. Thus, the peak of the similarity between the two areas is found using this approach. The result is that the disparity between the first and second image is (x_0,y_0). This value is used to calculate the needed Z coordinate. This approach achieves subpixel accuracy when determining the surface topography of the objects considered.

Experimental Results of Surface Topography Measurements

To illustrate the validity of the above theoretical procedure, four different kinds of object surfaces were tested: A piece of

paper with an inscribed hollow letter A taped to a tilted plane; a semi-cylindrical surface; a semi-spherical surface; and a semi-sinusoidal or wavy surface. The correlation function used for mapping the inscribed letter A, the semi-cylindrical, and the wavy surface is given by equation 38. The correlation function used to map the semi-spherical surface is given by equation 38. Some preprocessing (averaging the video images several times) of the video images was required to reduce background noise and was found to increase the accuracy of measurement.

Letter A Inscribed On a Tilted Plane

A hollow letter A is inscribed on a sheet of paper and is then glued to an aluminum plate. The aluminum plate is positioned at an angle to the vertical. The baseline B between the two cameras is 60 mm, and the focal length, λ, of the camera lens is 110.74 mm. This experiment was carried out using a parallel optical-axis experimental set-up. In this test, the magnification factors, found by using a known standard to relate the actual length to the measured length in pixels, are 4.91 pixels/mm along the x-axis and 4.24 pixels/mm along the y-axis. The analysis is performed from two video images of the hollow letter A, consisting of 11 thick-line segments. The algorithm used to determine the location of the letter A thick-line segments used their centerline location to reconstruct them. In determining the centers of the thick-lines, a scanning window program was used to interrogate and correlate the

two video images.

Figure 19 shows the results of the point-by-point reconstruction of the three-dimensional shape of the hollow letter A with an accuracy of approximately ±0.07 pixels. Table 4 gives the statistical results and measurement errors. To obtain the vertical distance from the lowest to the highest point of the letter A, the average vertical location of 46 points at the lower end (z_1 = 1956.60 mm) and the average of 43 points at the upper end (z_2 = 1995.79 mm) are used. This results in a vertical distance difference of Δz_m = 39.19 mm. Additionally, the tilt angle of the letter A from the horizontal is calculated using this vertical distance and the actual length of the letter A, D, which is 80 mm.

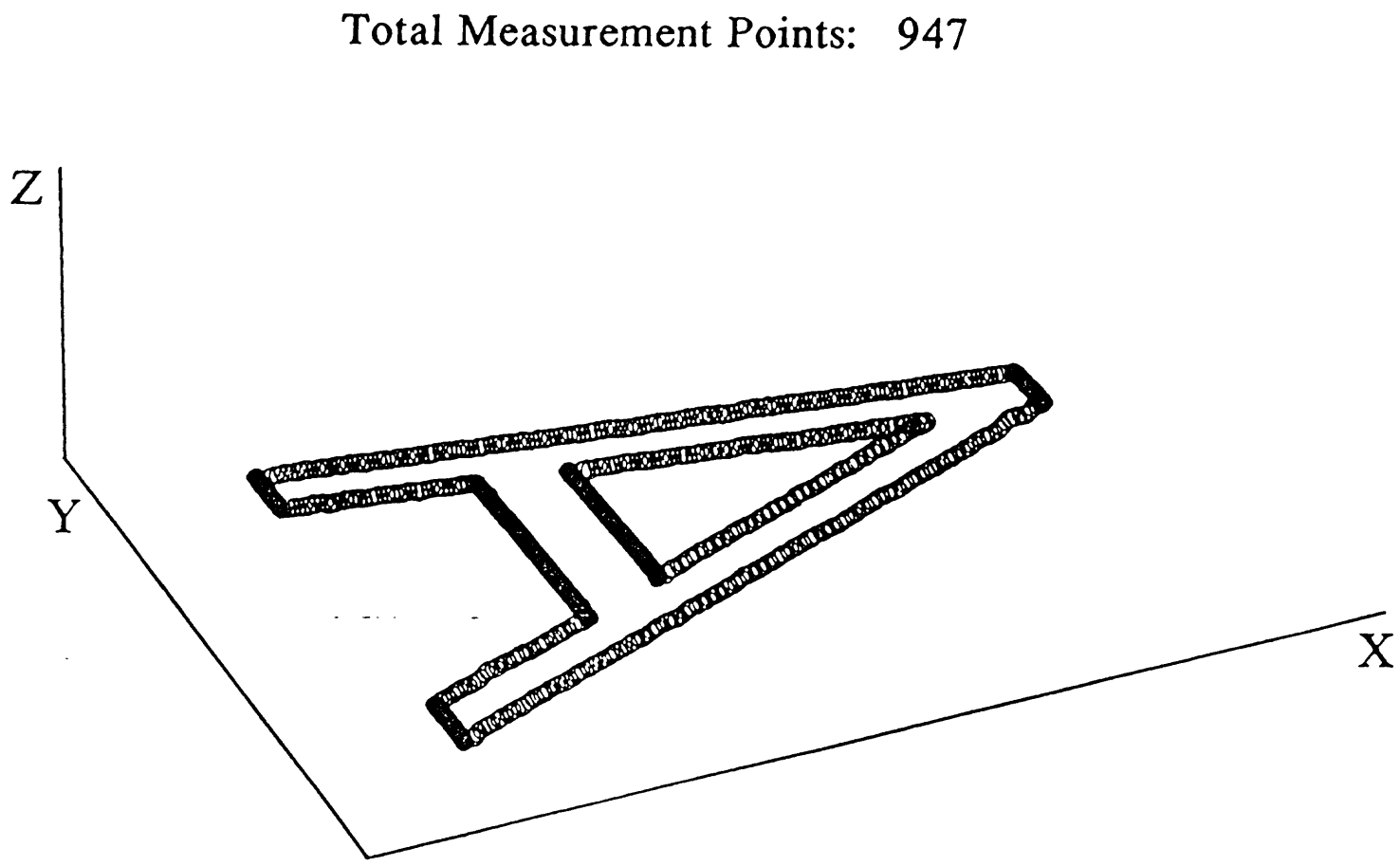

Figure 19. Three-dimensional reconstruction of the hollow letter A on a tilted plane.

Table 4. Error analysis of hollow A

	Vertical distance from lowest to highest point, Δz (mm)	Tilt angle (degrees)
Actual	40.12	30.10
Measured	39.19	29.33
Mean absolute error	-0.934	-0.11
Mean relative error (percent)	-2.33	-2.56

Semi-Cylindrical Surface

A semi-cylindrical surface inserted in a flat plane was measured using the parallel and converging optical-axis experimental set-ups. For the parallel optical-axis experimental set-up, the baseline B between the two cameras is 30 mm, and the focal length, λ, of the camera lens is 112.02 mm. The following values were used for the converging optical-axis experimental set-up: $\beta_1 = -\beta_2 = 0.11$ radians; $Z_{01} = Z_{02} = 0$, $X_{01} = X_{02} = 127$ mm; and $\lambda_1 = \lambda_2 = 112.83$ mm. A reconstructed image of the point-by-point surface topography of the semi-cylindrical surface obtained with the converging optical-axis experimental set-up is shown in figure 20. The data has an accuracy of ±0.06 pixels.

TOTAL MEASUREMENT POINTS: 1,560

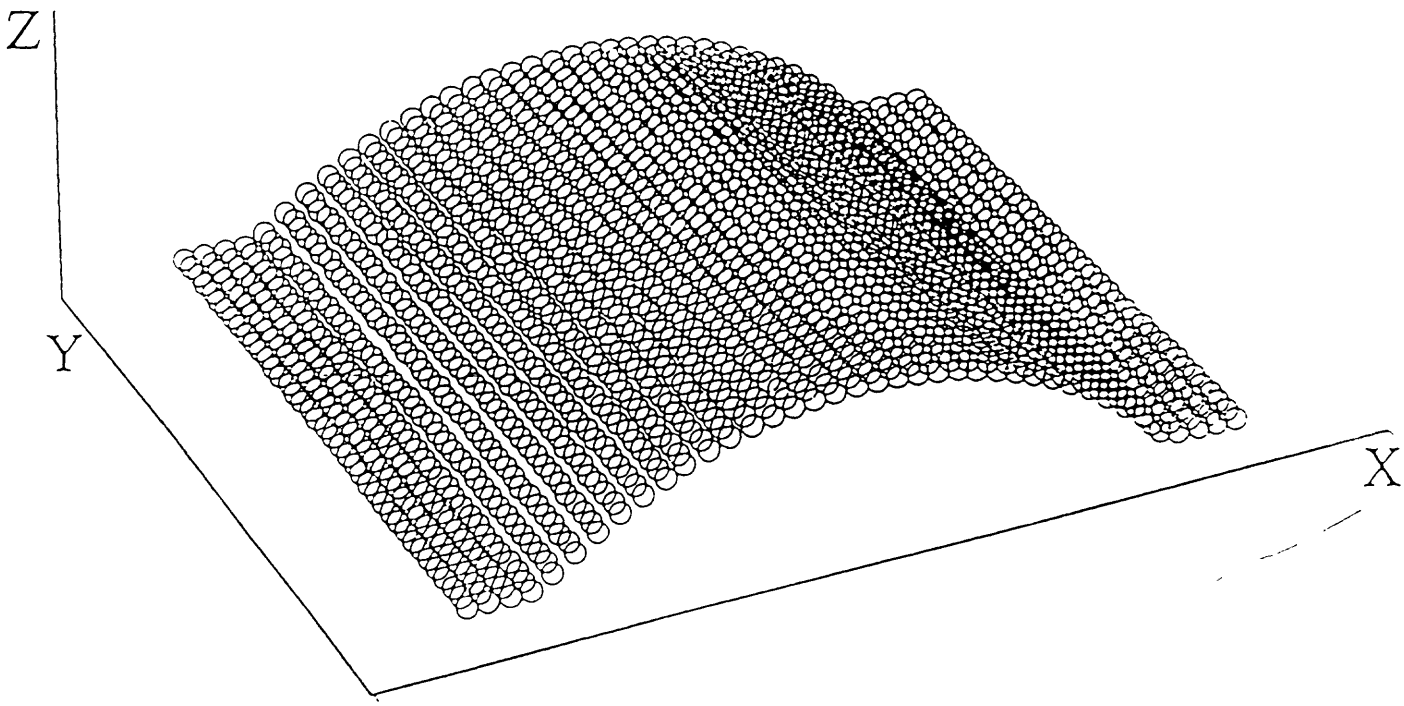

Figure 20. Three-dimensional reconstruction of a semi-cylindrical surface.

To determine which of the two experimental set-ups is more accurate, an error analysis was done using the results obtained from the two models. The radius of the cylinder is assumed to be the comparative base for this error evaluation. The actual radius of the cylinder, r_t, is measured with calipers and is 32.25 ± 0.025 mm.

Figure 21 shows the geometry used to compute the measured radius of curvature at every point that defines the surface of the object. In this figure, h_t and r_t are the actual height and radius of the semi-cylindrical surface. The measured height is h_m at each experimental point. From the geometric relations shown in figure 22, the measured radius is

$$r_m = [\, x^2 + (r_t - h_t + h_m)^2 \,]^{\frac{1}{2}} \qquad (38)$$

which is a function of the x coordinate of the experimental point.

The average or mean value of these data is $(r_m)_m$, e_a is the absolute error, e_s is the statistical mean error, and S is the standard deviation for all observations. A comparison of the measured errors for the parallel and converging optical-axis experimental set-ups is given in table 5. This table shows that the converging optical-axis experimental set-up has a higher measuring accuracy than the parallel-axis experimental set-up.

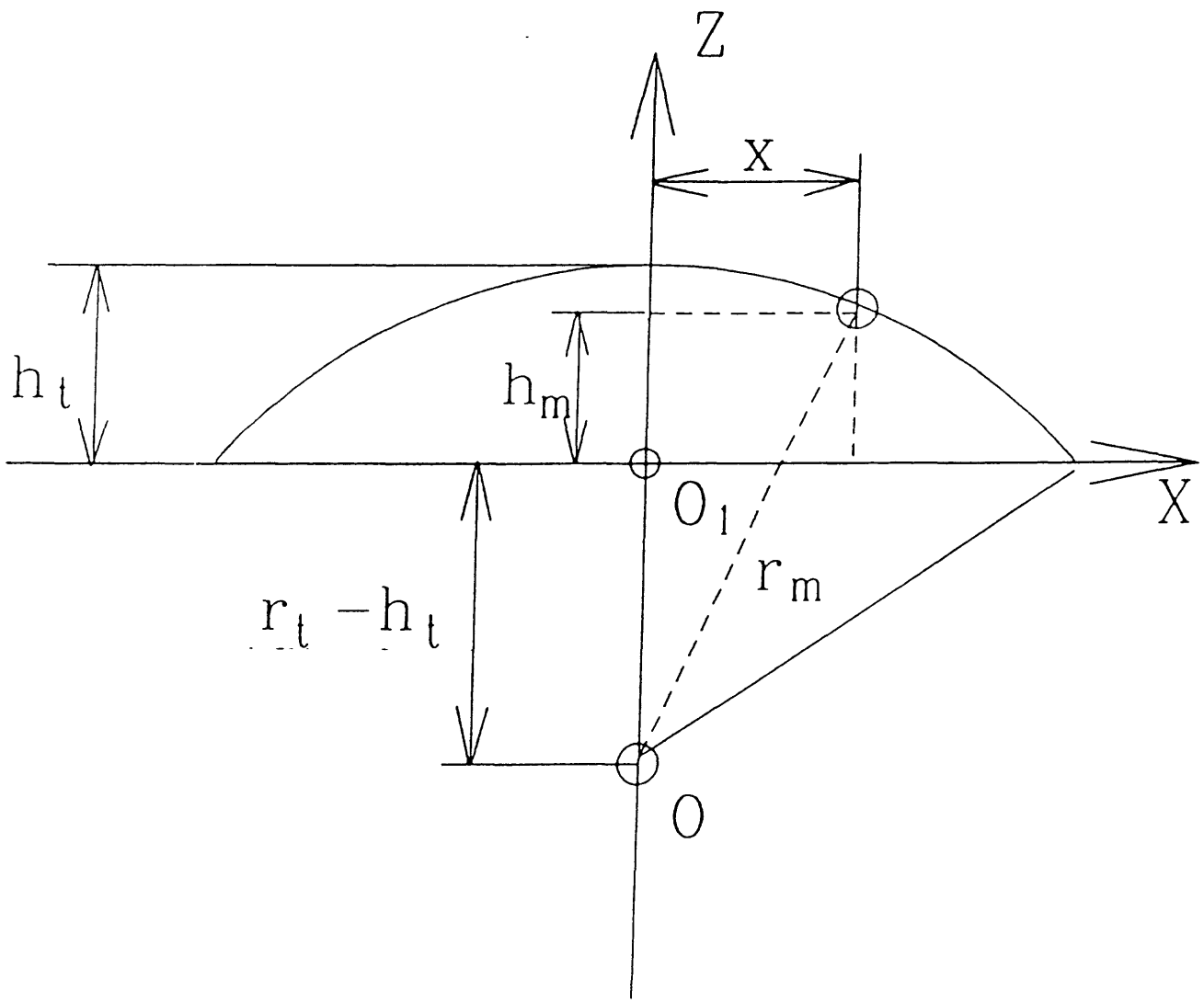

Figure 21. Geometry for computing radius r_m.

TOTAL MEASUREMENT POINTS: 4,698

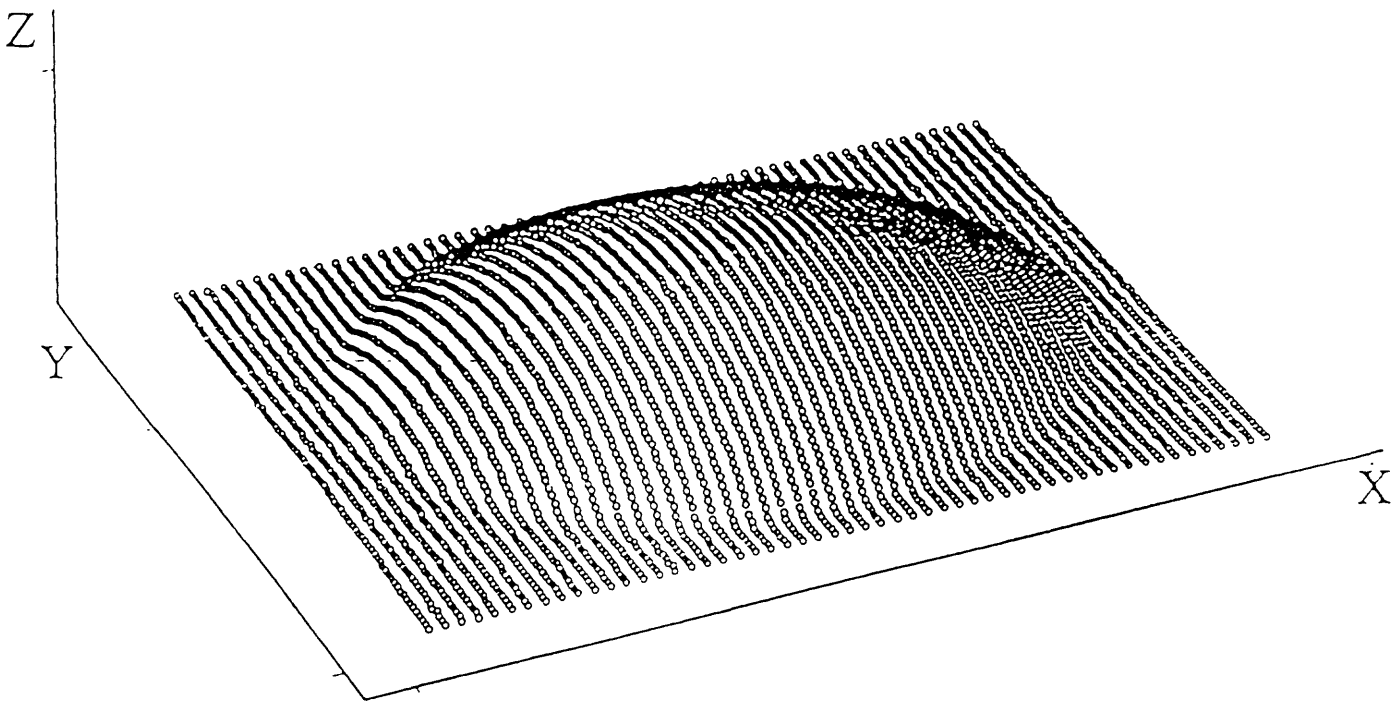

Figure 22. Three-dimensional reconstruction of a semi-spherical surface.

Table 5. Error analysis of a semi-cylindrical surface [mm, millimeters; parameters for the experimental setup: $(r_m)_m$, mean value of the measured radius; e_a, absolute error: e_s, statistical mean error; S, standard deviation for all observations; and $(r_m)_m - r_t$, mean measured radius minus measured cylinder radius]

Optical-axis model	$(r_m)_m$ (mm)	e_a (mm) $(e_a)_{max}$	e_a (mm) $(e_a)_{min}$	e_s percent	S (mm)	$(r_m)_m - r_t$ (mm)
Parallel	31.875	0.742	0.001	1.41	0.253	-0.375
Converging	32.268	0.361	0.016	0.81	0.257	0.018

Semi-Spherical Surface

The converging optical-axis experimental set-up was used to determine the shape of a semi-spherical surface inserted in a flat plane. For this experiment, the parameters that define the experimental set-up are: $\beta_1 = -\beta_2 = 0.119$ radians, $Z_{01} = Z_{02} = 0$, $X_{01} = X_{02} = 127$ mm, and $\lambda_1 = \lambda_2 = 112.72$ mm. A point-by-point reconstructed image of the semi-spherical surface and the plane into which it is inserted is shown in figure 22. The accuracy of the calculation is ±0.06 pixels. The magnification factors in this test are 9.478 pixels/mm along the x-axis, and 8.035 pixels/mm along the y-axis.

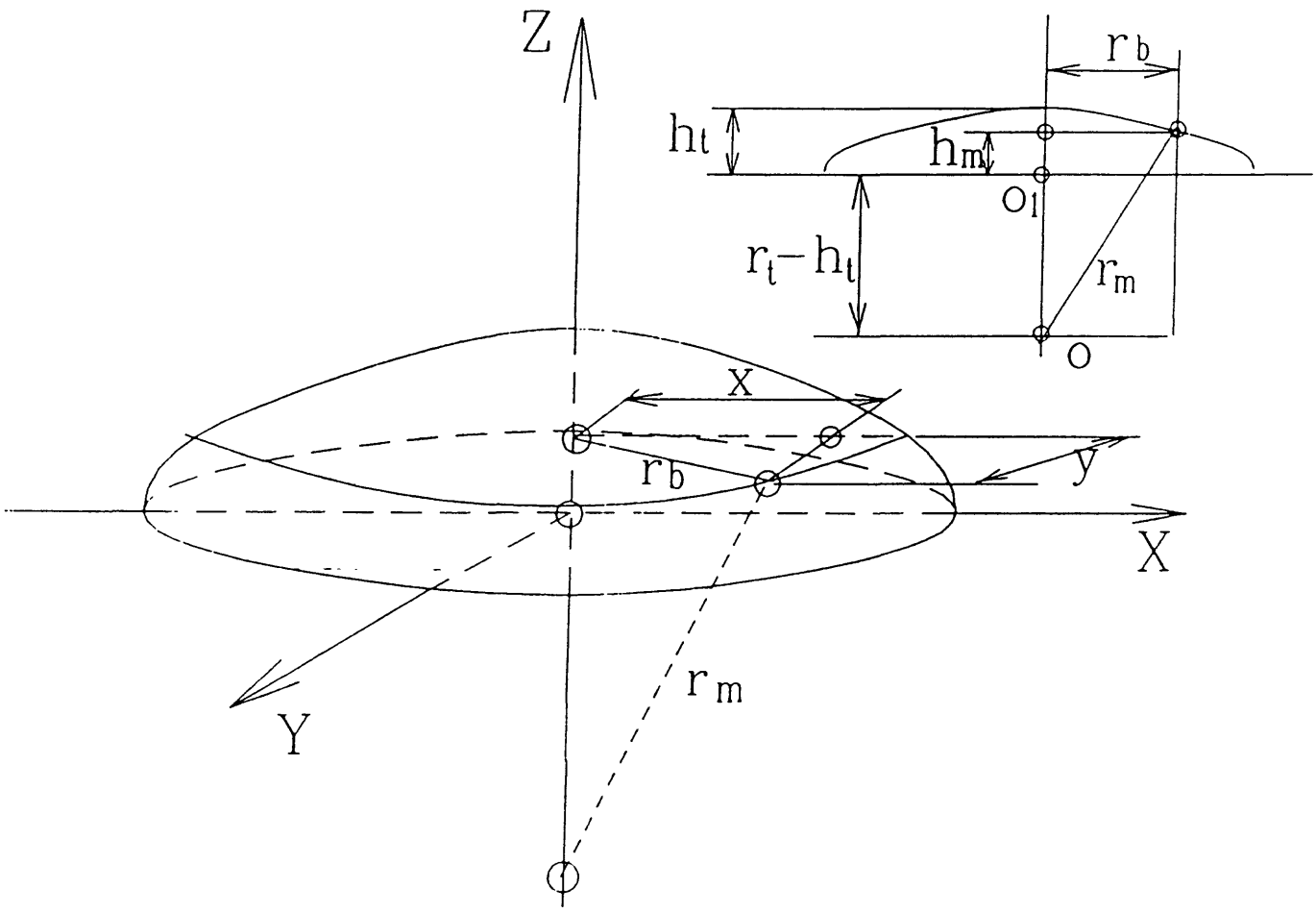

Figure 23. Geometry for computing measurement errors in a semi-spherical surface.

The actual radius of the sphere is used as the basis of comparison to determine the measurement errors in this semi-cylindrical surface. A schematic of the geometry used for estimating these measurement errors is shown in figure 23. Calipers (with an accuracy of ± 0.025 mm) are used to measure the diameter, D_t, of the circular intersection of the semi-sphere with the flat plane, and the height, h_t, of the semi-spherical surface. The radius, r_t, of the semi-spherical surface is then calculated from

$$r_t = \left[\left(\frac{D_t}{2}\right)^2 + \left(\frac{D_t}{2} - h_t\right)^2 \right]^{\frac{1}{2}} \qquad (39)$$

The measured radius, r_m, at every calculated point on the semi-spherical surface is obtained using the following procedure. First, the flat plane vertical location on the object is calculated by averaging the vertical location of 432 points on that plane. The value obtained is 1,230.84 mm. Then the center of the base circle is obtained by locating the horizontal position coordinates x_c and y_c from the first video images. If there is a measured radius needed for a point that has been identified on the semi-spherical surface, the radius of a circle parallel to the base circle, r_b, is obtained from

$$r_b = \left[\left(\frac{x - x_c}{M_x}\right)^2 + \left(\frac{y - y_c}{M_y}\right)^2 \right]^{\frac{1}{2}} \qquad (40)$$

Then, the measured radius, r_m, of every point on the semi-spherical surface is obtained by

$$r_m = [\, r_b^2 + (r_t - h_t + h_m)^2 \,]^{\frac{1}{2}} \qquad (41)$$

where h_m is the measured height from the base plane to any point on the spherical surface.

An error analysis of the calculations of the semi-spherical surface was performed using 2,632 measurement points. The results are given in table 6. Also, figure 24 shows the maximum error cross section of the object. The figure illustrates a comparison between the actual shape and the measured values showing two smooth contours with different curvatures. The maximum error occurs at the highest point of the object. This result reflects the systematic error introduced as a result of the machining process, which was not very accurate, used to form this semi-spherical shape.

Table 6. Error analysis of a semi-shperical surface [mm, millimeters; parameters for the experimental setup are: $\underline{D_t}/2$, actual radius; $(r_m)_m$, mean measured radius; e_s, relative error; and standard deviation]

$\underline{D_t}$					
2	$(r_m)_m$	$\underline{e_s}$ (percent)			S
(mm)	(mm)	Mean	Max	Min	(mm)
53.810	54.986	2.186	-0.004	4.358	0.620

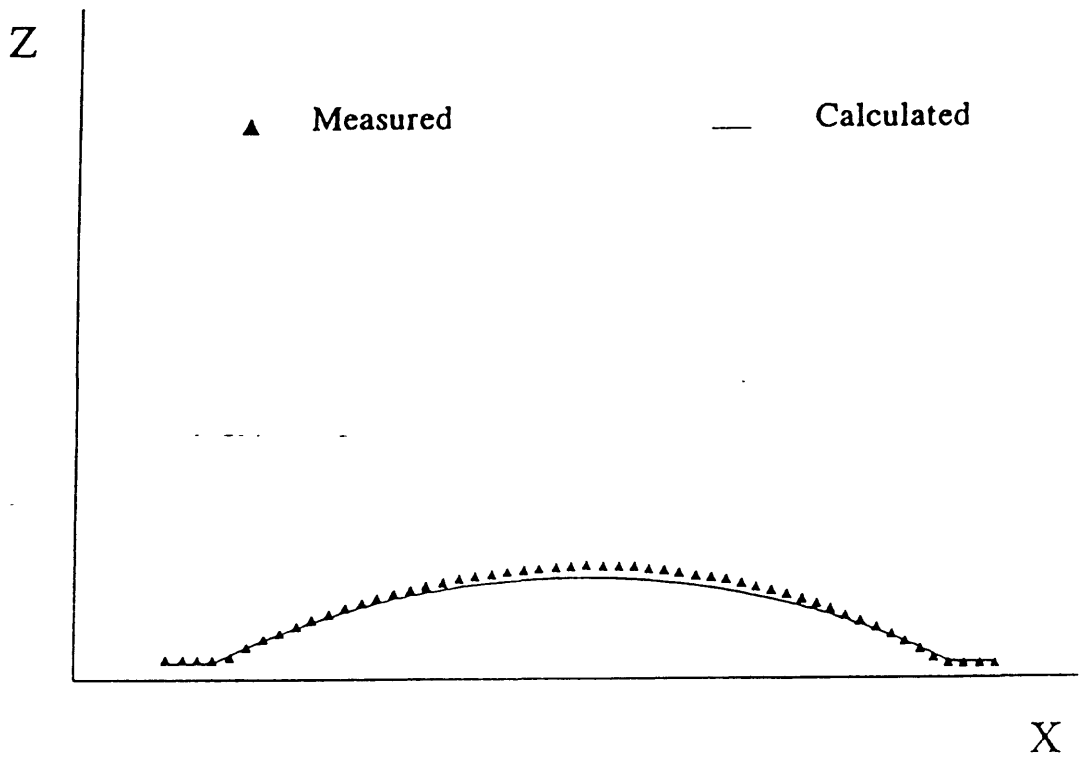

Figure 24. Comparison of the measured and calculated semi-spherical surface.

Wavy Surface

The final surface tested using the stereo imaging equipment was a semi-sinusoidal or wavy surface. It was chosen because of its more complex surface. The baseline of the parallel optical-axis experimental set-up is 30 mm, and the focal length, λ, of the camera lens is 109.61 mm. The number of measurement points on the wavy surface is 6,840 with an accuracy of ±0.06 pixels. The three-dimensional smoothed shape of this reconstructed surface is shown in figure 25. The parallel optical-axis experimental set-up was used because the converging optical-axis experimental set-up was unable to image all areas of this particular specimen. Since no independent measurements of the wavy surface topography were made, an estimate of the accuracy of this wavy surface mapping would have to rely on the previous experimental results.

TOTAL MEASUREMENT POINTS: 6,840

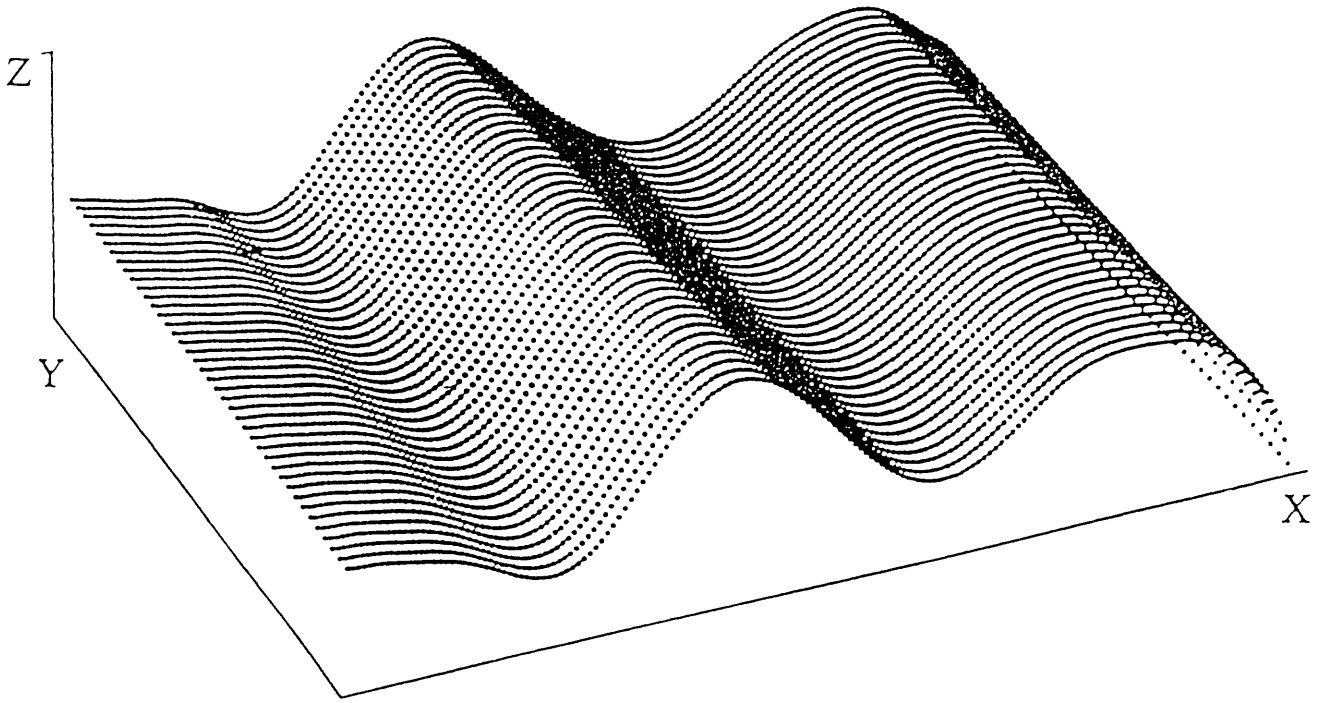

Figure 25. Three-dimensional reconstruction of a wavy surface.

AUTOMATED PHASE-MEASURING PROFILOMETRY FOR THREE-DIMENSIONAL RECONSTRUCTION OF OBJECT SURFACES

Noncontact measurement of three-dimensional objects is a desirable alternative to using calipers, dial gauges, and micrometers. It is especially needed in high-speed on-line inspection, mechanical component quality control, automated manufacturing, computer-aided design, medical diagnostics, and robotic vision. Optical methods play an important role in noncontact surface profile measurement. Several optical three-dimensional surface profilometry methods that have been studied exhaustively include projection moire (Idesawa and others, 1977; Perrin and Thomas, 1979; Cardenas-Garcia and others, 1991), phase shifting technique (Kujawinska and Robinson, 1988; Asundi, 1991; Kujawinska and Wojciak, 1991), and Fourier transform (Takeda and others, 1982; Takeda and Mutoh, 1983).

The moiré approach has been widely used as a tool to measure shapes, displacements, and deformation for many years. When two gratings or one grating with its shadow are superimposed under the light, moire fringes appear on the surface, which are the loci of constant heights conveying three-dimensional information about the surface. However, it is not a simple matter to automate the demodulation of this information. Some problems that need to be solved are locating the center lines of the moire fringes, which is especially difficult for broad fringes where the surface is flat

and almost normal to the optical axis; assigning fringe orders, automatically including those separated by discontinuities; making an automatic distinction between an elevation and a depression on the surface, which needs at least two moire fringe images that are obtained before and after the object is translated along the optical axis; and evaluating false or partially dark fringes.

Moire fringe analysis obtains three-dimensional data only at the fringe centers, and considerable information is lost. The points between fringe centers can be measured to increase the accuracy of the measurement. To accomplish this, the object is translated to several accurate locations to obtain different moire images. Processing of the images is then performed at all of these alternative positions. Although this whole procedure can be automated using a computer, considerable time is needed to perform all the processing. This technique is not useful for high speed, on-line inspection, or any other measurement that requires that the object move when measurements are taken. This requirement of more than one image to accurately analyze the surface topography of an object limits the applicability of this experimental technique.

Phase shifting, when applied to moire techniques, is one approach to using all the pixel information of a moire image to calculate the topography of an object. This implementation requires the translation of one grating on its own plane with respect to another. Images are obtained at preset values of

translation, creating several related moire images. The phase of every pixel of the image then can be determined, if the exact translation distance is known. This phase modulation experimental approach avoids most of the problems of conventional moire techniques. However, the optical set-up is more complicated, and small errors in assessing the translation motion substantially affect the accuracy of the measurement. Also, variations in image intensity and contrast have a detrimental affect on the results. Although the use of this experimental approach permits the determination of the three-dimensional coordinates of all points on the moire image in a short time, this method cannot be used if the object being measured is in motion.

Fourier transform profilometry (FTP) does not rely on moire fringes, so it is free from all the difficulties associated with the moire contouring technique, and it can obtain the three-dimensional coordinate of every pixel on the image. The grating image projected on an object surface is processed by taking the Fourier transform. After selecting the second spectrum, its inverse Fourier transform is computed. A reference plane is also analyzed using the same method. By comparing both results, it is possible to obtain the phase difference that is directly associated with the height difference between the point on the surface and the reference plane. Because FTP relies on only one image to assess object shape, it is useful for measuring the shape of not only a static but also a moving object, which substantially broadens the

choice of a window to select the part of the frequency spectrum to be analyzed when calculating the phase difference, it is sometimes difficult to precisely select the exact required spectrum. For example, if more than the required information is extracted, the measurement accuracy decreases near the object edge; whereas, if too little information is extracted, the resulting object shape is distorted.

Another approach that is useful in the mapping of object shape is stereo imaging (Keshef and Sawchuk, 1983; Grimson, 1984, 1985), discussed in a previous section of this report. No grating is needed in this method. Its basic principle is the same as the human vision system. Two images are needed to implement a stereo-imaging approach. Either the images are taken simultaneously from two cameras separated by some distance or with a single camera that is translated relative to itself while acquiring two images of the same object (or the object moves relative to a stationary camera). The same real point on the two images is located by digital correlation. The distance from the point of interest to the lens plane of the camera is calculated from the stereo parallax of the same point and the parameters of the observation set-up. It is a whole-field measurement technique much like FTP, but it has the advantage of giving more direct, unambiguous, and quantitative depth information. One disadvantage is that the computer processing time needed by stereo imaging is much more than that needed by FTP or by the moire phase shifting technique. Also, if

there are not enough surface features on the object, the correlation technique cannot distinguish the same point on two different images.

Another approach to measuring the three-dimensional profile of objects is that taken by Tang and Hung (1990), which is based on the work outlined by Womack (1984) and Ichioka and Inuiya (1972). This measurement approach is a new, fast technique for automatic three-dimensional shape measurement. The phase-measuring profilometry technique, like FTP, is based on the principle of measuring the phase of the deformed grating pattern, which is projected on the object and conforms to its shape. The deformed grating contains the three-dimensional information of the object surface being measured. By using this measurement technique, it is possible to automatically and accurately obtain the phase map or the height information of the object at every pixel. Since only one object image is needed to assess object shape, the object can be either static or moving. Compared to FTP, the phase-measuring profilometry technique processes the deformed grating image pattern in the real-signal domain rather than the frequency domain. This technique has several advantages. It does not require extraction of an exact spectrum to ensure a high-accuracy measurement; it can process any number of pixel points; and it is much faster than FTP.

Using the approach of Tang and Hung (1990), very high levels of measurement accuracy in shape measurement can be achieved if a

simple low-pass digital filter is correctly designed. Several different object surfaces were successfully measured with high accuracy, including some simple diffuse reflecting cylindrical, spherical, triangular, and sinusoidal surfaces, and more complicated rock and silicon wafer surfaces.

Principles of Phase-measuring Profilometry

The principles of phase-measuring profilometry and the low-pass filtering function, which directly affects the accuracy of the measurement, are explained in this section of the report. Also, measurements of several samples and their accuracy are presented.

The optical geometry for the experimental set-up is shown in figure 26. On the reference plane,the grating pattern, $g_r(x,y)$, is expressed by

$$g_r(x,y) = \sum_{n=0}^{\infty} R_n(x,y) \cos\left[\frac{2\pi nx}{p} + n\,\phi_r(x)\right] \qquad (42)$$

where p is the period of the grating fringes on the image, $\phi_r(x)=(2\pi/p)\,r(x)$ is the phase shift on the reference plane owing to the divergent light source, where $r(x)$ is the distance point (x,y) that moves when p is moved from infinity to a finite distance from point O.

When the grating pattern is projected onto the surface to be

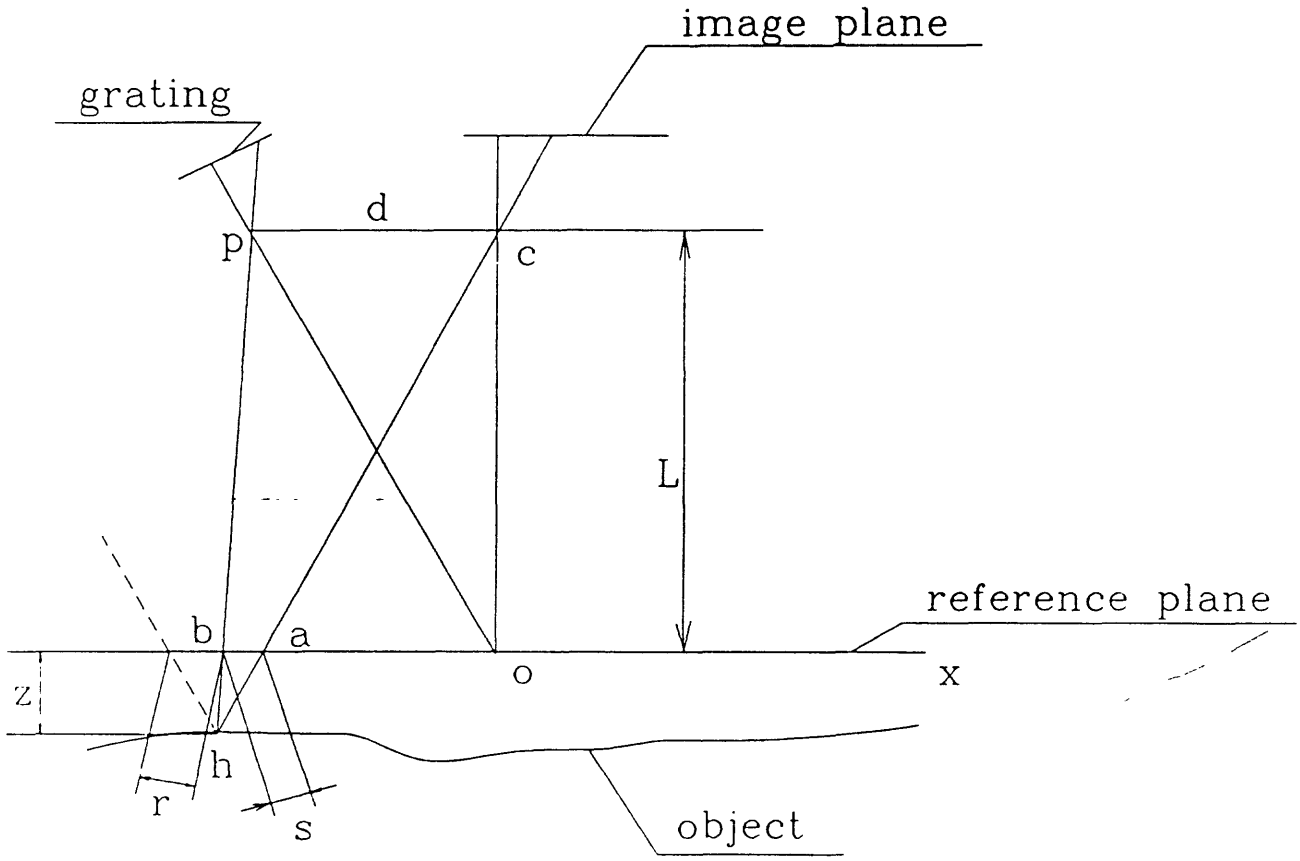

Figure 26. The geometry of the experimental set-up.

measured, the deformed grating pattern is observed at point C. The grating pattern, $g_0(x,y)$, on the object surface can be expressed as

$$g_o(x,y) = \sum_{n=0}^{\infty} B_n(x,y) \cos\left[\frac{2\pi nx}{p} + n\,\phi_o(x,y)\right] \qquad (43)$$

where $\phi_o(x,y) = (2\pi/p)\ [r(x) + s(x,y)]$ is the phase shift on the object surface.

The phase difference, $\Delta\phi(x,y)$, between the reference plane and the object surface is

$$\Delta\phi(x,y) = \phi_o(x,y) - \phi_r(x) = \frac{2\pi}{p}\, s(x,y) \qquad (44)$$

where, $s(x,y)$ for point h on the object surface is the distance between a and b as shown in figure 26. From simple geometry, the distance z from the reference plane to point h is easily determined from $s(x,y)$.

To obtain the phase $\phi_r(x)$ (from eq. 43) and $\phi_o(x,y)$ (from eq. 44), the following procedure is used. The general pattern is expressed as

$$g(x,y) = \sum_{n=0}^{\infty} a_n(x,y) \cos\left[\frac{2\pi nx}{p} + n\,\phi(x,y)\right] \qquad (45)$$

where phase $\phi(x,y)$ varies very slowly compared to the variation of $\cos(2\pi nx/p)$, is multiplied by $\cos(2\pi x/p)$, and expanded to:

$$
\begin{aligned}
& g(x,y)\cos\frac{2\pi x}{p} - \sum_{n=0}^{\infty} a_n(x,y)\ \cos\left[\frac{2\pi nx}{p} + n\,\phi(x,y)\right]\cos\frac{2\pi x}{p} \\
& - a_0(x,y)\ \cos\frac{2\pi x}{p} + \frac{1}{2}\,a_1(x,y)\ \cos\left[\frac{4\pi x}{p} + \phi(x,y)\right] \\
& + \frac{1}{2}\,a_1(x,y)\ \cos(x,y) + \frac{1}{2}\,a_2(x,y)\ \cos\left[\frac{6\pi x}{p} + 2\,\phi(x,y)\right] \\
& + \frac{1}{2}\,a_2(x,y)\ \cos\left[\frac{2\pi x}{p} + 2\phi(x,y)\right] + \ldots .
\end{aligned}
\qquad (46)
$$

does not have a $(2\pi nx/p)$ term, and it is the only low-frequency term. Assume that $g1(x,y)$ is the result after the function $g(x,y)\cos(2\pi x/p)$ is processed by a digital low-pass filter.

When equation 46 is multiplied by $\sin(2\pi x/p)$ and expanded, the following equation is obtained:

$$
\begin{aligned}
& g(x,y)\ \sin\frac{2\pi x}{p} - \sum_{n=0}^{\infty} a_n(x,y)\ \cos\left[\frac{2\pi nx}{p} + n\,\phi(x,y)\right]\sin\frac{2\pi x}{p} \\
& - a_0(x,y)\ \sin\frac{2\pi x}{p} + \frac{1}{2}a_1(x,y)\ \sin\left[\frac{4\pi x}{p} + \phi(x,y)\right] \\
& - \frac{1}{2}a_1(x,y)\ \sin(x,y) + \frac{1}{2}a_2(x,y)\ \sin\left[\frac{6\pi x}{p} + 2\,\phi(x,y)\right] \\
& - \frac{1}{2}a_2(x,y)\ \sin\left[\frac{2\pi x}{p} + 2\,\phi(x,y)\right] + \ldots .
\end{aligned}
\qquad (47)
$$

In equation 48, the only low frequency is $-\frac{1}{2}\,a_1(x,y)\sin\phi(x,y)$. Assume that $g2(x,y)$ is the result after the function $g(x,y)\sin(2\pi x/p)$ is processed by a digital low-pass filter.

The phase can then be obtained from

$$\phi(x,y) = \tan^{-1}\left[\frac{-g_2(x,y)}{g_1(x,y)}\right]. \qquad (48)$$

The only remaining problem is extracting the low-frequency terms from equations 47 and 48. These can be obtained in the real-signal domain by performing the convolution of the unit sample response *h(n)* of a low-pass digital filter with the input signal represented by equation 46.

In a real measurement, the distribution of the intensity on the reference plane (reference line) should be taken and then multiplied by $cos(2\pi x/p)$ and $sin(2\pi x/p)$, separately. Through low-pass filtering, $g1(x,y)$ and $g2(x,y)$ are obtained, and ϕ_r is then calculated using equation 49. The deformed grating pattern on the object is processed line by line. For each line, the same procedure as for the reference line is performed to get $\phi_o(x,y)$. The phase difference between the object point and the reference $\Delta\phi$ is obtained using

$$\Delta\varphi = \varphi_o(x,y) - \varphi_r(x). \qquad (49)$$

The phase calculated using equation 49 is a principal value ranging from $-\pi$ to π. The phase distribution is wrapped into this range and has discontinuities at $-\pi$ and π. The unwrapped phase distribution can be automatically obtained by the Macy phase unwrapping algorithm (Macy, 1983).

To calculate the height from a point on the object to the reference plane, $z(x,y)$, either the simple geometrical relation given by equation 50 is used

$$z(x,y) = \frac{L\, p\, \Delta\varphi(x,y)}{2\pi d - p\, \Delta\varphi(x,y)}, \qquad (50)$$

or it can be determined by calibration, where the relation between a phase unit and a real length unit, such as millimeter, is defined.

Because it is difficult to accurately measure the distances d and L defined and shown in figure 26 and to evaluate the system error of the experimental set-up, calibration of the system is recommended to eliminate the system error. The calibration procedure can be performed using an object whose shape is known with the required measurement precision. The calibration and measurement procedures can be fully automated.

Experimental Set-up

Figure 27 shows a schematic of the measurement set-up used in this section of the report. A precision projector is used to project a Ronchi grating on the object surface. The projected grating is imaged using a charge-coupled device (CCD) video camera, whose optical axis can be either parallel or converging with that of the projector, without any noticeable affect on the measurement result. Data acquisition is performed using a video camera and a

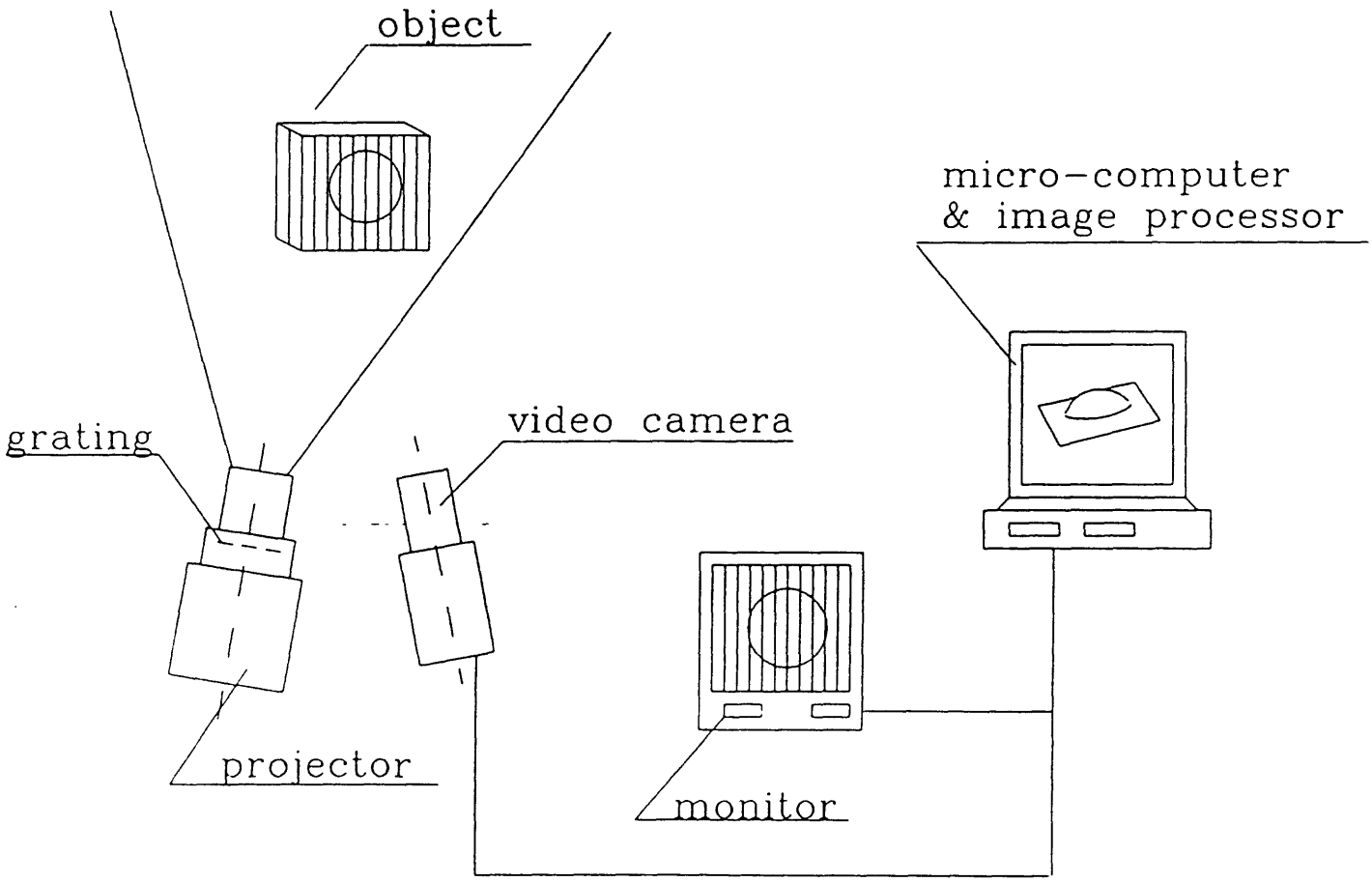

Figure 27. Schematic of the experimental set-up.

4-megabyte image memory video digitizing image processing board. The resolution of the image is 752 (horizontal) x 480 (vertical) pixels. The image board works in conjunction with a 486DX2/50 microcomputer. A color video monitor is used to show the acquired video images. A machined reference plane is located near the object being measured. The processing of a 256 x 256 pixel window with this experimental set-up takes less than 8 seconds. This includes writing the result into a file. It is estimated that with a computer accelerator board and suitable software, real-time measurement could be easily achieved.

Six different kinds of object surfaces were tested, including some simple diffuse reflecting cylindrical, spherical, triangular and sinusoidal surfaces and more complicated rock and silicon wafer surfaces. The axis of the projector is set up parallel to that of the CCD video camera. The pitch of the Ronchi grating used is 20 lines per mm.

Semi-Cylindrical Surface

The semi-cylindrical surface is a cylinder that was placed next to a flat plane. The radius of the cylinder is 32.25 ± 0.01 mm and its length is 125.00 ± 0.1 mm. It was machined to this tolerance using a lathe and checked with a dial gage. The distance between reference plane and the lens plane L, shown in figure 26, is 653.1 mm. The magnification factor on the reference plane is

10.874, and the grating fringe pitch, p, is 0.544 mm (4.418 pixels on the reference plane). Figure 28 shows the deformed grating image, and figure 29 shows the three-dimensional reconstruction of the semi-cylindrical object surface. The measured area is 60.06 mm by 44.92 mm. The statistical mean error of this measurement using 100,490 points on the object surface, compared to the actual nominal radius of the cylinder, is 0.142 percent. The statistical absolute error is 46 microns.

Semi-Spherical Surface

The semi-spherical surface is obtained by carefully machining a semi-spherical surface on a flat plane. The nominal radius of the spheroid is 53.81 mm. The object is located 697.4 mm from the lens plane. The magnification factor is 11.680, and the pitch of the grating fringe on the reference plane is 0.584 mm (4.436 pixels). Figures 30 shows the deformed grating image, and figure 31 shows the reconstruction of the semi-spherical object surface. The measured area is 62.89 mm by 52.46 mm. The results of measuring about 90,000 points on the spherical surface show that the statistical mean error related to the nominal radius of the sphere is 0.129 percent, which gives a statistical absolute error of 69 microns.

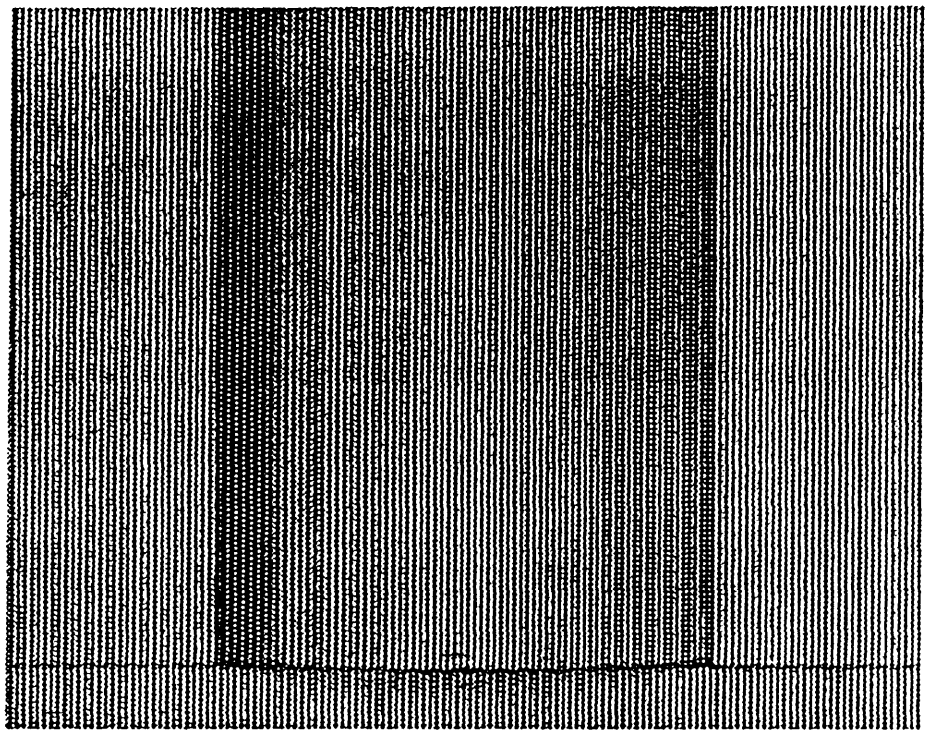

Figure 28. Deformed grating image of a semi-cylindrical surface.

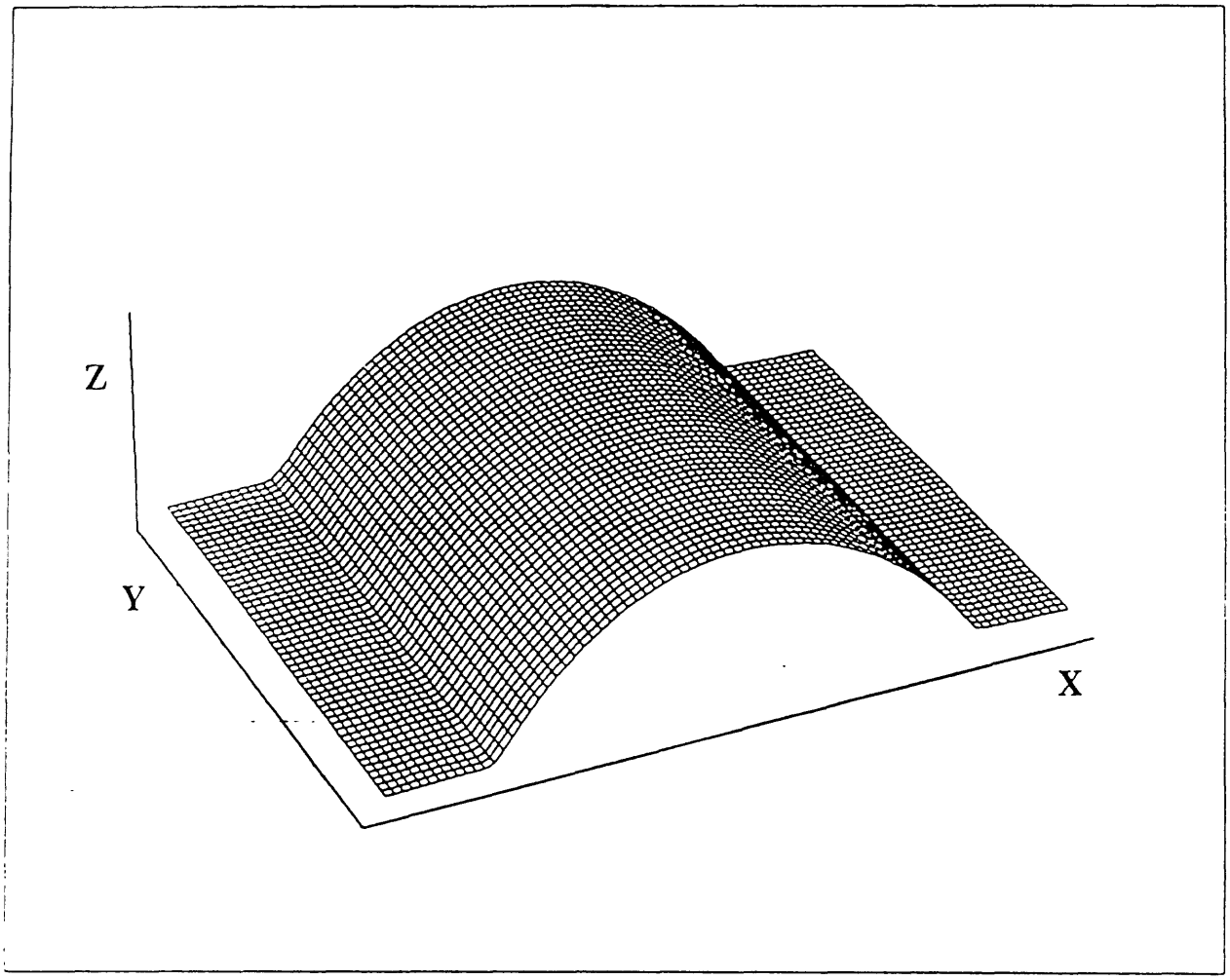

Figure 29. Three-dimensional reconstruction of a semi-cylindrical surface.

Other Surfaces

The deformed grating image and their three-dimensional reconstruction for a roof-like triangular surface, a wavy surface, a coarse rock surface, and a silicon wafer are shown in figures 32-39. If a visual comparison is made of the reconstructed rock surface to the real object, great similarity is found, even in the smallest details. The statistical mean error of the measurements is predicted to be less than 0.15 percent. The resolution in the direction of the optical axis that can be reached is from 50 to 70 microns.

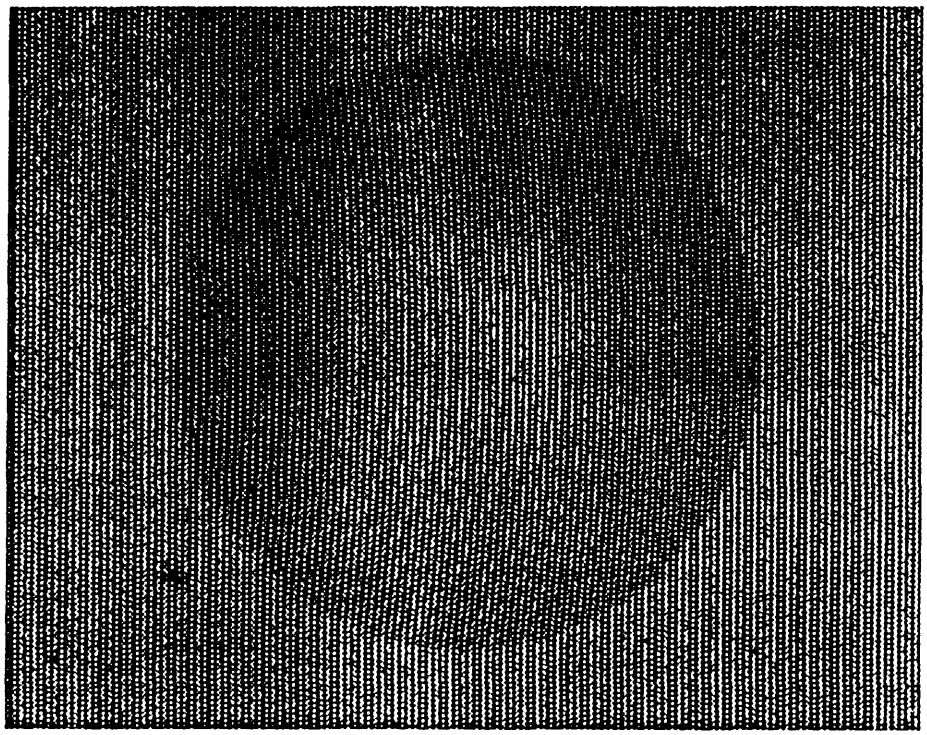

Figure 30. Deformed grating image of a semi-spherical surface.

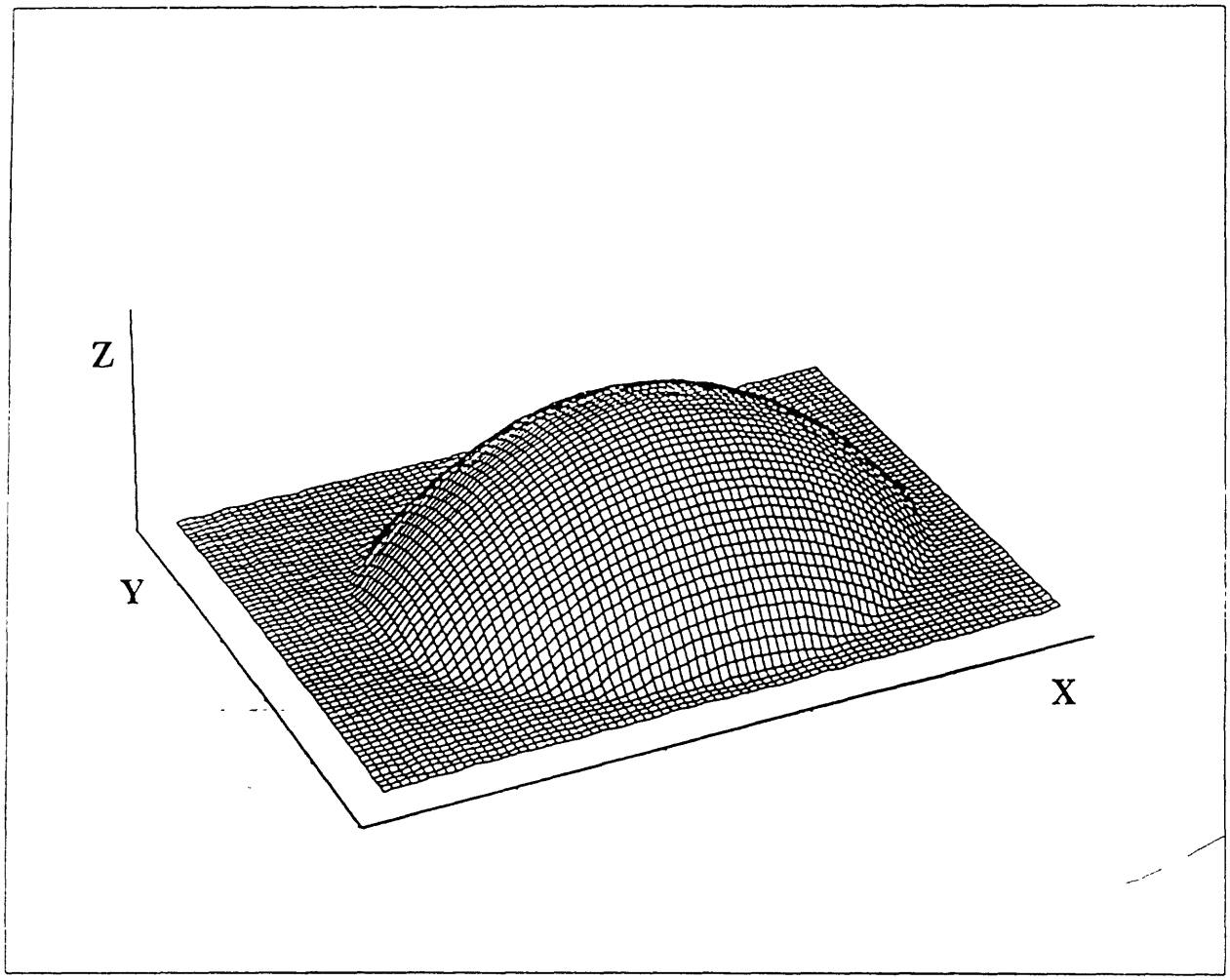

Figure 31. Three-dimensional reconstruction of a semi-spherical surface.

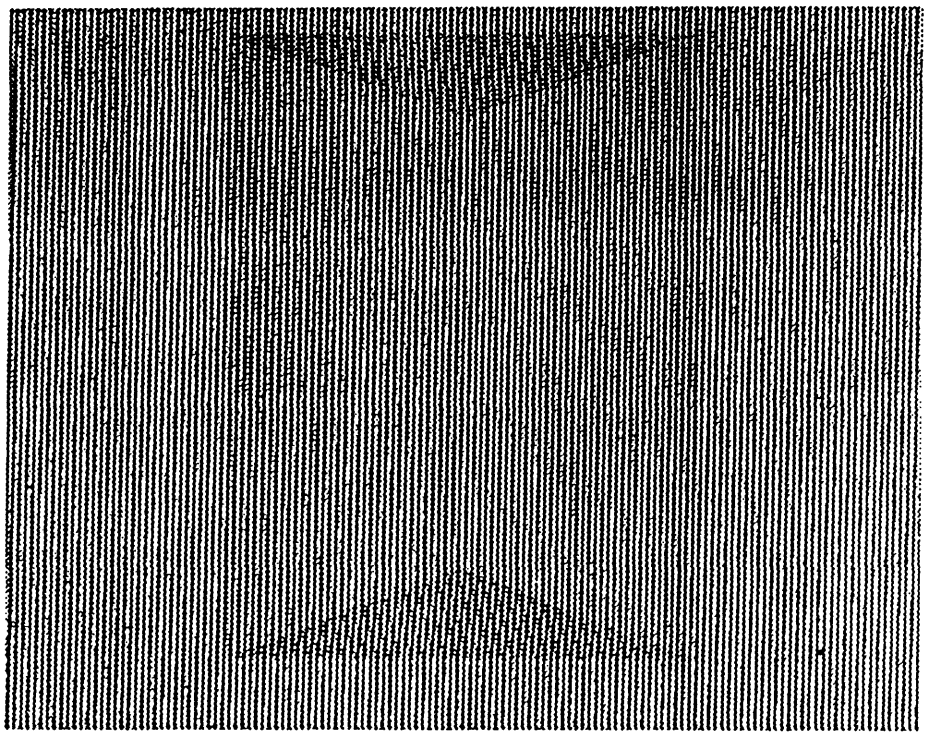

Figure 32. Deformed grating image of a triangular surface.

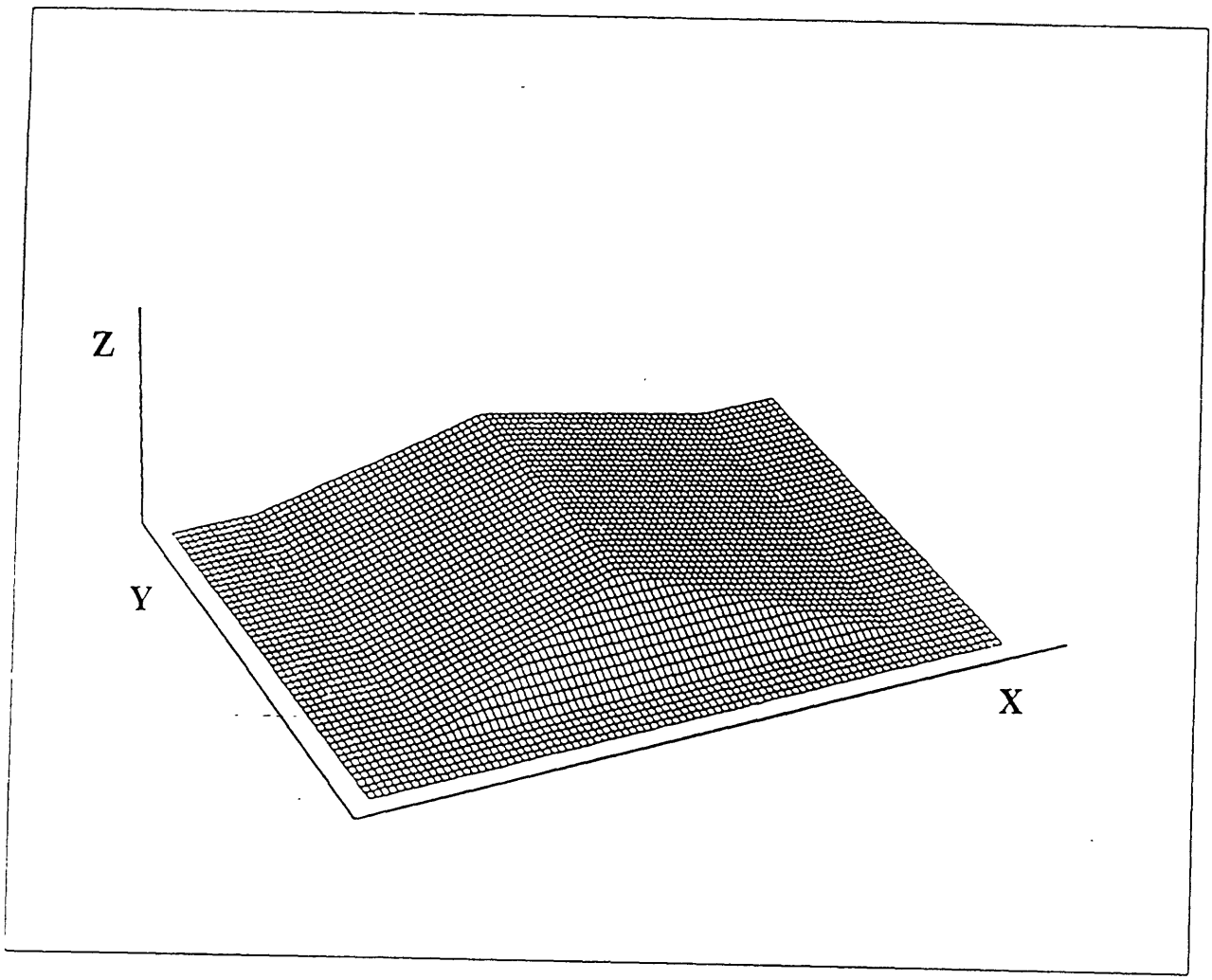

Figure 33. Three-dimensional reconstruction of a triangular surface.

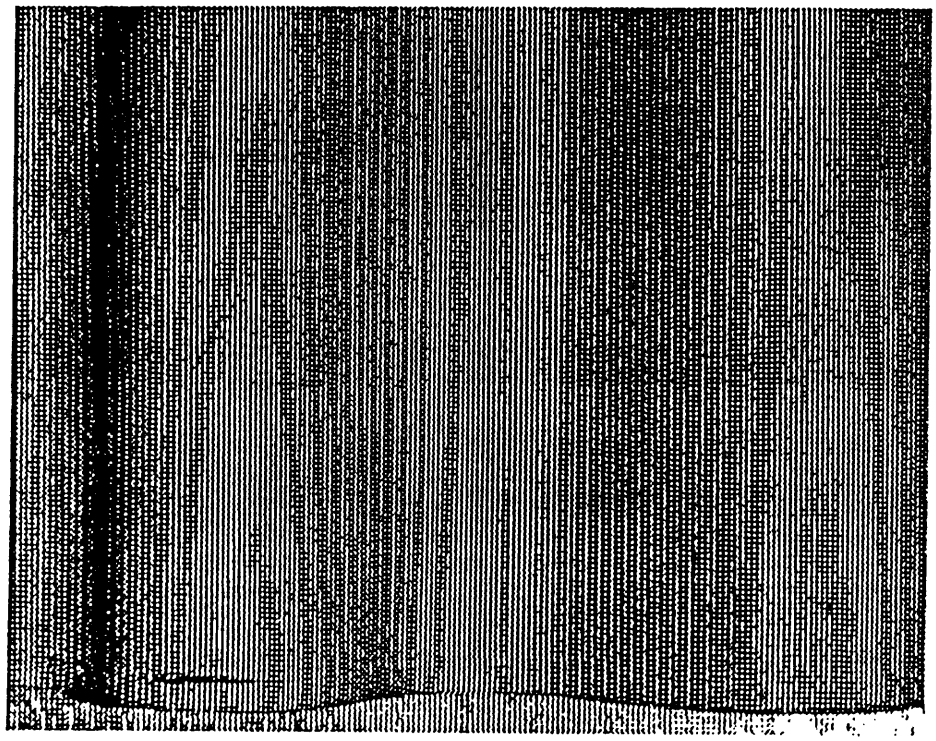

Figure 34. Deformed grating image of a wavy surface.

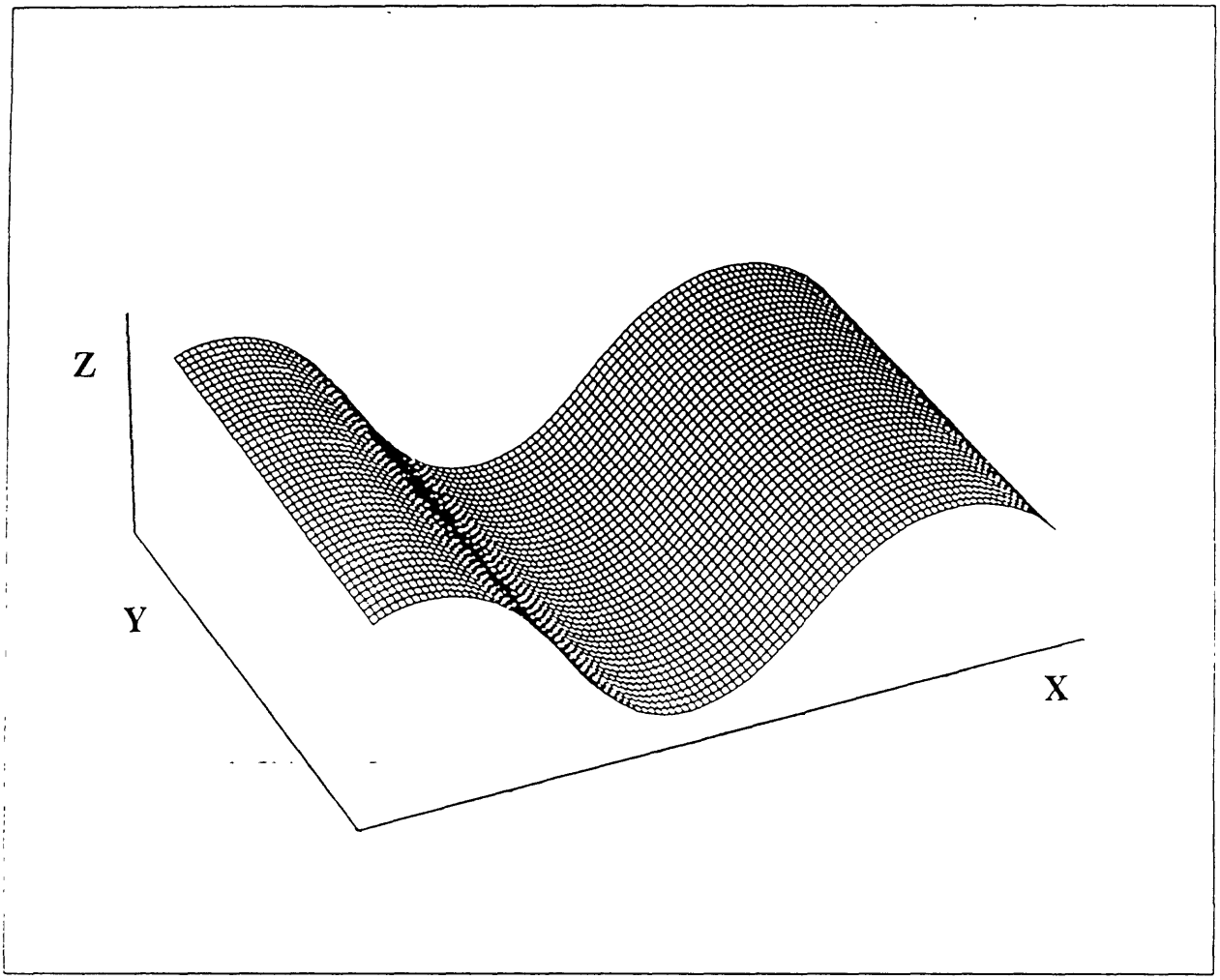

Figure 35. Three-dimensional reconstruction of a wavy surface.

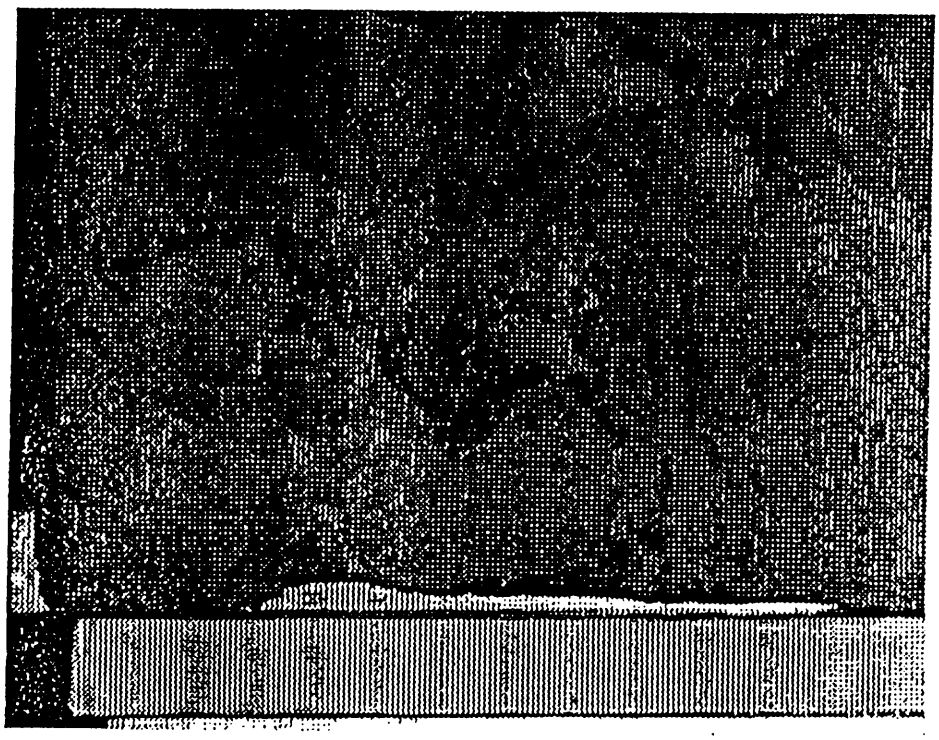

Figure 36. Deformed grating image of a rock surface.

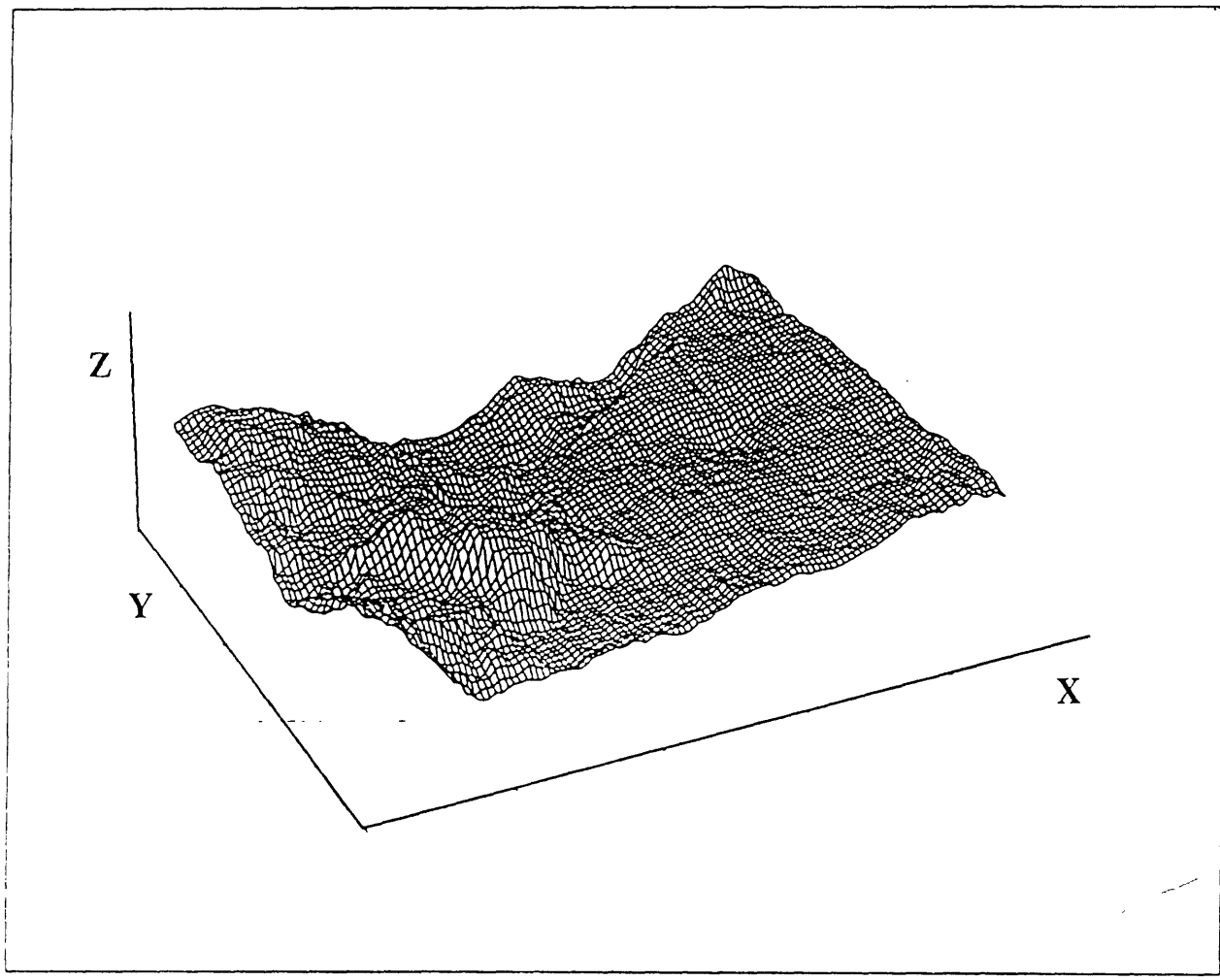

Figure 37. Three-dimensional reconstruction of a rock surface.

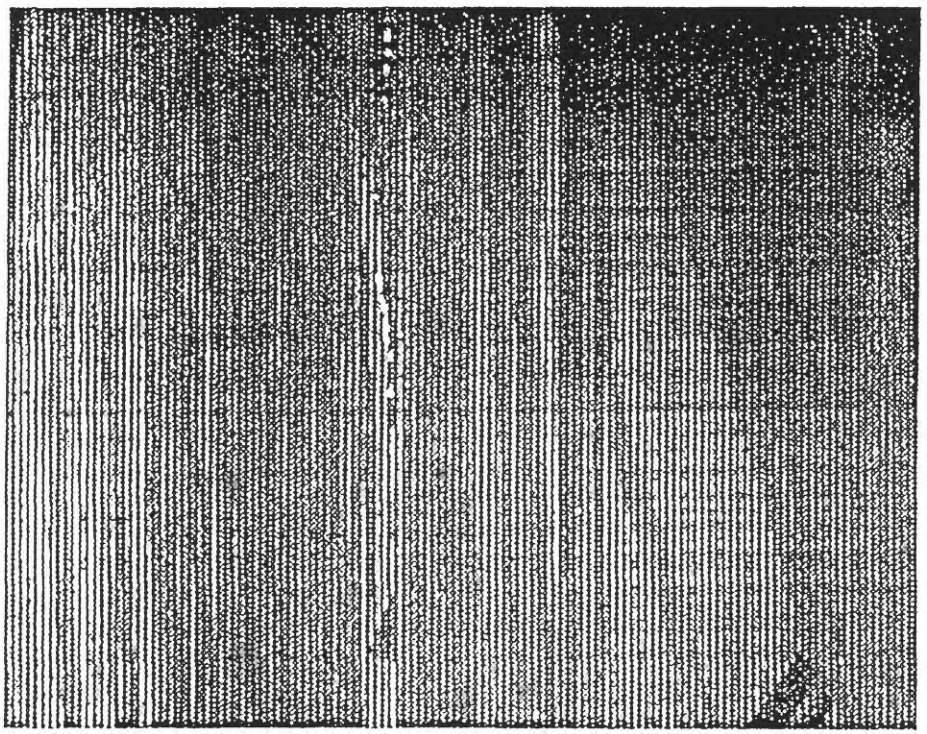

Figure 38. Deformed grating image of a silicon-wafer surface.

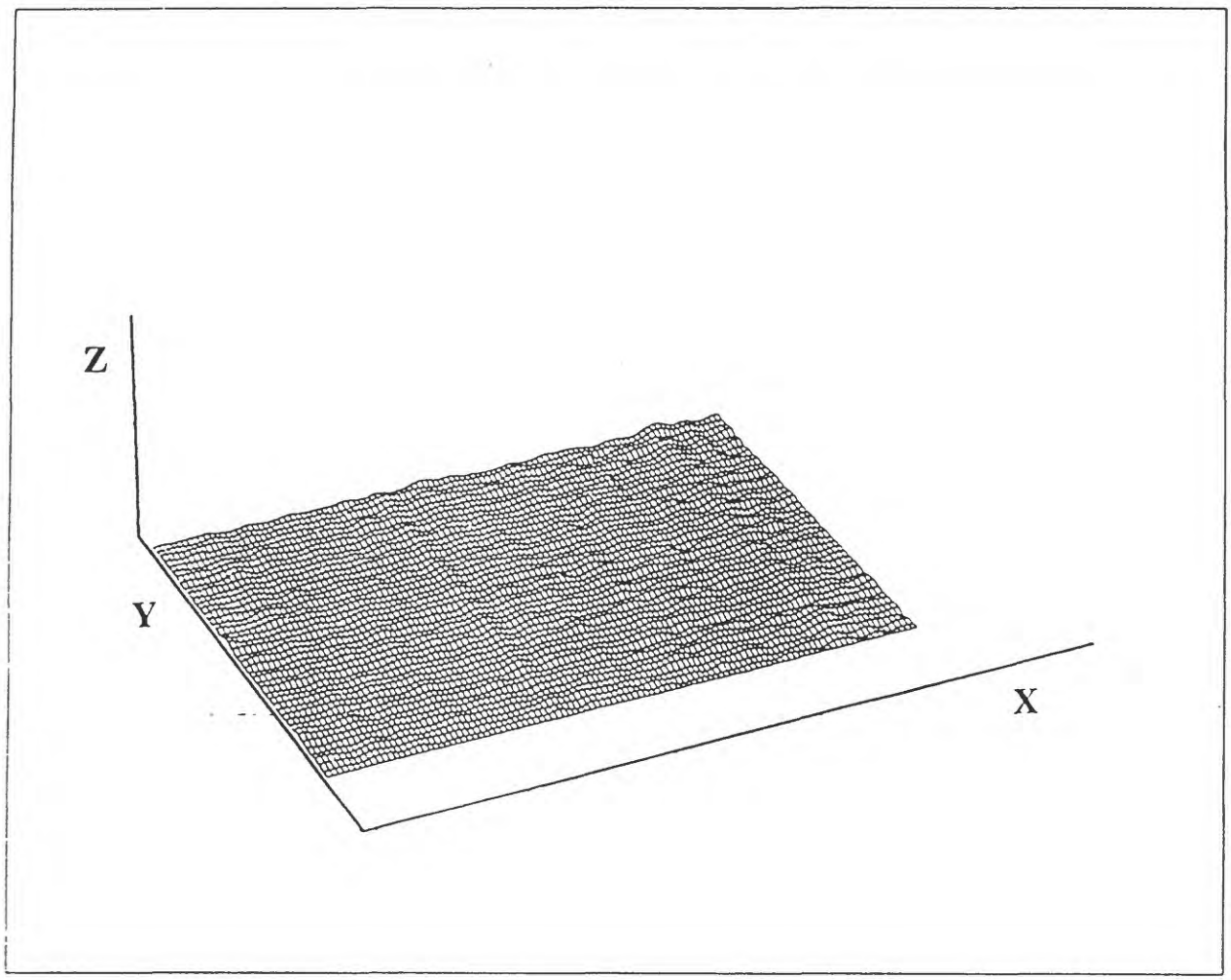

Figure 39. Three-dimensional reconstruction of a silicon-wafer surface.

SUMMARY

Three experimental techniques for assessing the topography of object surfaces are projection moire, stereo imaging, and phase-measuring profilometry. These experimental techniques were developed in the laboratory to make topographical measurements of various objects.

This study was conducted to support site-characterization for the Yucca Mountain Project. A method was developed to digitize the topography of fracture surfaces for a series of tests investigating the hydrologic characteristics of the welded and nonwelded tuffs at Yucca Mountain. These tests are for determining the relations between unsaturated-fracture flow and fracture roughness.

The first experimental technique described in this report is an automated projection moire experimental set-up that is capable of displaying and measuring the three-dimensional form of some simple objects. Calibration of the experimental set-up, determination of the fringe number, and use of phase information are important aspects of this approach. The resolution and relative error were obtained using a cylindrical surface. This experimental set-up can be used for distinguishing the concavity and convexity of a surface.

Projection moire is not an ideal optical technique for making

topographical measurements of surfaces. The principal problems of implementing moire projection in an automated mode are the following: Making an automatic distinction between a depression and an elevation from a contour map of the object requires the use of more than one image; assigning fringe orders automatically, including those separated by discontinuities; locating the center lines of broad fringes by correcting unwanted irradiance variations caused by nonuniform light reflection on the object surface; interpolating regions lying between contour lines; and evaluating the existence of false or partially dark fringes. However, despite these problems, projection moire is an experimental technique that provides a method for displaying and measuring the three-dimensional form of large objects with continuously variable resolution.

In the second section of this report, two stereo-imaging experimental set-ups for measuring the three-dimensional geometry of objects are described. A parallel optical-axis model and a converging optical-axis model are both obtainable from the same theoretical development. Digital image correlation was used to find the disparities between corresponding points in a pair of images, for each of these models, with sub-pixel accuracy. Four different object surfaces were used to illustrate the application of the developed algorithms and the stereo-imaging experimental set-ups. For some of the objects tested, a higher measuring accuracy was obtained from the converging optical-axis experimental

set-up.

The most promising approach, phase-measuring profilometry, is described in the third section of this report. Phase-measuring profilometry provides a new fast profilometer for full-field three-dimensional shape measurement. Compared to other optical methods for three-dimensional shape measurement, this technique is faster, and more accurate. The technique is based on the principle of phase measurement of a projected grating image on the object surface that conforms to the shape of the object. This deformed grating pattern carries the three-dimensional shape information of the surface to be measured. Six different object surfaces were measured with this experimental technique. The measurement error was less than 0.15 percent, and, for the objects used, the resolution was 50 microns.

REFERENCES CITED

Allen, J.B., and Meadows, D.M., 1971, Removal of unwanted patterns from moire contour maps by grid translation techniques: Applied Optics, v. 10, no. 1, p. 210-212.

Anuta, P.E., 1970, Spatial registration of multispectral and multitemporal digital imagery using fast Fourier transform techniques: Institute of Electrical and Electronics Engineers, Transactions on Geoscience Electronics, v. GE-8, no. 4, p. 353-368.

Asundi, Anand, 1991, Projection moire using PSALM: in Chiang, F.P., ed., Proceedings, Second International Conference on Photomechanics and Speckle Metrology: San Diego, Calif., International Society for Optical Engineering, 22-26 July, v. 1554B, p. 257-265.

Barnard, S.T., and Thompson, W.B., 1980, Disparity analysis of images: Institute of Electrical and Electronics Engineers, Transactions on Pattern Analysis and Machine Intelligence, v. PAMI-2, no. 4, p. 333-340.

Barnea, D.I. and Silverman, H.F., 1972, A class of algorithms for fast digital image registration: Institute of Electrical and Electronics Engineers, Transactions on Computers, v. C-21, no. 2, p. 179-186.

Cardenas-Garcia, J.F., Zheng, S., and Shen, F.Z., 1991, Projection moire as a tool for the automated determination of surface topography: in Chiang, F.P., ed., Proceedings, Second International Conference on Photomechanics and Speckle Metrology: San Diego, Calif., International Society for Optical Engineering, 22-26 July, v. 1554B, p. 210-224.

Chiang, Chun, 1975, Moire topography: Applied Optics, v. 14, no., 1, p. 177-179.

Cline, H.E., Holik, A.S., and Lorensen, W.E., 1982, Computer-aided

surface reconstruction of interference contours: Applied Optics, v. 21, no. 24, p. 4481-4488.

Cline, H.E., Lorensen, W.E., and Holik, A.S., 1984, Automatic moire contouring: Applied Optics, v. 23, no. 10, p. 1454-1459.

Dally, J.W., and Riley, W.F., 1991, Experimental Stress Analysis, (3d ed.): New York, McGraw-Hill, Inc., p. 389-390.

Der Hovanesian, J., and Hung, Y. Y., 1971, Moire contour-sum contour-difference, and vibration analysis of arbitrary objects: Applied Optics, v. 10, no. 12, p. 2734-2738.

Dirckx, J.J.J., Decraemer, W.F., and Dielis, G., 1988, Phase shift method based on object translation for full field automatic 3-D surface reconstruction from moire topograms: Applied Optics, v. 27, no. 6, p. 1164-1169.

Doty, J.L., 1983, Projection moire for remote contour analysis: Journal of Optical Society of America, v. 73, no. 3, p. 366-372.

Durelli, A.J., and Parks, V.J., 1970, Moire analysis of strain: Englewood Cliffs, Prentice-Hall, Inc., N.J., p. 1.

Frobin, W., and Hierholzer, E., 1982, Calibration and model reconstruction in analytical close-range stereophotogrammetry,

part 1, mathematical fundamentals: Photogrammetric Engineering And Remote Sensing, v. 48, no. 1, p. 67-72.

Funnell, W.R.J., 1981, Image processing applied to the interactive analysis of interferometric fringes: Applied Optics, v. 20, no. 18, p. 3245-3250.

Gasvik, K.J., 1983, Moire technique by means of digital image processing: Applied Optics, v. 22, no. 23, p. 3543-3548.

Gasvik, K.J., and Fourney, M.E., 1986, Projection moire using digital video processing--A technique for improving the accuracy and sensitivity: Transactions of the American Society of Mechanical Engineers, v. 53, no. 3, p. 652-656.

Gasvik, K.J., 1987, Optical metrology: New York, John Wiley and Sons, p. 117-144.

Grimson, W.E.L., 1981, A computer implementation of a theory of human stereo vision: Philosophe Transactions of the Royal Society of London, v. 292, no. B1058, p. 217-253.

Grimson, W.E.L., 1984, Binocular shading and visual surface reconstruction: Computer Vision, Graphics, and Image Processing, v.28, no. 1, p. 19-43.

Grimson, W.E.L., 1985, Computational experiments with a feature

based stereo algorithm: Institute of Electrical and Electronics Engineers, Transactions on Pattern Analysis and Machine Intelligence, v. PAMI-7, no.1, 17-34.

Halioua, M., Krishnamurthy, R.S., Liu, H., and Chiang, F.P., 1983, Projection moire with moving gratings for automated 3-D topography: Applied Optics, v. 22, no. 6, p. 850-855.

Harding, K.G., and Harris, J. S., 1983, Projection moire interferometer for vibration analysis: Applied Optics, v. 22, no. 6, p. 856-861.

Heiniger, F., and Tschudi, T., 1979, Moire depth contouring: Applied Optics, v. 18, no. 10, p. 1577-1581.

Ichioka, Y., and Inuiya, M., 1972, Direct phase detecting system: Applied Optics, v. 11, p. 1507-1514.

Idesawa, Mansanori, Yatagai, Toyohiko, and Soma, T., 1977, Scanning moire method and automatic measurement of 3-D shapes: Applied, Optics, v. 16, no. 8, p. 2152-2162.

Jaerisch, W., and Makosch, G., 1973, Optical contour mapping of surfaces: Applied Optics, v. 12, no. 7, p. 1552-1557.

Jain, Ramesh, Bartlett, Sandra, L., and O'Brien, Nancy, 1987,

Motion stereo vision ego-motion complex logarithmic mapping: Institute of Electrical and Electronics Engineers, Transactions on Pattern Analysis and Machine Intelligence, v. PAMI-9, no. 3, p. 356-369.

Jin, G.C., and Tang, S., 1989, Automated contouring of diffuse surfaces: Optical Engineering, v. 28, no. 11, p. 1211-1215.

Kafri, Oded, and Glatt, Ilana, 1990, The physics of moire metrology: New York, John Wiley & Sons, p. 61-74.

Karara, H.M. ed., 1989, Non-Topographic Photogrammetry (2d ed.): Falls Church, Va., American Society for Photogrammetry and Remote Sensing, p. 231-263.

Kashef, B.K., 1983, A survey of new techniques for image registration and mapping: Proceedings, Society of Photo-Optical and Instrumentation Engineers, v. 432, p. 222-239.

Kujawinska, Malgorzata, and Robinson, D.W., 1988, Multichannel phase-stepped holographic interferometry: Applied Optics, v. 27, no. 2, 312-20.

Kujawinska, Malgorzata, and Wojciak, J., 1991, Spatial phase-shifting techniques of fringe pattern analysis in photomechanics: in Chiang, F.P., ed., Proceedings, Second

International Conference on Photomechanics and Speckle Metrology: San Diego, Calif., International Society for Optical Engineering, 22-26 July, v. 1554B, p. 503-513.

Lee, Dah-Jye, 1990, Depth information from image sequences using two-dimensional cepstrum: Lubbock, Texas Tech University, Ph.D. dissertation, 102 p.

Lillestrand, R.L., 1972, Techniques for change detection: Institute of Electrical and Electronics Engineers, Transactions on Computers, v. C-21, p. 654-659.

Livnat, A., Kafri, Oded, and Erez, G. 1980, Hills and valleys analysis in optical mapping and its application to moire contouring: Applied Optics, v. 19. no. 19, p. 3396-3400.

Macy, W.W., Jr., 1983, Two-dimensional fringe-pattern analysis: Applied Optics, v. 22, no. 23, p. 3898-3901.

Marr, D., and Poggio, T., 1979, A computational theory of human stereo vision: Proceedings of the Royal Society of London, v. B204, p. 301-328.

Meadows, D.M., Johnson, W.O., and Allen, J.B., 1970, Generation of surface contours by moire patterns: Applied Optics, v. 9, no. 4, p. 942-947.

Meyer-Arendt, J.R., Smith, B.G., and Weekly, R.J., 1987, Moire topograms--A simple method for their evaluation: Applied Optics, v. 26, no. 7, p. 1166-1167.

Moore, D.T., and Truax, B.E., 1979, Phase-locked moire fringe analysis for automated contouring of diffuse surfaces: Applied Optics, v. 18, no. 1, p. 91-96.

Perrin, J.C., and Thomas, A., 1979, Electronic processing of moire fringes--Application to moire topography and comparison with photogrammetry: Applied Optics, v. 18, no. 4, p. 563-574.

Rayleigh, Lord, 1874, On the manufacture and theory of diffraction-gratings: Philosophical Magazine and Journal of Science, 4th series, v. 47, no. 310, p. 193-205.

Robinson, D.W., 1983, Automatic fringe analysis with a computer image-processing system: Applied Optics, v. 22, no. 14, p. 2169-2173.

Schemm, J.B., and Vest, C. M., 1983, Fringe pattern recognition and interpolation using nonlinear regression analysis: Applied Optics, v. 22, no. 18, p. 2850-2853.

Takasaki, Hiroshi, 1970, Moire topography: Applied Optics, v. 9, no. 6, p. 1467-1472.

Takasaki, Hiroshi, 1973, Moire topography: Applied Optics, v. 12, no. 4, p. 845-850.

Takeda, Mitsuo, Ina, Hideki, and Kobayashi, Seiji, 1982, Fourier-transform method of fringe-pattern analysis for computer-based topography and interferometry: Journal of the Optical Society of America, v. 72, no. 1, p. 156-160.

Takeda, Mitsuo, and Mutoh, K., 1983, Fourier transform profilometry for the automatic measurement of 3D object shapes: Applied Optics, v. 22, no. 24, p. 3977-3982.

Tang, S., and Hung, Y.Y., 1990, Fast profilometer for the automatic measurement of 3D object shapes: Applied Optics, v. 29, no. 20, p. 3012-3018.

Tsuruta, T., Itoh, Y., and Anzai, S., 1970, Moire topography for the measurement of film flatness: Applied Optics, v. 9, no. 12, p. 2802-2803.

U.S. Department of Energy, 1988, Site characterization plan, Yucca Mountain Site, Nevada Research and Development Area, Nevada, U.S. Department of Energy, Washington, D.C.

Womack, K.H., 1984, Interferometric phase measurement using spatial synchronous detection: Optical Engineering, v. 23,

no. 4, p. 391-400.

Wu, C.K., Wang, D. Q., and Bajcsy, R. K., 1983, Acquiring 3-D spatial data of a real object: Computer Vision, Graphics, and Image Processing, v. 28, no. 1, p. 126-133.

Yatagai, Toyohiko, Nakadate, Suezou, Idesawa, Masanori, and Saito, Hiroyoshi, 1982, Automatic fringe analysis using digital image processing techniques: Optical Engineering, v. 21, no. 3, p. 432-435.

Yokozeki, S., and Suzuki, T., 1970, Interpretation of the moire method for obtaining contours of equal slope from an interferogram: Applied Optics, v. 9, no. 12, p. 2804-2805.

APPENDIX - Newport Corporation Precision Moire Gratings

(Manufacturer Specifications)

Model:	MGP-20
Pitch:	20 line pairs per mm. A line pair consists of one dark and one bright line
Format:	35 mm
Fabrication:	Double coated chrome pattern on 1.6-mm-thick optical glass
Flatness:	0.0002 in. (0.00508 mm) for 2 in. by 2 in. (50.8 mm by 50.8 mm)
Optical density:	D > 3.0
Local defects:	Voids/blockage < 0.00